UNIVERSITY OF OKLAHOMA

GRADUATE COLLEGE

# GEOMECHANICS OF UNCONVENTIONAL RESERVOIRS: HYDRAULIC FRACTURING AND NANOINDENTATION

A THESIS

SUBMITTED TO THE GRADUATE FACULTY

in partial fulfillment of the requirements for the

Degree of

MASTER OF SCIENCE

By

JUAN CAMILO ACOSTA MONTENEGRO
Norman, Oklahoma
2021

# GEOMECHANICS OF UNCONVENTIONAL RESERVOIRS: HYDRAULIC FRACTURING AND NANOINDENTATION

A THESIS APPROVED FOR THE
MEWBOURNE SCHOOL OF PETROLEUM AND GEOLOGICAL ENGINEERING

BY THE COMMITTEE CONSISTING OF

Dr. Carl H. Sondergeld, Chair

Dr. Chandra S. Rai, Co-Chair

Dr. Deepak Devegowda

*This thesis is dedicated to my parents, advisor, and friends for their unconditional and endless support and encouragement*

## ACKNOWLEDGEMENTS

This journey has been one of the most amazing experiences in my life. I would not have seen myself in Oklahoma five years ago, and now I would not change the past three and a half years for anything else.

Firstly, to my advisors. To Dr. Carl Sondergeld, I have nothing but gratitude. From the first semester, when I was late to a meeting, he started helping me enter a path full of dedication, respect, and proactivity. He guided me and challenged me to be better. To Dr. Chandra Rai, I want to thank him for his support and supervision; he encouraged me to work harder and improve my skills. They both believed in me and trusted me with conviction that I would succeed, giving me a unique opportunity that I will never forget. They are my role models and people I am incredibly thankful for; this would not have been possible without them.

I want to also thank people who advised and mentored me. Thank you to Dr. Deepak Devegowda and Dr. Ali Tinni for their continuous support and time in research and classes. To Dr. Son Dang, who was unconditional from the first day, guided me to develop new ideas and challenge myself in new projects. To Dr. Mark Curtis, I want to thank him for allowing me to work with him, for his guidance and support. To Dr. Felipe Pérez, the first person to receive me at the University and always supported me in and out of work.

I want to acknowledge Gary Stowe, Micaela Langevin, and Jeremy Jernigen for their support. Without their help and care, this would not have been possible. I thank the Unconventional Shale Gas Consortium members for their advice, suggestions, and research support.

Finally, I thank the people behind me for pushing me to continue this journey. My mom and dad for always carrying me forward. Their love and faith have taken me to places far beyond what I imagined. To my friends who made Oklahoma home and these years unforgettable: Eleonora, Michael, Vanessa, David, Alejandra, Esteban, and Jhouly. And to my $IC^3$ team: Wyatt, Sanchay, Sidi, Judah, Adesoji, Jing, Heyleem, and Amanda, for being always there and making work time better.

## ABSTRACT

Geomechanics is the study of the mechanical response of geologic formations subjected to injection, production, and storage of fluids in the subsurface. It plays a role in understanding formation integrity and the response to oil and gas depletion during well completion. Recent studies also relate geomechanics to energy transition methods, such as carbon capture storage and geothermal energy. In this thesis, we combine nanoindentation with hydraulic fracturing testing and acoustic emissions monitoring to approach one question. *Can we combine nanoindentation and hydraulic fracturing laboratory testing to understand and improve solutions for common problematics in completions design, such as the reduction in hydraulic fracturing breakdown pressure, total stimulated reservoir volume, time-dependent deformation, and rock and fluid interactions?*

Using cyclic injection, a greater number of cycles reduced the monotonic breakdown pressure and the average seismic moment of induced acoustic events. The number of acoustic events increased with more cycles, reflected in a greater estimated stimulated reservoir volume (SRV). The 4-cycle test was the most efficient test, with the greatest SRV generated based on the work inputted. Additionally, nanoindentation showed linear gel as a damaging agent for carbonate rich samples, ash beds to record a significantly lower Young's modulus than the formation matrix, and modeled primary and secondary creep in shales, showing a dependency on clay and total organic content.

# TABLE OF CONTENTS

# LIST OF FIGURES

# LIST OF TABLES

# 1. INTRODUCTION

Oil and gas production is one of the main drivers worldwide. Once hydrocarbons are refined and processed, petroleum becomes the energy source for multiple industries. ***Fig. 1.1*** displays the use of oil in different sectors, including transportation, industrial and residential, and electric power. Only within those three sectors, a total of 18.1 million of barrels per day are utilized, coming mainly from sources of gasoline, fuel, and hydrocarbon gas. ***Fig. 1.2*** shows the U.S. natural gas consumption by sector; there in an incremental trend over the latest years. As consumption continued to increase, engineers needed to find ways and techniques to satisfy consumption by increasing the oil and gas production. One of the main techniques developed was hydraulic fracturing. It consisted of the injection of fluids -primarily composed of water- to the subsurface to induce fractures in low permeability rocks and recover stored hydrocarbons. Hydraulically fractured wells have increased over the last years (***Fig. 1.3b***). The steps followed during fracturing are explained:

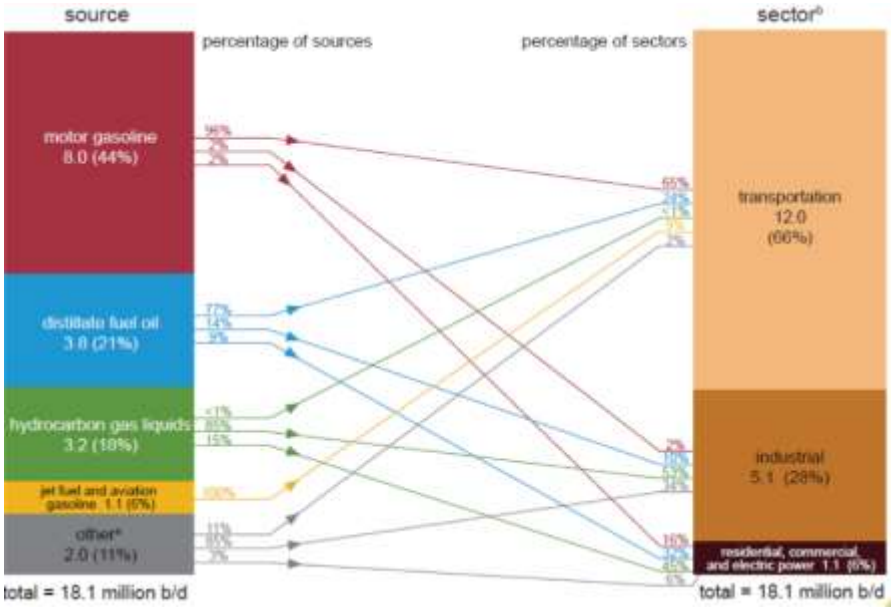


*Figure 1-1. Petroleum products consumption in the United States for 2020 classified by the source and sector. This is a large production that continues to increase every year (U.S. Energy Information Administration, 2021)*

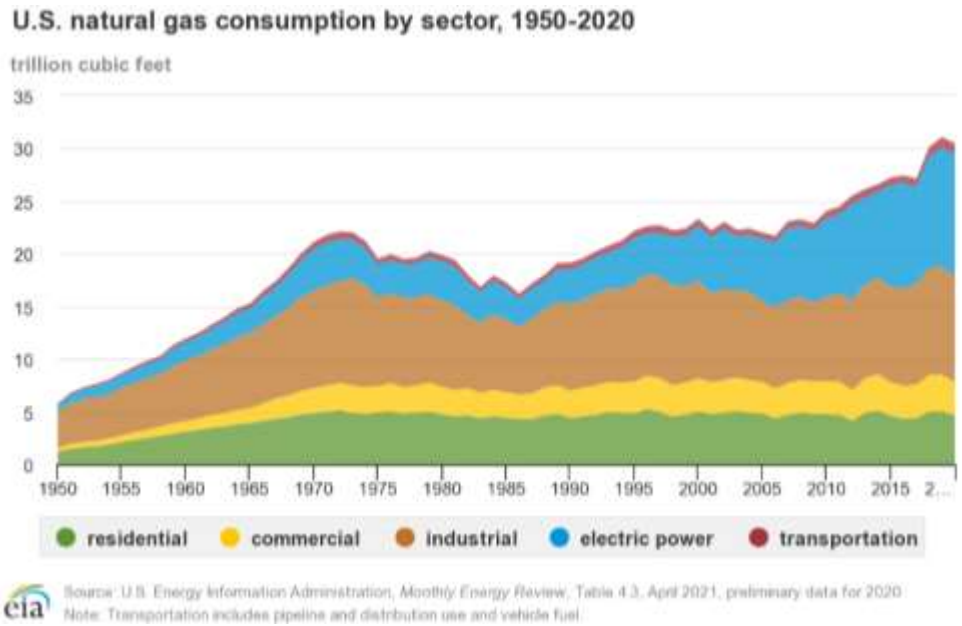


*Figure 1-2. Natural gas consumption in trillion cubic feet based on the sector for the past 70 years. Note the increasing trend over the last 10 years (U.S. Energy Information Administration, 2021).*

- Hydraulic fracturing starts by injecting fluids into the formation until it exceeds the fracture pressure. Multiple methods (Cyclic, Variable Rate, Zipper) have been used to ***reduce the breakdown pressure***, and they have been proven to work according to the formation properties.

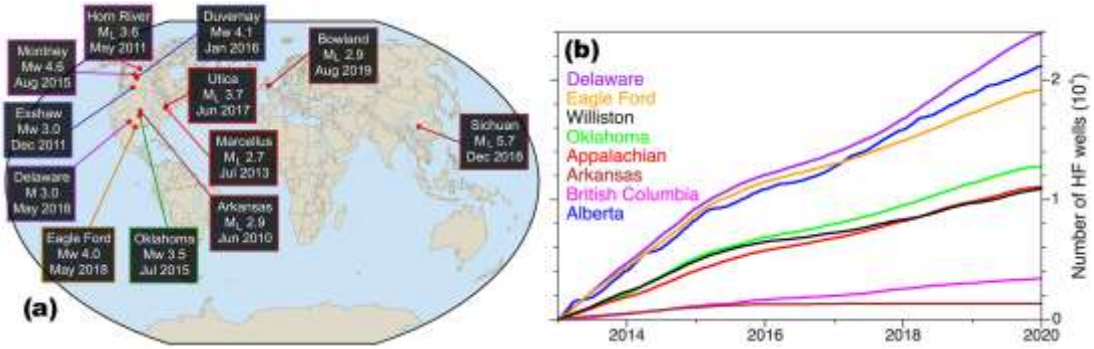


*Figure 1-3. a) Magnitude of the largest earthquake induced during hydraulic fracturing operations over the past 10 years. This shows how important it is to reduce magnitude of seismicity, as some of those earthquakes have a magnitude greater than 4.0 B) Number of wells hydraulically fracture in the last 7 years for different formations. Note that there is an increasing trend, suggesting that advances in the technique could potentially lead to even a greater number of HF wells.*

- Fractures are induced through the formation ***extending through different layers*** and interfaces. Even though some people believe that fractures are planar, multiple studies have

shown fractures more complex than planar shapes. Elastic parameters of the layers are essential once the fracture tip energy is low (i.e., far away from the wellbore).

- During fracture propagation, small earthquakes -known as ***microseismic***- are induced. Location of these events is important as usually the greater in number, the greater the productivy. Mapping those microseismics allow the recreation of the fracture network, understanding what zones are part of the stimulated reservoir.
- Proppant is placed inside the fracture, and fluids are flushed back to the surface. However, most water is never recovered and remains in contact with the formation, leading to ***rock and fluids interaction***. Acids and fracturing fluids are common fluids that react with the formation. Depending on the pH and formation petrophysics, they can damage the fracture surface and reduce elastic properties, such as Young's modulus.
- Recall that proppant is placed to hold the fractures open. After long periods, ***creep*** is observed. The longer the proppant is holding the fracture at high stresses, the greater the deformation, leading to failure and fracture closure.

**Research objective:**

Hydraulic fracturing faces different issues. Understanding what leads to those issues is the best method in finding a solution. In this study we will combine nanoindentation with hydraulic fracturing testing and acoustic emissions monitoring to understand topics such as fracture propagation in layering, increase in seismic intensity, reduction of breakdown pressure, and time-dependent deformation in soft layers. This thesis will approach two questions:

- Can we use hydraulic fracturing laboratory testing to aim to reduce breakdown pressure and seismicity, determining the effectiveness through acoustic emissions?
- Can nanoindentation be used as a technique to understand better common problematics in hydraulic fracturings, such as the contrast in elastic properties from different layers, time-dependent deformation, and rock and fluid interactions?

**Synopsis:**

This study is divided into 6 chapters. The first and second chapters include the introduction and literature review. Then, chapter 3 will touch on studies using nano-indentation, divided into rock and fluid interactions, creep parameters, and fracture propagation. Chapter 4 will consist of an analysis of hydraulic fracturing, discussing the equipment and methodology, and two studies that determine the most efficient protocol for reducing seismic magnitudes and increasing fracture network. Chapter 5 will describe some of the field applications and suggestions for future research. The last chapter will give the general conclusions.

# 2. LITERATURE REVIEW

## 2.1 Geomechanics

Geomechanics is the study of the mechanical response of geologic formations subjected to injection, production, and storage of fluids in the subsurface. Historically, it is a subject that has been extensively studied in the petroleum industry. It plays a role in understanding formation integrity and the response to oil and gas depletion during well completion. Recent studies also relate geomechanics to energy transition methods, such as carbon capture storage and geothermal energy (Rutqvist et al., 2019). Knowledge on formation stresses at various depths and properties such as the uniaxial compressive strength, Young's modulus, and Poisson's ratio can improve oil extraction mechanisms such as hydraulic fracturing. Geomechanics knowledge is required at every stage in hydraulic fracturing to understand the mechanical properties and in-situ stresses of adjacent layers during well placement for better-stimulated reservoir volumes and fracture networks. In pre-pad and pad stages, fluid interaction with the formation matrix is critical for extended fractures and greater stimulated reservoir volumes. Information on creep and Young's modulus is necessary to avoid proppant embedment and to maintain fractures apertures.

## 2.2 Hydraulic Fracturing Protocols

Hydraulic fracturing is a technique that involves injecting fluids at different flow rates into the wellbore to open fractures in the subsurface and create paths for hydrocarbons to escape. This technique is usually best described in three main stages. First, acidizing the area around the perforation holes for cleaning and clearing paths; second, injecting low and high viscosity water-based fluids until the formation breakdown pressure is reached, where fractures initiate and propagate; and last, pumping proppant (sand) to hold the induced fractures open while the injected fluid is flushed. This technique caused a breakthrough in oil and gas exploitation due to its ability in hydrocarbon recovery for unconventional reservoirs. Its advantages have expanded in other fields, including geothermal energy and carbon sequestration (Adams et al., 2013; Qian et al., 2019).

Hydraulic fracturing was patented in 1957 by J. Clark. He described it as a method to increase the well productivity by injection viscous fluids containing a granular material into a well. Since then, the monotonic injecting has been the most popular in field tests. Laboratory and field studies have been combined to understand and analyze this test. However, much remains undefined.

Laboratory studies are usually performed at small scales, and relating them to the field was, at some point, very difficult. Zang and Stephansson (2010) built a relation between laboratory and field tests by comparing fracture fault length and process zone (***Fig. 2.1***). Even though the scales differ by up to five orders of magnitude, a strong correlation permits laboratory tests to be upscaled. The correlation is 1:50, implying that a process zone will be about 2% of the fault length.

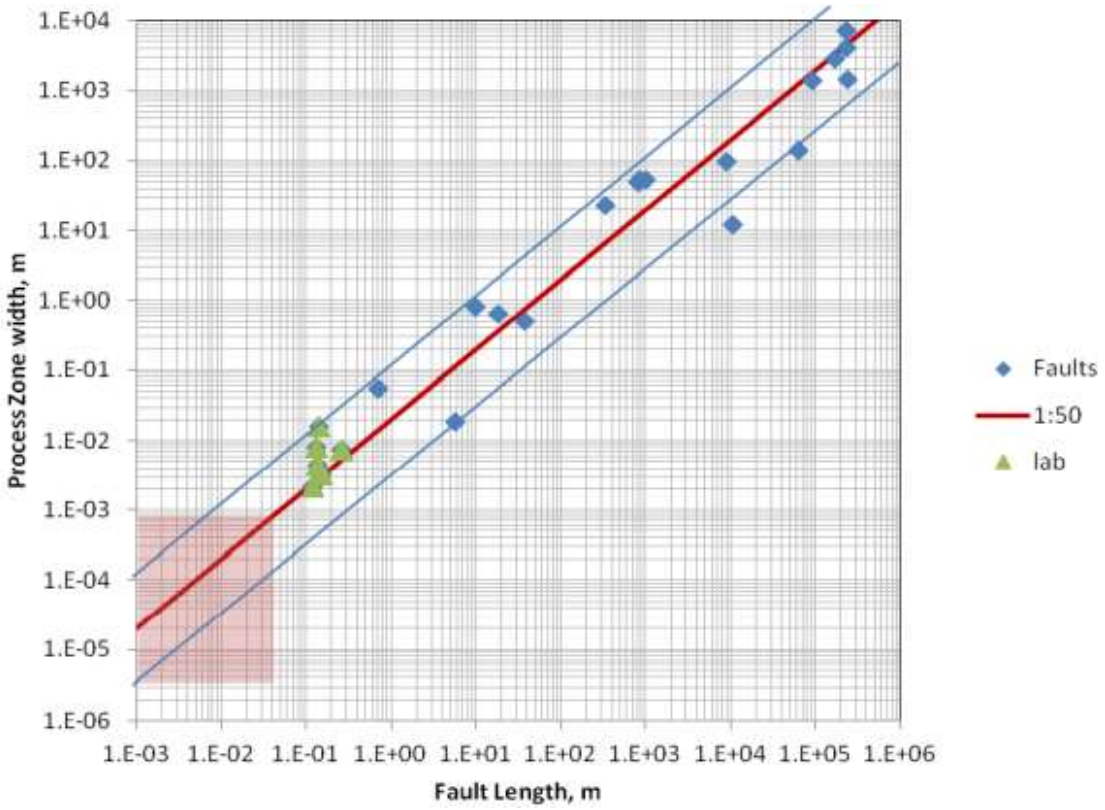


*Figure 2-1. Hydraulic fracturing upscaling from laboratory to field fractures. There is a 1:50 ratio between the process zone and the fault length. Note that laboratory experiments do not exceed a fault length of 30 cm, while field data shows faults to reach lengths up to 200 km (Zang and Stephansson, 2010).*

With the shale revolution, unconventional reservoirs became a target for exploration. It is well known that unconventional reservoirs are more complex than conventional reservoirs, and although monotonic injection was used initially as the primary method for fracturing, adjustments have been carried out. For example, different injection methods were tried to increase the stimulated reservoir volume, process zone and to reduce the breakdown pressure. Cyclic injection, variable rate injection, zipper fracking, highway fracking, and other tests have been implemented (Surgchev et al., 2008; Patel et al., 2016; Zhuang et al., 2017; Iriarte et al., 2017; Patel et al., 2017; Sukumar et al., 2019).

The cyclic injection test was first patented by Hulse (1959), where successive shock pressure waves were superimposed, which resulted in more fluid and proppant being injected into the fractures, increasing the total productivity.

Subsequent studies improved the understanding of cyclic injection. Using 1-in core samples, Erarslan and Williams (2012) studied the effect of cyclic loading on Brisbane tuff using a Brazilian test and found that cyclic injection reduced the indirect tensile strength by 35%, agreeing with observations by Mighani (2014). In addition, Scanning Electron Microscopy (SEM) imaging showed grain breakage during cyclic loading. Zhuang et al. (2016) performed a laboratory test of Pocheon granite in South Korea, seeing a reduction in breakdown pressure with cyclic injection. The reduction of breakdown pressure with cycling has been observed on different rock types, such as Tennessee Sandstone (Patel et al., 2017) and isotropic materials such as cement (Falser et al., 2016). Zhuang also noted that breakdown pressure decreased as a function of cycle numbers, and fractures were planar under monotonic injection but branched more under cyclic injection. Modifications to this test caused higher reductions in formation breakdown pressure. Al-Nakhli et al. (2019) held the pressure at each cycle peak before letting it drop to a baseline, getting a 23% reduction in breakdown pressure. Higher fracture width was obtained from cyclic hydraulic fracturing, agreeing with the increase in secondary fractures observed by Patel et al. (2017). Hofmann et al. (2018) compared cyclic injection with constant injection for both laboratory and field scales, showing agreement in lower magnitudes of seismic events under cyclic injection and more fractures produced for cyclic injection.

A secondary alternative for monotonic injection has been intended for both laboratory and field experiments. Instead of changing the pressure, the flow rate was the controlled variable. The variable rate injection test or water hammer uses sudden changes in flowrate to act as pressure

pulses and damage the rock. Ciezobka et al. (2016) saw a rise in microseismic events during these pulses, which led to an increase in production as those pulses opened closed perforations. Iriarte and Merritt (2017) showed this test to depend on the completion type and fluid system. Using pressure pulses, a well-connected fracture network near the wellbore was created with increase in production.

The Integrated Core Characterization Center has performed laboratory tests on hydraulic fracturing to understand what mechanisms drive fracture growth, process zone, and breakdown pressure. To briefly review them, Alvaro Ortiz (2010) and Camilo Moreno (2011) assessed microseismic mapping and location uncertainties in uniaxial experiments. Akash Damani (year) performed triaxial testing with different injection rates, fluid types, and rock mineralogy. Insights were gained on what parameters drive formation breakdown pressure and produce higher permeabilities and larger process zones. Swetal Patel (2017), Christopher Ratzlaff (2019) and Saurabh Goyal (2019) used the triaxial set-up and performed pre- and post-cyclic injection, noting further reductions in breakdown pressure and an increase in the stimulated reservoir volume. The latest studies attempt to take microseismic one step further and analyze attributes of acoustic emissions to understand types of failure mechanisms.

## 2.3 Fluid's Injection

Large quantities of fluids are injected into the subsurface before and during hydraulic fracturing jobs. Acids and fracturing fluids are pumped to clean and induce pressure. One of the main concerns is understanding the effect fluids will have on a formation and how they impact it both chemically and mechanically.

Wick et al. (2020) showed the mechanical damage caused by different acids (HCl, citric and formic) on samples with high quartz, carbonate, and clay content using nanoindentation. The

observations proved formation degradation under acid exposure. There was mineral removal on the surface, especially on the carbonate-rich sample, which significantly damaged the surface by leaving a patchwork frame and decreasing Young's modulus by as much as 80%. Such a decrease can lead to proppant embedment and integrity issues in near-wellbore stability.

The water weakening effect on rocks has been studied, addressing reduction by as much as 70% on Young's modulus and uniaxial compressive strength (Colback and Wiid, 1965; Almassodi et al., 2014; Gupta et al., 2018). These effects are dependent on different conditions such as temperature, salinity, and fluid additives, which can either trigger reactions and increase damage or reduce the rock-fluid interaction (Akrad et al., 2011; Lyu et al., 2018; Signh et al., 2019).

Harrison et al. (2017) showed how mineralogy is the driving component of rock-fluid behavior (shales) on the geomechanical side. Their fracturing fluids dissolved calcite and pyrite, generating hydroxides that could block pores and affect fracture connectivity. Luo et al. (2021) observed pyrite oxidation, clay hydration, and swelling as the main factors in shale softening and degradation.

From a mechanical perspective, Chen et al. (2019) analyzed the effect of water-based rock and fluid interactions. A significant reduction in fracture toughness and fracture growth index was observed with increased water content for Woodford samples, even though smectite was low. The opposite case was observed for carbonate-rich samples (Marcellus), where the water effect was insignificant. Clay-rich samples have a high probability of failure with water-based fluids due to subcritical fracture growth. Lyu et al. (2018) showed a considerable reduction (70%) in uniaxial compressive strength after water saturation in the Shichuan Basin shale samples with low clay content. Salinity content was determinant in partially recovering the decrease in UCS; having higher salinity concentrations reduced the UCS reduction. KCl was the most efficient salt to avoid

weakening. At a concentration of 25% KCl, the UCS reduction was only 20%, compared to NaCl and $CaCl_2$ where the reduction was 40%.

## 2.4 Fracture Initiation and Propagation

Production in unconventional reservoirs has many challenges. A suitable fracturing protocol optimizes parameters such as breakdown pressure and contacted surface area; however, fracture propagation is still affected by layering and laminations in reservoirs (Suarez-Rivera et al., 2016). The layering refers to reservoirs with thick enough formations to be targeted, while laminated refers to thin below log resolution. Understanding mechanical properties in multilayer reservoirs, especially the contrast between the landing zone and the adjacent layers, is critical in overcoming poor fracture propagation and fracture connectivity.

Philipp et al. (2013) showed a detailed analysis of the main factors that affect hydraulic fractures. Discontinuities, defined as a break or fracture of low or zero tensile strength, and stress barriers, defined as layers with unfavorable stress conditions for fracture propagation, were considered the least favorable factors for a hydraulic fracture. The relation between mechanical properties (e.g., Young's modulus and Poisson's ratio) and the stress state of rock control the fracture propagation of different layers. As the fracture tip moves toward an open contact, it either propagates along the contact or stops. These observations also occur in volcanic regions, where ash beds are common. Volcanic ash beds are heterogeneous thin layers commonly observed in unconventional formations with diagenetic alterations and sedimentary structures, making them act as barriers that affect fracture propagation (Calvin et al., 2015; Suarez-Rivera et al., 2016).

Luo et al. (2018) investigated the effect of bedding plane orientation on fracture mechanics (fracture propagation and fracture toughness) on a dry Longmaxi shale. When the crack was propagating at small bedding plane inclinations, the fracture initiated and propagated along the

same crack line; however, when the angle increased, the crack initiated along weak bedding planes. Fracture toughness was lower for crack propagation along bedding planes.

Other industries have similarly analyzed crack propagation. Kim et al. (2005) examined the crack behavior across interfaces in ceramic dental bilayers, contrasting elastic properties between each layer. They noted that cracks arrested at the interface when traveling from low to high Young's modulus. The opposite case was noted when traveling from high to low Young's modulus, which enhanced the crack propagation. Using microindentation cracks in soda-lime glass, Rosenfeld et al. (1990) showed the direction of crack propagation to depend on the distance to the interface and using finite element modeling (FEM), they showed the propagation angle to depend on the elastic moduli difference.

## 2.5 Creep Properties

Once the fracture network is created, proppant is pumped into the fractures to keep them open while hydrocarbons are extracted. However, due to high stresses to which propping sand is subjected, proppant crushing, and embedment are common and likely issues. Understanding the plastic deformation properties of each layer becomes the key to maintaining production. Commonly known as creep, this property is defined as the permanent deformation of a material over long times and under constant loads. This property can be impactful depending on external factors such as temperature, loads, and material composition. ***Fig. 2.2*** shows the three phases of creep in a curve of strain as a function of time. Primary or transient creep consists of a rapid deformation in a short time, where the strain is relatively high. As time progresses, primary creep transitions into secondary creep, also known as steady-state creep, due to its constant deformation rate over time. The change in strain is almost linear. Most studies have been analyzed during secondary creep, aiming to obtain the stress vs time slope as the predictor for the long-time

performance. The tertiary creep is the last stage where the strain abruptly increases, and failure occurs. After holding strain for long times in the secondary stage, strength is lost, and deformation leads to a total and irreversible rupture. Although sometimes neglected, few studies have been performed to understand creep behavior in unconventional reservoirs using uniaxial and triaxial systems.

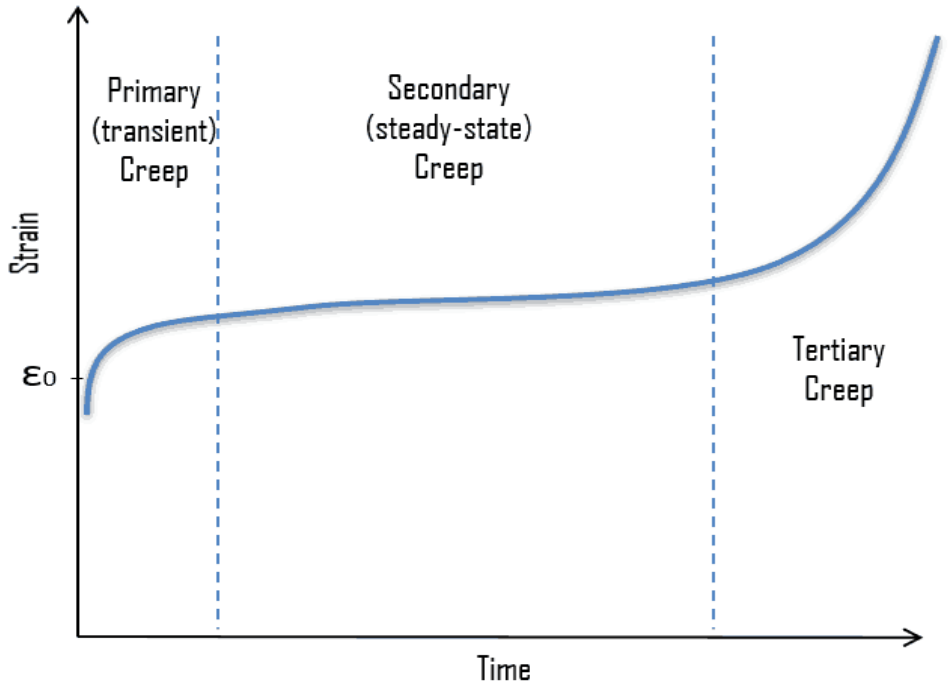


*Figure 2-2. Strain vs time curve for creep. The rapid increase in strain (primary) is followed by the steady-state creep (secondary), which is the most important phase across industry studies. The latest stage has a sudden rapid increase in strain which leads to failure.*

Sone and Zoback (2013) performed long-term (6-hours) triaxial testing on different unconventional reservoirs to analyze the creep behavior and brittle strength of shale. Viscoelastic creep strongly correlated with the rock composition (especially clays and kerogen) and the static Young's modulus. Deformation perpendicular to bedding planes was greater than parallel. In addition, Rybacki et al. (2017) studied creep behavior in Posidonia shales at different applied differential stresses. At low differential stresses, sample deformation did not reach secondary

creep, however, increasing the differential stresses not only achieved secondary creep but also reached failure.

Primary and secondary creep are better understood through modeling. Fitting the stress and strain relation using the power-law function such as $\varepsilon = \sigma B t^n$. Sone and Zoback (2014) showed how the stress exponent 'n' depended on mineralogy and anisotropy. Rassouli and Zoback (2018) performed different triaxial tests on the Haynesville formation. After performing creep tests over different time intervals, they calculated a consistent creep compliance factor, predicting time-dependent deformation in shales. Similarly, Gupta et al. (2018) used the stress exponent to compare creep behavior in different formations. The Eagle Ford formation showed higher creep compared to the Wolfcamp and Woodford.

## 2.6 Microseismics

Microseismics have been historically used to evaluate the efficiency of a hydraulic fracturing job. It is one of the principle diagnostic procedures to monitor fracture development, and it expanded towards unconventional reservoirs (Albright and Pearson, 1982; Warpinski et al., 1998; Warpinski, 2013). During fracturing testing, the pore pressure is increased until exceeding the fracture gradient, and failure is reached. During fracture propagation, energy is liberated by the opening of cracks, which liberates energy monitored with acoustic geophones. Knowing the precise location of each geophone, the compressional wave velocity, and having a certain number of signals allows the user to locate the source of a crack/fracture with relative confidence (Stein and Wysession, 2003; Moreno, 2011). A combination of the located acoustic emissions creates a fracture network map.

Whitfield et al. (2018) aimed to mitigate the frac hits in the Eagle Ford formation as they can lead to collapse casing. Microseismic was a helpful in identifying locations where wells were

communicating with each other. Mayerhofer et al. (2011) integrated fracture diagnostics in the Marcellus for improvement in stimulation efficiency. Microseismics showed locations where BHP increased at different stages and the direction at which microseismics appeared after the communication between wells occurred (***Fig. 2.3***).

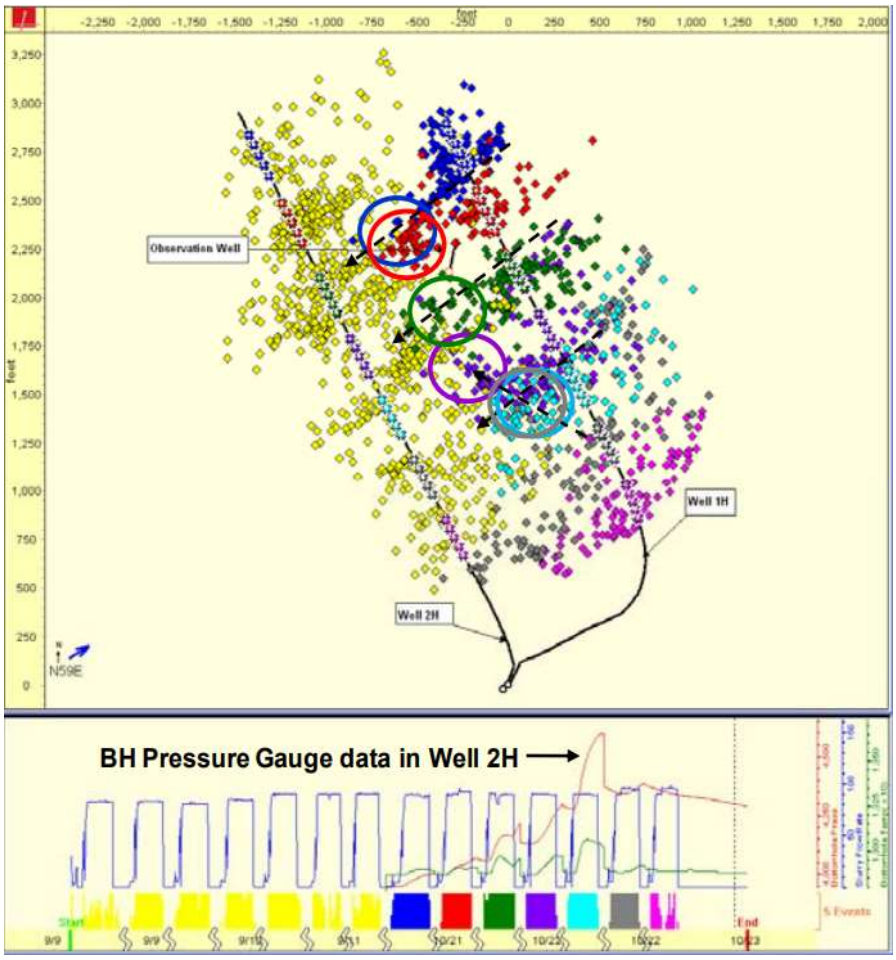


*Figure 2-3. Integration of fracture diagnostics, bottom hole pressure and microseismics for two wells in the Marcellus. Microseismic shows that according to the interference between two wells, there are changes in BH pressure. (Mayerhofer et al., 2011).*

The accuracy and precision of microseismic locations have improved over time. Their application has been used in well placement, completion design, and stimulation optimization (Warpinski, 2013). Laboratory studies have aimed to complement and validate the field observations, not only through acoustic emission locations but by performing attribute analysis on

each emission and understanding failure modes, seismic magnitudes, source radius and displacement. This section will evaluate the methodology for calculating the source parameters and insights gained.

Brune (1970) is one of the pioneers of seismic source analysis. His work contributed to calculations on the source radius using the frequency response and moment magnitudes. Source radius is the first parameter calculated using the corner frequency Fc and shear wave velocity Vs. The corner frequency, defined as the separation between the low and high frequency in the displacement spectrum, or center frequency in the velocity spectrum, was calculated by taking the Fourier Transform of the displacement spectrum (Papageorgiou, 1988; Warpinski et al., 2012).

Evaluation of acoustic waves in the frequency domain offers information about the event that is not apparent in the time domain cannot. Bakker et al. (2016) conducted laboratory experiments to analyze the dyke injection at elevated pressure and temperatures of an Etna basalt. They found similarities in pre-breakdown events to classical volcano-tectonic waveforms; however, events after failure exhibited a low-frequency response. Mohamed Bak et al. (2016) characterized failure modes uniquely based on the frequency signal of single lap joint basalt/epoxy specimens. The acoustic emissions were recorded with piezoelectric sensors with frequencies of 100-900 kHz. A threshold was set to classify events as an adhesive failure or a shear failure using the peak of the frequency spectra (***Fig. 2.4***).

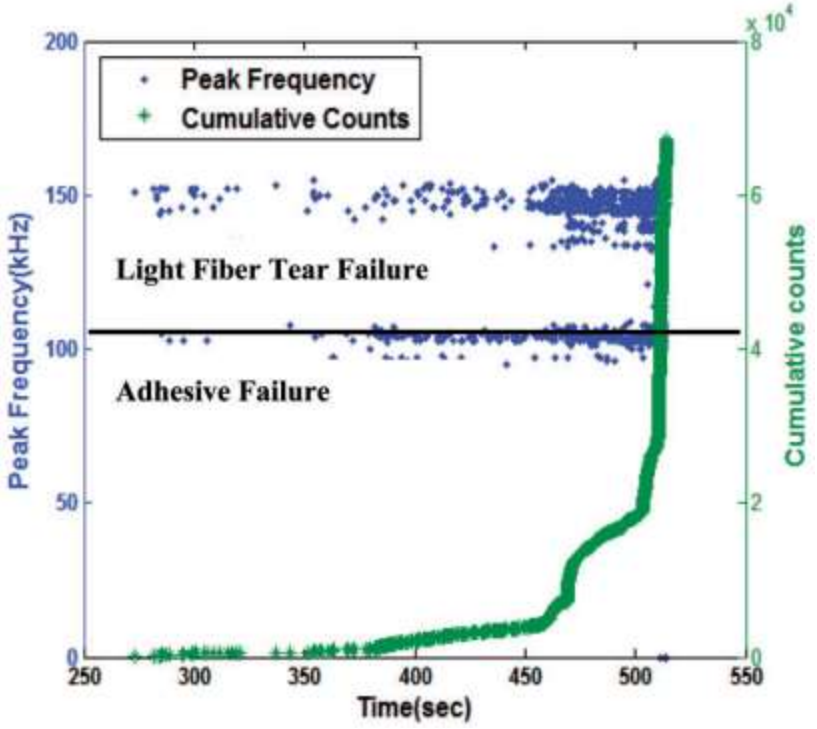


*Figure 2-4. Peak frequency spectra as a function of time. This is used to differentiate between the light fiber tear failure and adhesive failure in single lap joint basalt/epoxy (Bak et al., 2014).*

The seismic moment is an estimate of the energy release by a crack. It is calculated using ***Eqn. 2.1***, where ρ is the density, R is the distance between the crack and the receiver, Ω is the low-high displacement spectrum, Fc is the radiation pattern factor, and Vs is the shear wave velocity. The seismic moment is probably the most critical attribute from a seismic event, as it is used to obtain other parameters such as stress drop or displacement slip on the fracture plane, and it opens insights on events failure. The moment magnitude is a method to scale it, and it is also derived from the seismic moment.

$$M_o = \frac{\Omega_o}{R_{o\emptyset}} 4\pi\rho R V_p^3 \quad \text{.....(2.1)}$$

Baig and Urbancic (2014) studied two cases with acoustic events from the Horn River Basin and the Eagle Ford and showed the complexity of characterizing seismic events. They showed that large-magnitude events tend to be shear-driven, while small magnitudes represent fluid-driven signatures. An emphasis is made to consider the low frequency of the signal when

obtaining parameters such as corner frequencies, as this can underestimate the moment magnitude. A direct correlation was found between seismic moment and source radius.

Zecevic and Eaton (2017) used moment magnitudes and corner frequency to classify acoustic events in the Barnett. Based on the relationship of Fc and Mw, two clusters were identified, one having greater moment magnitudes than the other. Those clusters showed that events with smaller magnitudes mainly show low double couple components, classifying them as tensile. Events with higher magnitude show a greater double couple (%) and are expected as shear events.

Mizuno et al. (2019) proposed an approach to monitor static stress drop and rupture velocity changes by combining the corner frequency and seismic moment in the Barnett Shale and Cotton Valley. The changes in seismic moment were explained with variations in the static stress drop and rupture velocity, which allowed for the interpretation of properties such as permeability. They recorded a constant moment during the development of the hydraulic fracture system for the Barnett Shale; however, the Cotton Vale showed an initial increase in moment followed by a decrease towards the end of the fracture development. The increase was explained by the rise in permeability.

Warpinski et al. (2012) reviewed microseismic information of multiple treatments for six basins in the United States. Using Brune's (1970) model for calculating magnitudes, they observed that seismic magnitudes trend with depth in the Barnett, Woodford, and Eagle Ford, which suggested a dependency between the seismic magnitude and stress conditions (Zang and Stephansson, 2010). However, this trend was not repeated for the Marcellus formation. A direct correlation was observed between the slip area and the Zang and Stephansson (2010) seismic moment; the higher the magnitude, the greater the slip area. The Barnett exhibited the highest

moment magnitudes, while the Marcellus was the lowest. In a similar study, Warpinski (2012) showed that most of the events recorded during hydraulic fracturing have magnitudes in the range of -3.0 to 1.0, which in terms of energy is 1,000 times smaller than events felt at the surface. These events are not likely to cause earthquakes.

# 3. NANOINDENTATION

Over the last decade, industries have improved their technology and started developing small size materials. Thin films and coatings are some examples of the materials that universities and industries analyze. Generally, these materials require mechanical testing before being used in semiconductor devices, solar cells and integrated circuits. Uniaxial and triaxial testing are conventional techniques for measuring parameters such as elastic modulus, while Brinell and Vickers hardness are applied for hardness measurements. However, these techniques are not capable of assessing materials on the order of micro- and nanometers. Oliver and Pharr. (1992) developed a method that works in small size materials and outputs both elastic moduli and hardness, called nanoindentation. The depth of penetration is measured using a three-plate capacitance displacement gage (***Fig. 3.1***). A diamond tip is placed at the indenter end, which changes in geometry according to its application. Indenter tips such as the Berkovich or Vickers are used for shallow indentation, while spherical indenters are more commonly used in defining yield stress (Bhushan and Li, 2013).

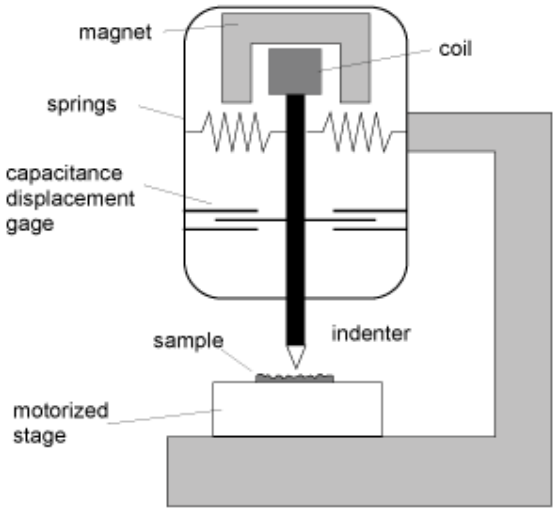


*Figure 3-1. Schematics of a nanoindenter. The coil and magnet create a load applied by the indenter tip. The displacement is measured with the capacitance displacement gage (VCU Engineering, Nanoindentation).*

***Fig. 3.2*** describes the loading process, starting with the indenter tip contacting the sample surface, and gradually increasing the load until the desired limit. The tip is then held for a finite time (can be 10 seconds) and unloaded. During the tip release, the elastic moduli and hardness are obtained. The tip size is small allowing multiple indentations to be placed on the surface, which is important in heterogeneous materials. Additionally, the grain size needs to be significantly smaller than the indentation area. Although not as frequent, other properties such as creep and fracture toughness have also been quantified (Schiffmann et al., 2011; Liu et al., 2015; Mighani et al. 2015).

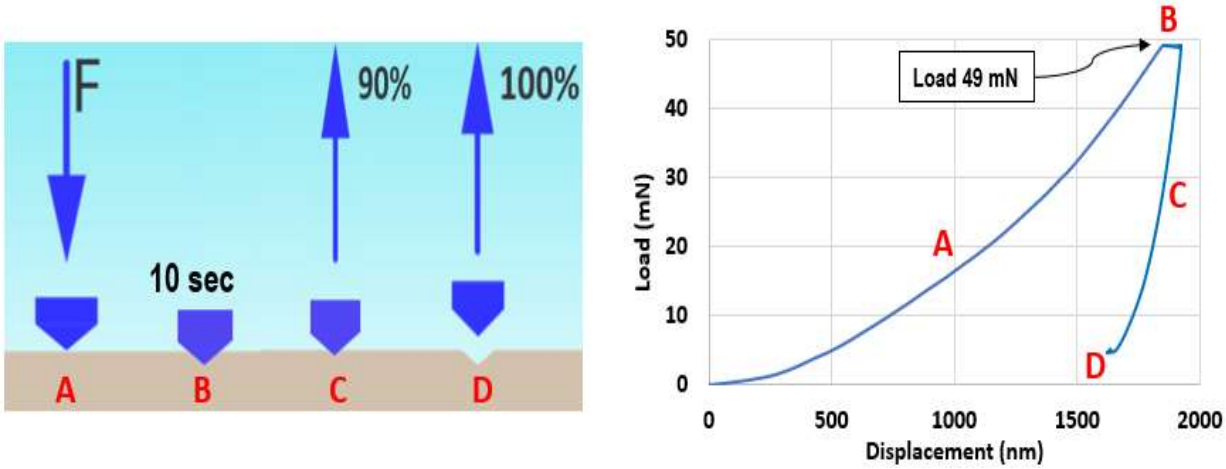


*Figure 3-2. Left) Indenter tip steps in a sample surface. Right) Loading curve as a function of displacement for one nanoindentation. A) indenter loading; B) holding time; C) unloading; D) drift coefficient measurements (Acosta et al., 2020).*

Because of shale friability, mechanical properties are often difficult to obtain as core samples are challenging to acquire. Shales are very heterogeneous with small grain and pore sizes (nanoscale), allowing the use of cuttings of readily available chips. In the following sections, analysis of creep behavior under saturated conditions, the effect of fracturing fluids on mechanical properties, and the contrast in elastic parameters between the ash beds and the formation matrix will be discussed.

## 3.1 Fracturing Fluids on Mechanical Properties in Wolfcamp

Rock and fluid interactions are a main area of study in completion operations. Understanding the formation response to injected fluids can improve completion designs, especially in hydraulic fracturing operations, where different fluid compositions are used. Previous studies have reported interactions between acids and brines with the formation matrix; however, there are limited studies on fracturing fluids. Large quantities of fracturing fluids are injected in each operation and their selection is crucial. Fluid viscosity controls fracture initiation and propagation. After completion, large amounts of fluid remain in the subsurface, leading to strong rock-fluid interactions. This study quantifies the effect on mechanical properties caused by reactions between common fracturing fluids and the formation, considering parameters such as additive concentration, saturation time, and formation mineralogy.

### *3.1.1 Formation Evaluation*

The Permian basin is a large sedimentary basin located in Texas and the southeast of New Mexico. It contains numerous reservoirs mainly composed of limestone, sandstone, and shale. With a depth range between 7500 to 10000 ft and an area of about 75000 $mi^2$, it is a thick formation with strong prospect zones for production. This is the largest oil-producing basin in the United States (*"Permian Basin – Major Oil and Natural Gas Field", 2013*). Companies such as Exxon, OXY, BP, and Pioneer have assets in it. Some formations, such as the Avalon Shale, Leonard Shale, Bone Spring, Spraberry, and the Wolfcamp, are all within the Permian. The Wolfcamp is located at the bottom of the basin and is just above the Strawn formation, a carbonate (***Fig. 3.3***). The formation can reach temperatures around 170-200 ºF, a factor to be considered in this study.

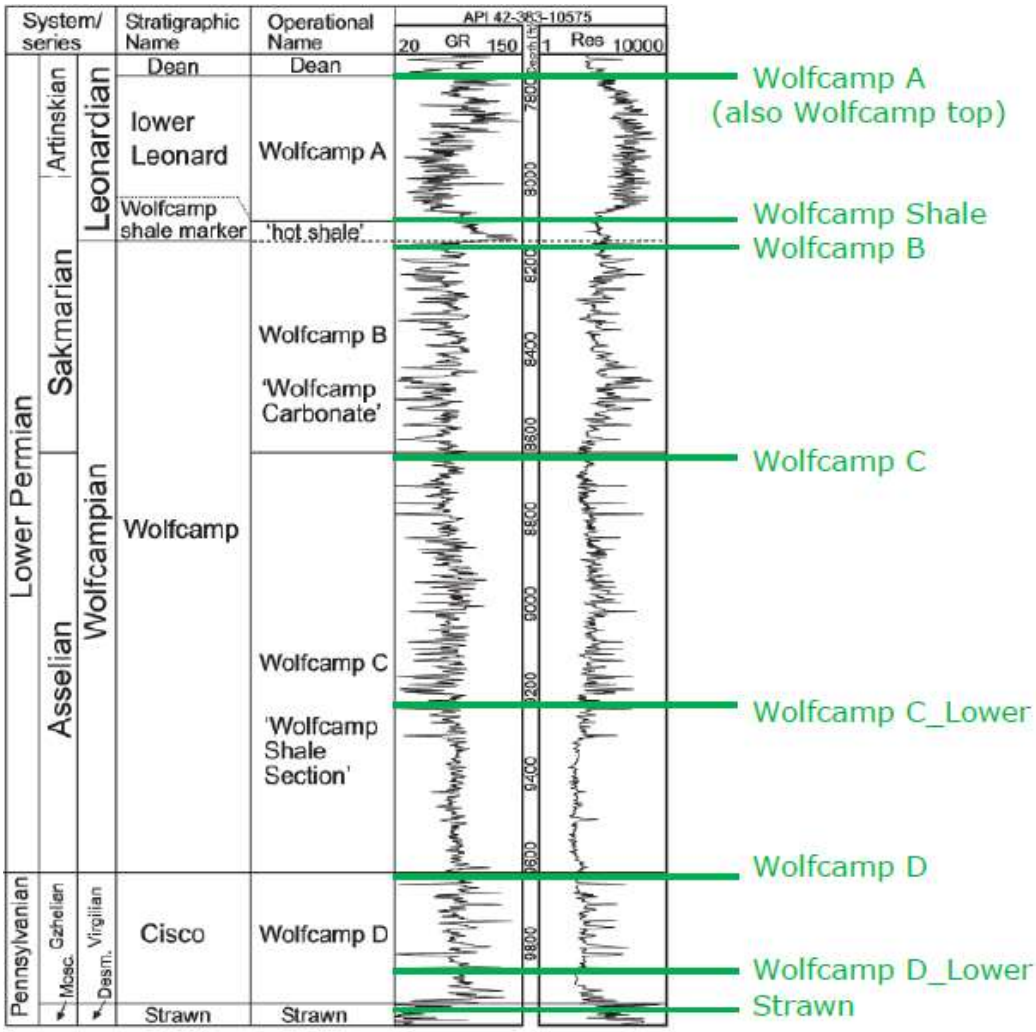


*Figure 3-3. Permian Basin depth diagram. IHS Energy (2016).*

### *3.1.2 Methodology*

A total of 12 samples were chosen for indentation and Scanning Electron Microscopy. Seven were selected from the Wolfcamp formation and five from the Strawn. A 1-in diameter disc was sliced from a plug with a thickness ranging between 0.2 to 0.3-in. The discs were cut in four pieces to accommodate multiple tests (***Fig. 3.4a***): 1) Native measurements, 2) Slickwater saturation, 3) Linear gel saturation, and 4) petrophysics. Saturation was done for 24 hours at a pressure of 1,000 psi. In ***Fig. 3.4b,*** saturating fluid filled the cup holding the sample to maintain saturation while running the indentations.

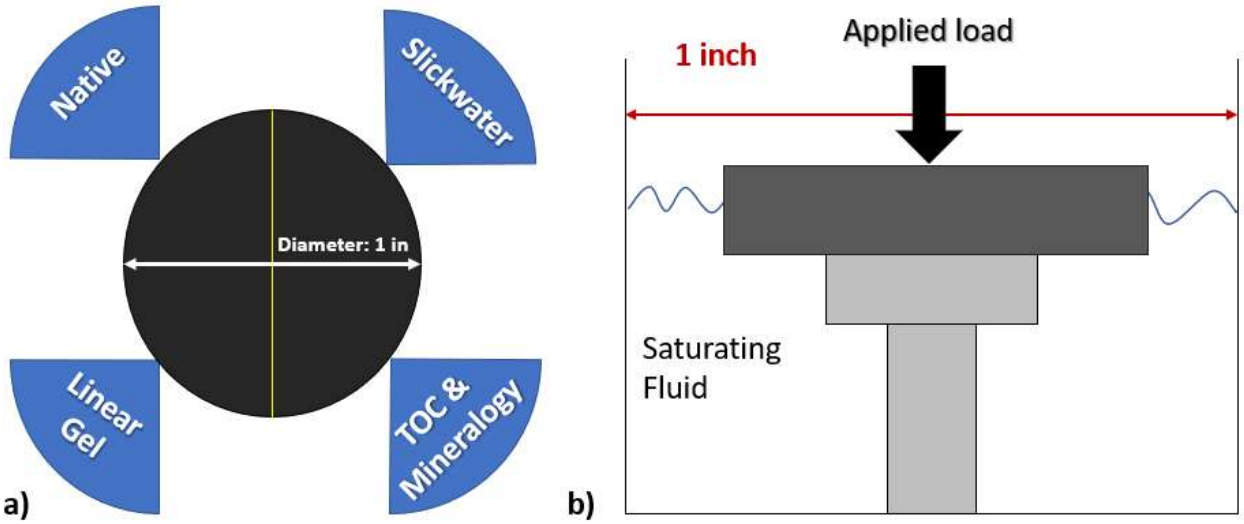


*Figure 3-4. a) Illustration for disc testing at different saturation conditions. b) Stub protocol to hold the sample under saturation while performing nanoindentation.*

Slickwater and linear gel were chosen for testing as they are two of the most common fracturing fluids used in hydraulic fracturing operations. Slickwater is a low viscosity fluid, that yields high fracture conductivity. On the other hand, the linear gel has a greater viscosity, which helps proppant transport and fluid loss control. The pH of the slickwater and the linear gel were 7.8 and 4.9 respectively. Other fluids used in the field, such as crosslinkers, are less common, more expensive and were not considered in this study.

Rocks were dried at 100 $^{O}$C. Indentation arrays of 5x5 were randomly placed on the sample surface. The maximum load was set to 490 mN, with a holding time of 10 seconds. The effect of fluids on Young's modulus and hardness were studied.

The slickwater consisted of 120 ppm each of friction reducer and a clay stabilizer. The main component in the linear gel was guar, at a concentration of 2400 ppm, while the gel breaker used was ammonium persulfate at 60 ppm. These values were chosen by Schlumberger, who provided the fluids with predetermined concentrations based on their field use.

### *3.1.3 Petrophysics*

One of the sample fractions was selected for petrophysical measurements. TOC and mineralogy were run using the same methodology as in Section 3.1.3. The Wolfcamp formation showed a considerably higher TOC (1.5 – 6.8 wt%) than the Strawn (0.6 – 1.2 wt%). In addition, Wolfcamp samples showed variations in mineralogy, with low and high clays, carbonates, and quartz. The Strawn formation was carbonate-rich (over 70 wt%), with low porosity as shown in ***Table 3.1***.

*Table 3-1. Detailed composition for the Wolfcamp and Strawn samples. The Wolfcamp formation has a variation in mineralogy, while the Strawn is very carbonate-rich and low in TOC. All mineral and TOC percentages are weight percentages.*

| Permian | # Samples | TOC | Clays | Carbonates | Quartz | Feldspar | Porosity (%) |
|---|---|---|---|---|---|---|---|
| Wolfcamp | 7 | 1.5 - 6.8 | 15 — 60 | 5 — 60 | 13 — 36 | 2 — 39 | 7.3 — 10.3 |
| Strawn | 5 | 0.6 - 1.2 | 2 — 19 | 70 — 87 | 1 — 11 | 0 — 9 | 2.5 — 3.2 |

### *3.1.4 Results*

***Mechanical properties response under fracturing fluids***

The native samples were indented, and Young's modulus was plotted against mineralogy. with the results were consistent with previous data from Shukla et al. (2013). Due to the high carbonate content, Strawn showed a higher Young's modulus, ranging from 70 to 80 GPa, while the Wolfcamp moduli ranged between 30 to 50 GPa (***Fig. 3.5***). A direct proportionality was observed between the moduli and quartz and carbonate, while samples with higher clay content had lower Young's moduli.

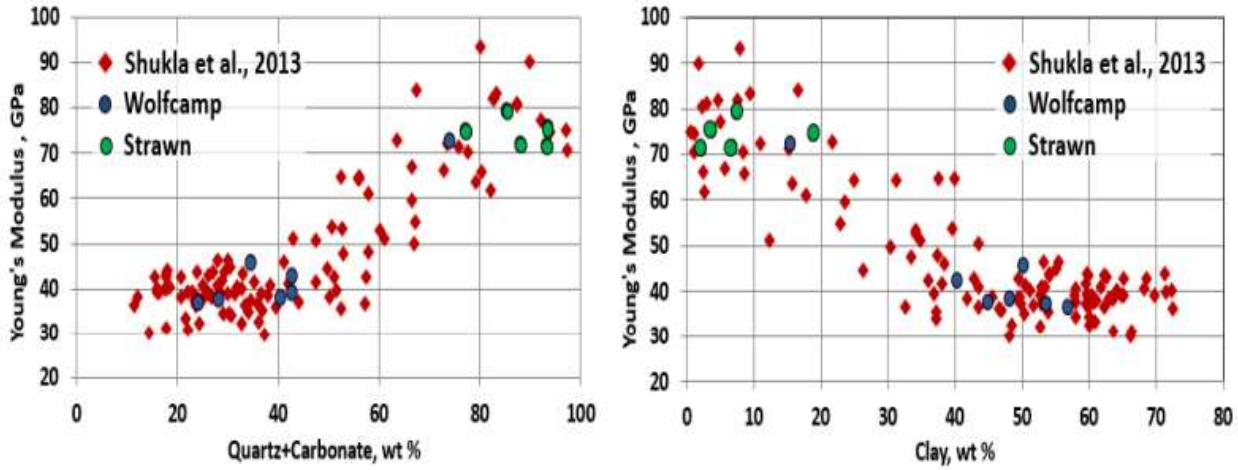


*Figure 3-5. Young's modulus as a function of quartz and carbonates (left) and clay and TOC (Right). The current data matches historical measurements performed by Shukla et al. (2013). The Strawn and Wolfcamp are measurements from this study.*

***Fig. 3.6*** compares Young's modulus of the native state with those of the saturated samples. High carbonates (> 60 wt%) samples were the most affected. A decrease in Young's modulus of 21% under slickwater and 31% under linear gel was measured. On the other hand, low carbonates samples showed a 6% decrease with slickwater and 22% with linear gel. This suggests more damage with linear gel than under slickwater, independent of the carbonate content.

Hardness results were identical to those observed for Young's modulus (***Fig. 3.7***). The lowest hardness was observed using linear gel, decreasing in almost every sample (independent on carbonate content) by more than 50%. Sample 8 (Strawn) had a higher hardness after saturation, but it also had a high standard deviation. Slickwater also decreased hardness after saturation, suggesting an increase in the plastic deformation, yet it was not as significant change.

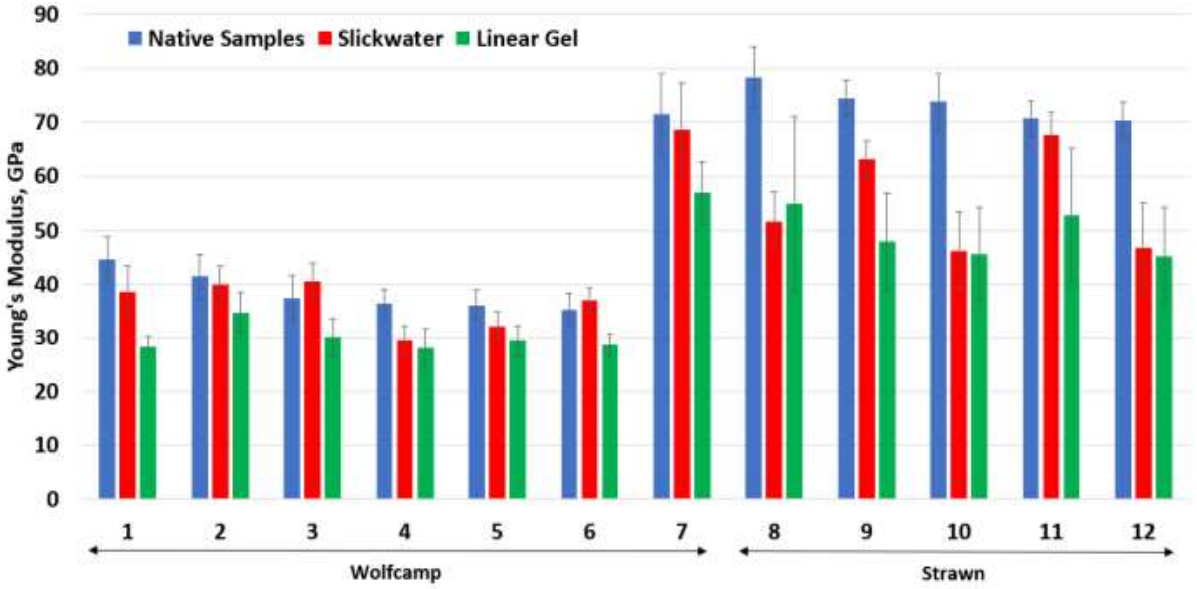


*Figure 3-6. Bar chart on Young's modulus for the Wolfcamp and Strawn samples showing the native sample (blue), slickwater saturation (red) and linear gel (green) responses. Note the standard deviations are marked with the error bars. There is a greater Young's modulus decrease using linear gel than slickwater. Carbonate-rich samples (7-12) were the most affected.*

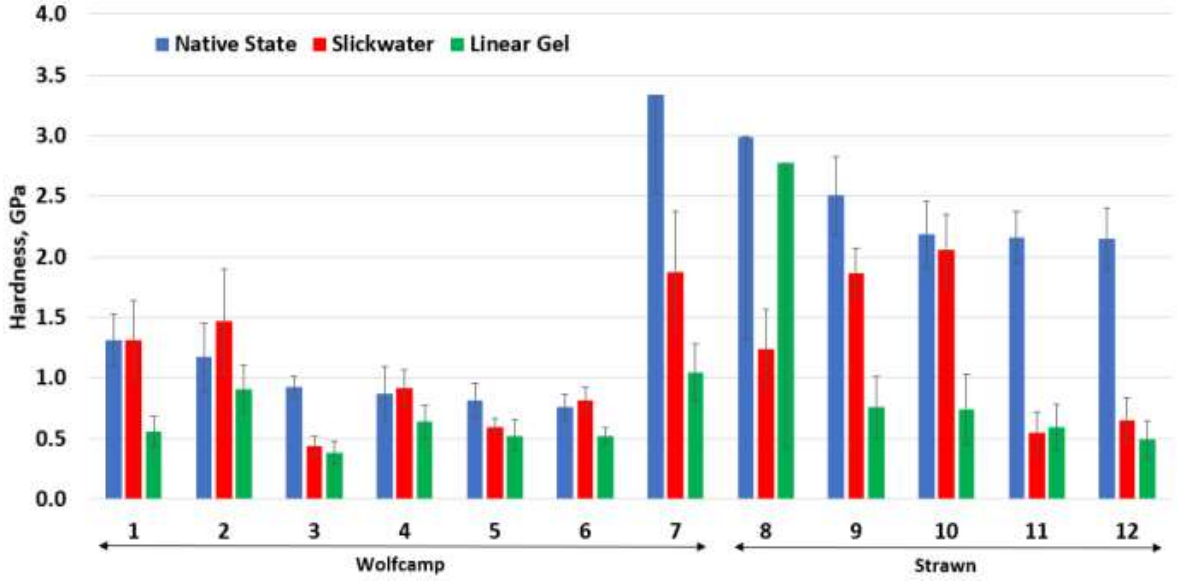


*Figure 3-7. Bar chart showing hardness reduction after saturation. Note the Strawn has a greater decrease in hardness than the Wolfcamp. The linear gel caused the greatest damage.*

### *Scanning Electron Microscope*

In order to understand the possible microstructural changes, low and high carbonate samples were examined under the Scanning Electron Microscope. Backscattered images were

taken before (left) and after (right) saturation with each fluid. The yellow triangles represent the size of an indentation with respect to the scale image.

***Fig. 3.8*** shows the effect of slickwater. In the top row, images at a 40-µm scale showed small grain boundary dissolution for the low carbonate sample (red arrows). At the bottom row, slickwater had a different effect on the high carbonate sample. Extensive grain boundary dissolution and some etching were observed. The boundary dissolution could weaken the rock matrix and reduce Young's modulus in high carbonate samples, explaining the decrease observed in ***Fig. 3.6***.

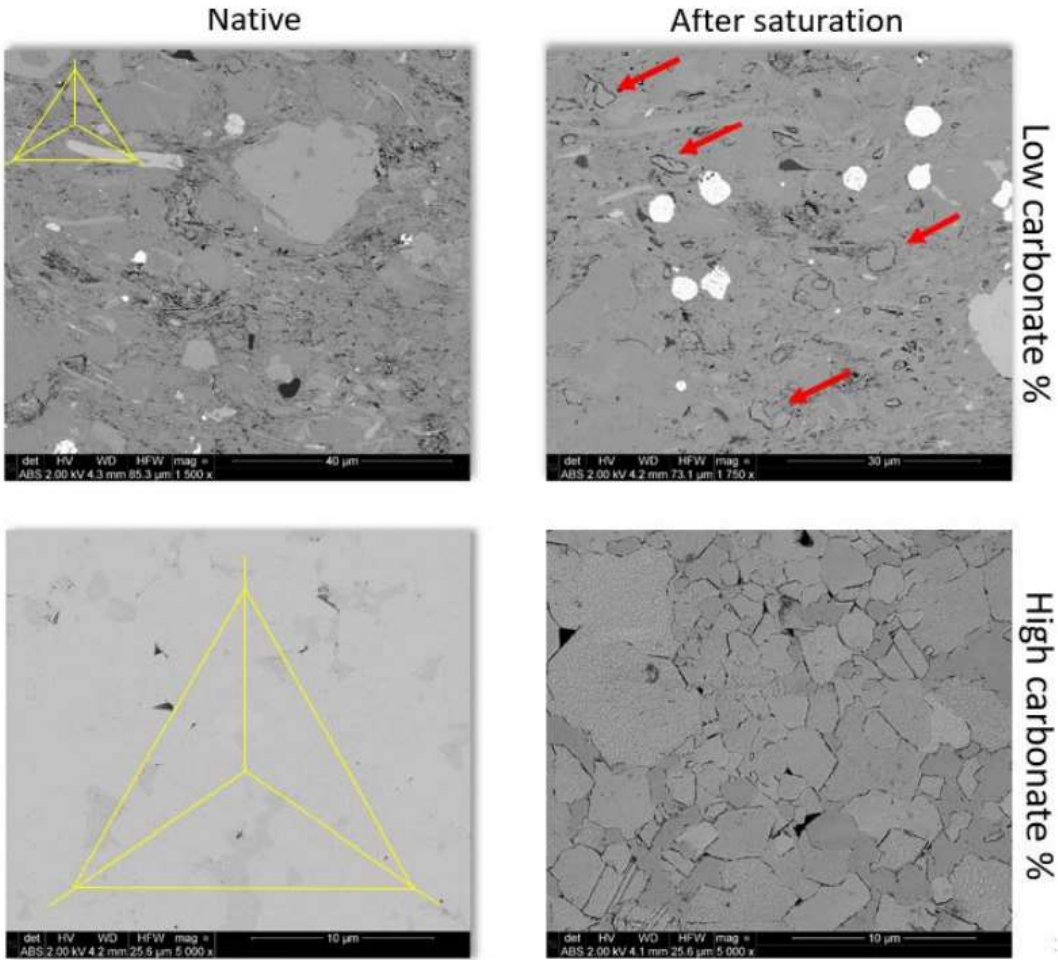


*Figure 3-8. SEM Imaging for slickwater saturation. Native samples are in the left column, while saturated samples are in the right. Small grain boundary dissolution is noted in the low carbonate sample (top row), while etching and extensive boundary dissolution is noted for the high carbonate sample (bottom row). These images were not taken at the same location but have similar scales.*

To better understand surface changes on the sample saturated with linear gel, the magnification was increased 5 times in some affected areas (from 5000x to 25000x). This exposed that not only grain boundaries were being dissolved, but that etching had occurred on the surface of some minerals (***Fig. 3.9***).

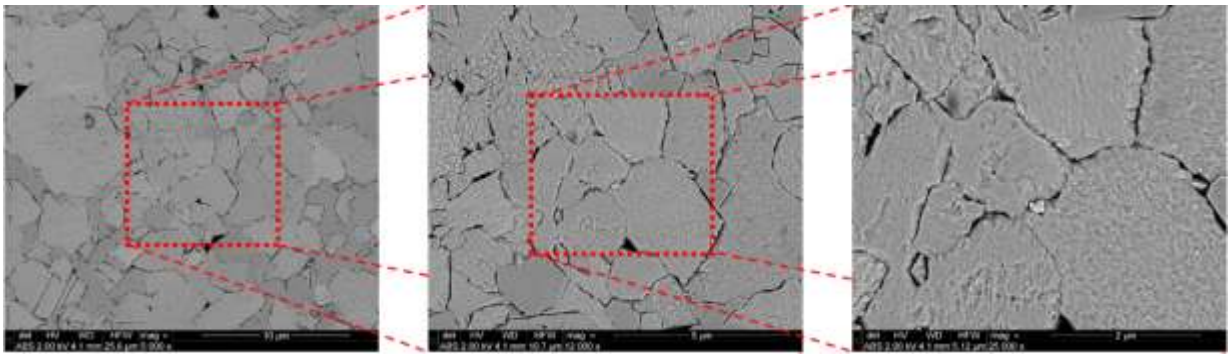

*Figure 3-9. Series of SEM images for a high carbonate sample saturated under slickwater, increasing in magnification from left to right. Higher magnifications expose etching and grain boundary dissolution (right image).*

***Fig. 3.11*** shows the effect of the linear gel on the surface. In low carbonates (top row), empty spaces appeared after saturation. It suggests that some minerals were dissolved and removed, explaining the further reduction in Young's modulus as porosity is increased. A chemical reaction also occurred, which led to guar deposits on the surface. It also revealed the most damaging and substantial reaction between the high carbonate sample and linear gel (bottom row), which significantly altered the surface. Etching and mineral removal occurred all over the sample, but quartz grains did not suffer from the linear gel exposure.

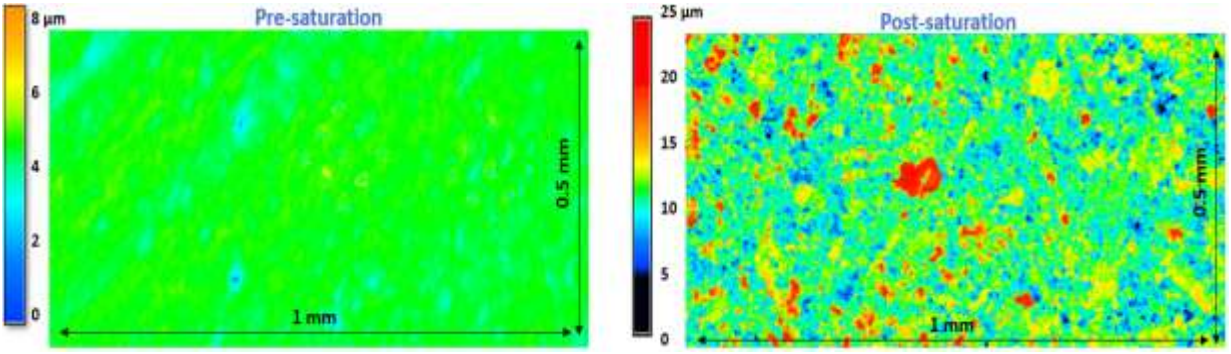


*Figure 3-10. Surface roughness change after linear gel saturation on a high carbonate sample using confocal microscopy. Note the depth changes in the surface map.*

Surface roughness was calculated using the chromatic confocal microscope, by obtaining the root mean square roughness ($R_{rms}$) in an area of 0.5 $mm^2$ pre- and post- saturation. After saturation, there was 10 times increase in surface roughness (***Fig. 3.10***), suggesting more roughness created in the fracture surface under linear gel exposure.

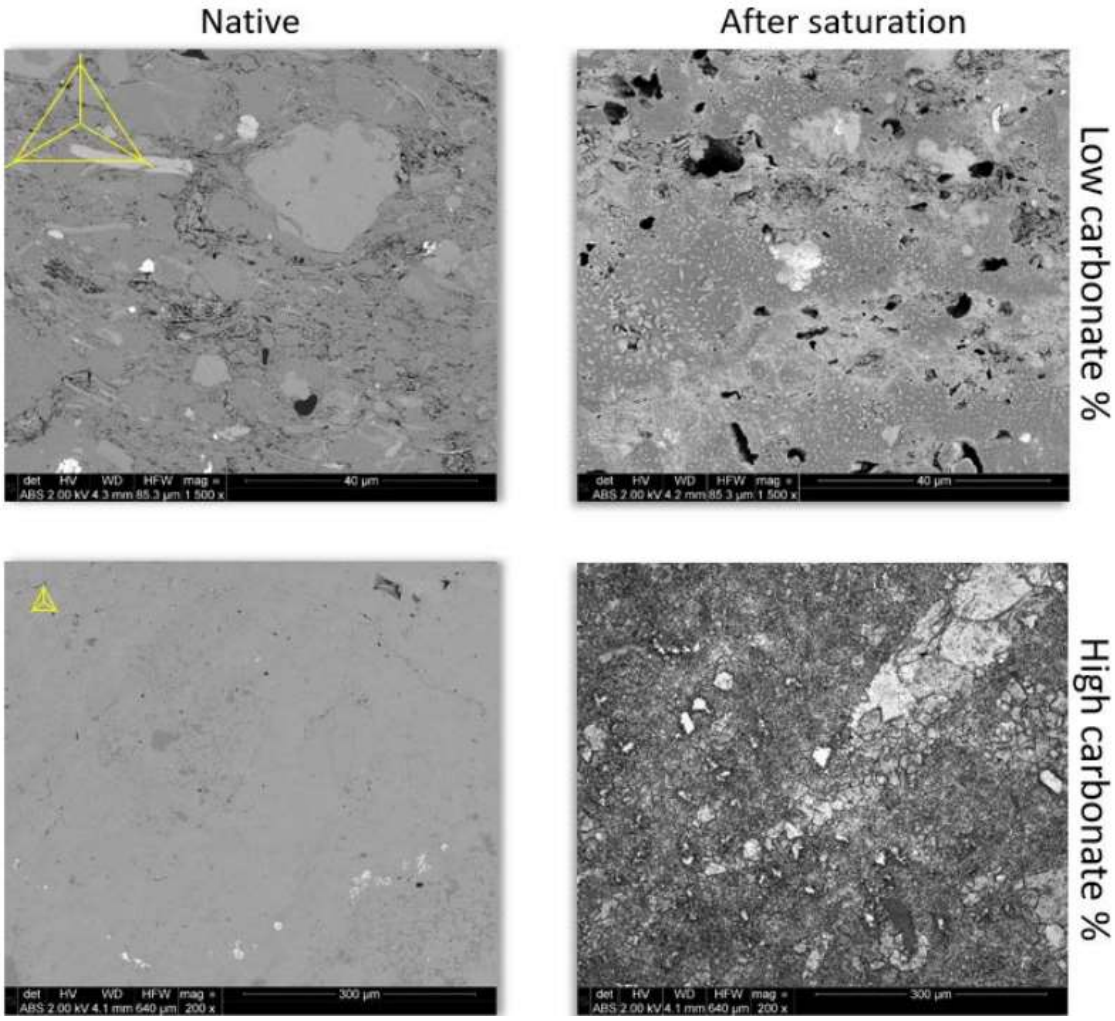


*Figure 3-11. SEM image under linear gel saturation. Both low and high carbonate samples were impacted by linear gel exposure. Note that low carbonate samples have small grains being dissolved (black color), while the high carbonates (bottom row) have etching and massive grain boundary dissolution. The carbonate removal can lead to increased porosity.*

Higher magnification images were taken of the linear gel saturated samples, as there was a more aggressive reaction. Increasing the magnification by 50 times showed carbonate residuals and quartz grains in detail (***Fig. 3.12***). Carbonates seem to be affected; however, the two silica crystals remain intact. This showed massive carbonate dissolution.

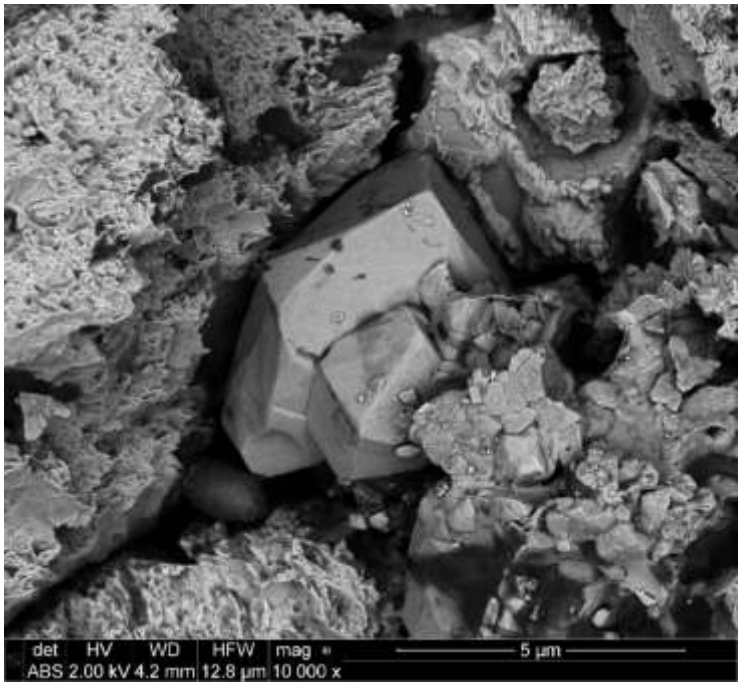


*Figure 3-12. SEM Imaging on a high carbonate sample after linear gel exposure. Note the intact silica grains in the center, while carbonates were dissolved.*

Considering that some minerals were dissolved under linear gel saturation (pH=4.9) images, an additional sample was prepared, and SEM images were taken at the same magnification and location before and after saturation. A low carbonate sample was used with three main carbonate types: ferroan dolomite (red), dolomite with ferroan dolomite (yellow), and calcite (green). After the 24-hour saturation, every carbonate was removed (***Fig. 3.13***). Other minerals such as pyrite and clays remained stable. The carbonate dissolution becomes void space implying higher porosity.

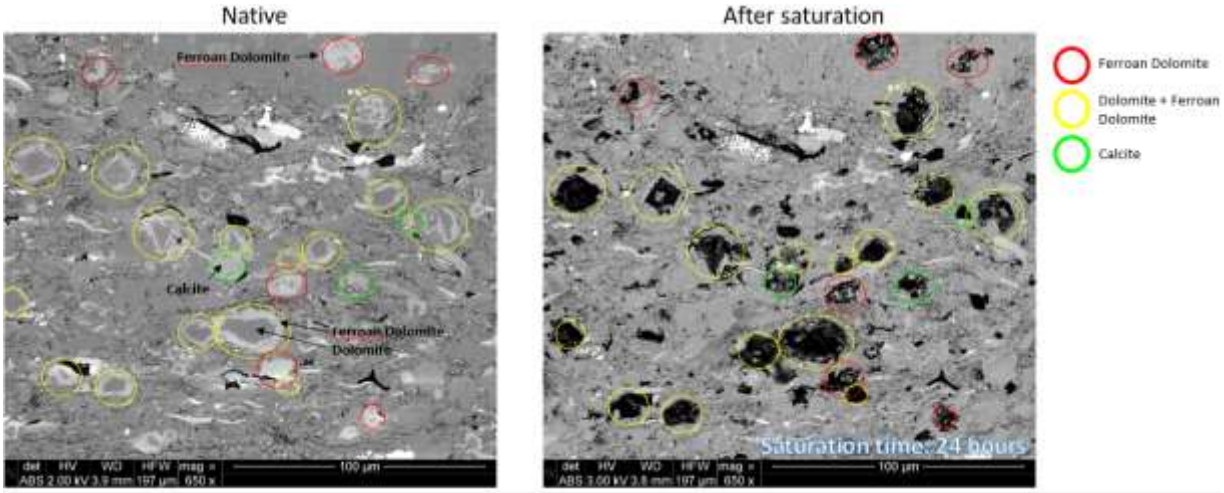


*Figure 3-13. SEM Images for linear gel saturation on a low carbonate sample using the same magnification at the same location. Not that the black holes correspond to carbonates being dissolved. Ferroan dolomite, dolomite and calcite are all dissolved.*

### *Ammonium persulfate impact*

Understanding the chemical reactions is important. The linear gel has two major components: guar and ammonium persulfate. The guar is the primary molecule, while the ammonium persulfate acts as a breaker. The temperature is significant for this reaction to occur; at 150°F thermal decomposition starts, and the molecule produces highly reactive radicals, which eventually break the acetyl linkage as illustrated in ***Fig. 3.14*** **(Montgomery, 2013)**. This reduces the viscosity of the gel, and liberates radicals, which could explain minerals dissolution.

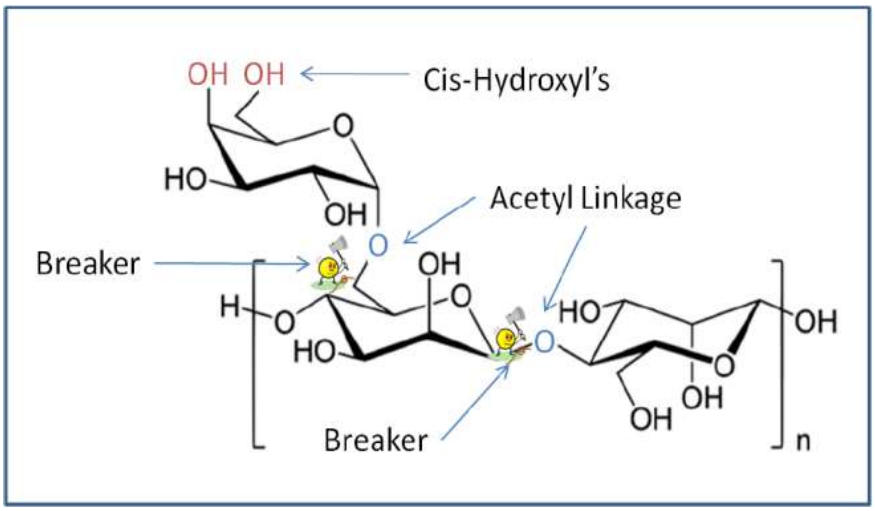


*Figure 3-14. Gel breaker reaction (Montgomery, 2013). The reaction breaks the gel molecule reducing its viscosity and liberating $SO_4$ radicals.*

***Eqn. 3.1*** and ***3.2*** show the guar molecule decomposition and the reaction between radicals and the carbonates at high temperatures (Al-Mohammed et al., 2007; Montgomery, 2013).

$$[O_3S - O - O - SO_3]^{2-} \rightarrow {SO_4}^{2-} + {SO_4}^{2-} \quad \text{.....(3.1)}$$

$$CaCO_3 + {SO_4}^{2-} + 2H^+ \rightarrow CaSO_4 + CO_2 + H_2O \quad \text{.....(3.2)}$$

Due to the high damage caused by the linear gel, three samples with different compositions were selected and used to evaluate ammonium persulfate's effect (0.5 ppt). Two fluids were used, a linear gel with and without guar presence. More damage was expected in the sample with no guar, as the ammonium persulfate would not react with guar. The samples selected were 1) a 56% clay sample, 2) a 44% dolomite sample, and 3) a 70% calcite sample (***Fig. 3.15***).

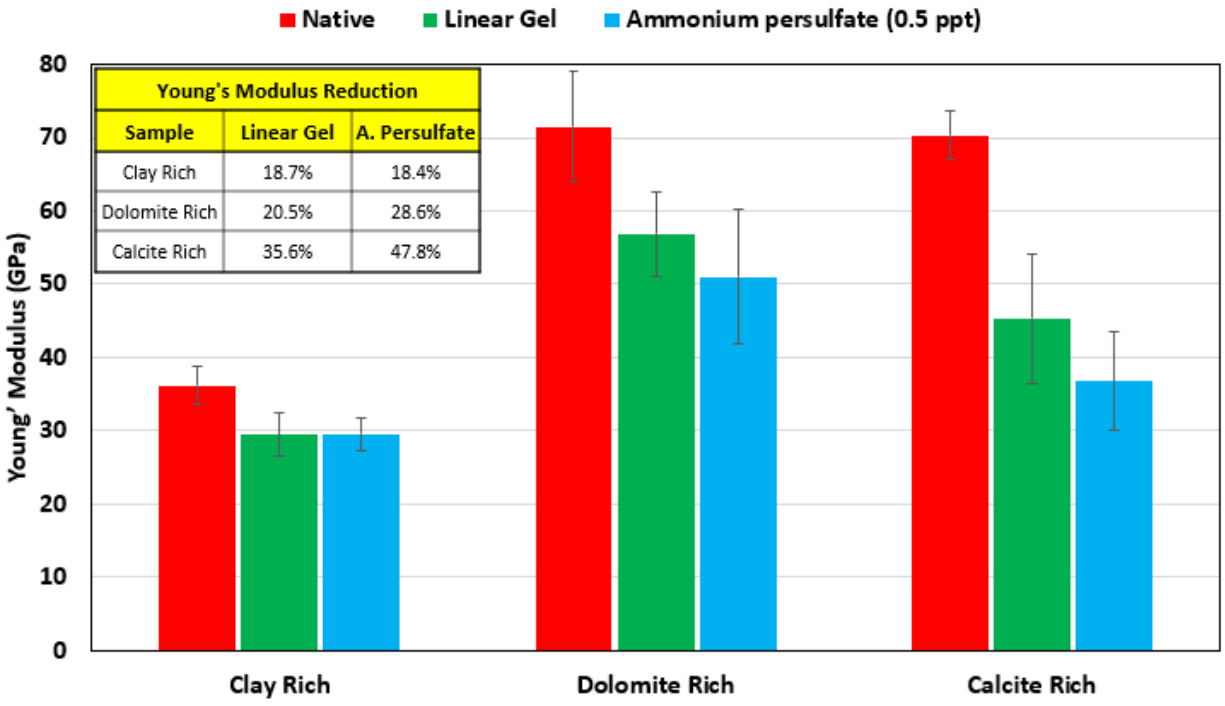


*Figure 3-15. Bar chart for Young's modulus change under linear gel (green) and ammonium persulfate with no guar (blue). Note the difference in damage for the ammonium persulfate, which is greater in the carbonate samples.*

For the clay-rich sample, Young's modulus decreased for the ammonium persulfate (18.4%) in a similar percentage as the linear gel (18.7%). This might also be due to the low carbonate composition. On the other hand, carbonate-rich samples experienced a different behavior. For the dolomite-rich sample, the decrease in Young's modulus under ammonium persulfate was 8% greater than with linear gel, while it was 12% more reduction for the calcite-rich sample. It is possible that since ammonium persulfate did not react with guar, all the radicals liberated at high temperatures were used to dissociate the shale surface.

### *Exposure Time*

Lastly, exposure time under fracturing fluid saturation was evaluated. A low carbonate sample was used, and a disc was prepared and cut into 4 pieces (*see* ***Fig. 3.4***). Each piece went through polishing and broad beam argon ion milling. Nanoindentation measurements were carried out after different linear gel saturation times: 5, 12, 24, and 72 hours. The linear gel was used as it was the most damaging fluid. The maximum time was 72 hours due to common fracturing fluids holding times in the field.

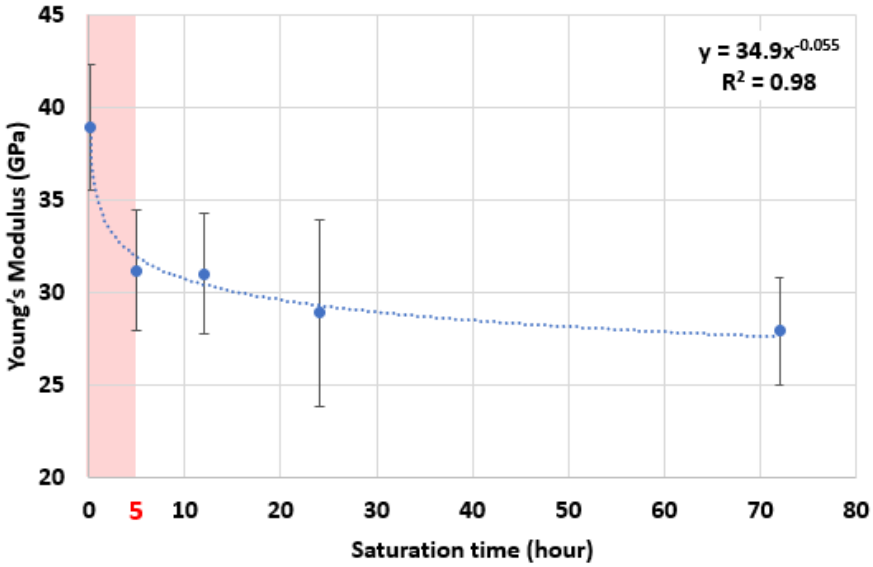


*Figure 3-16. Young's modulus as a function of saturation time (linear gel). A fast decrease in Young's modulus after 5 hours is followed by a slower but steady decrease for the next 3 days.*

As illustrated in ***Fig. 3.16***, Young's modulus decreased significantly within the first hours of saturation. Starting at 39±3 GPa, it dropped to 32 GPa within 5 hours, decreasing 20%. Young's modulus continued to decrease after 5 hours, but at a lower rate, which is essential as operators should avoid holding fluids in the subsurface for extended time periods. SEM images were retaken before and after saturation using the Energy Dispersive X-Ray Spectroscopy (EDS), for the 5- and 72-hours scenarios (***Fig. 3.17***). Only 5 hours were necessary to remove all the carbonates, which also explained the rapid reduction in moduli.

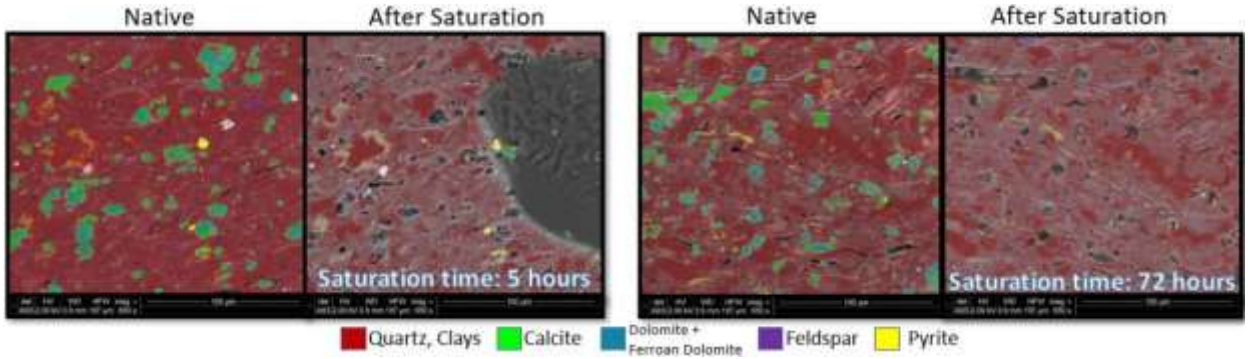


*Figure 3-17. EDS imaging for linear gel exposure during 5 and 72 hours. Only 5 hours are necessary for carbonate removal. Note that pyrite is not affected by the linear gel.*

### *3.1.5 Discussion*

Fracturing fluids are widely used but their effect on formations is poorly known. The linear gel was the most damaging fluid, weakening the sample more than the slickwater and decreasing the moduli by up to 40% for the Wolfcamp samples. SEM imaging showed surface damage when exposed to different saturation fluids. In addition, the main damaging component in the linear gel was ammonium persulfate.

When designing hydraulic fracturing treatments, special consideration should be given to carbonate-rich formations. It is important to minimize rock-fluid exposure. Young's modulus decreased even after 3 days of saturation. The decrease in rock strength and hardness can lead to common issues such as proppant embedment and reduction in fracture conductivity. Prevention of

high persulfate concentrations is necessary when using gel breakers. Lastly, different breakers should be considered, as a more neutral solution might avoid carbonate removal.

## 3.2 Brine Saturation in the Barnett Shale

Several studies have proved the application of nanoindentation in shales. Properties such as Young's modulus and hardness have been extensively studied, however, creep measurements on shales are not very common, especially using fluid saturation. Nevertheless, creep properties are helpful, as they can predict fracture degradation over time and contribute to understanding proppant embedment. This study reports measurements of creep under dry and saturated conditions using samples from the Barnett Shale. The Miller-Norton and steady-state creep equations modeled the creep displacement, creep strain and stress.

### *3.2.1 Formation Evaluation*

Located in the north of Texas at a depth of approximately 8000 ft, the Barnett Shale is one of the leading unconventional hydrocarbon producers in the United States. It is a very thick shale formation with an average thickness of 300-ft, mainly composed of quartz and clays. Due to technological advances such as hydraulic fracturing and horizontal drilling, it has become a prolific gas producer. Uses of multi-stage fracturing are common due to the formation thickness. Barnett gas reserve forecasts range from 5 to 30 trillion cubic feet *("Barnett Shale – Oil and Gas Field", 2013*). Although it is mainly known for its large natural gas reserves, it also has oil quantities that make it economically feasible. In fact, this has been referred to as a "Combo play" due to both oil and gas composition. ***Fig. 3.18*** shows the Barnett Shale Map with the hydrocarbon window based on region.


*Figure 3-18. Barnett Shale Map. Different hydrocarbon windows are shown based on the location from east to west ("Barnett Shale – Oil and Gas Field", 2013).*

### *3.2.2 Methodology*

Thirteen vertical samples were selected from the Barnett shale based on mineral composition and total organic carbon (TOC). Samples were sliced from 1-in cores for 0.25-in thickness discs and placed in specimen stubs, progressively polished to 1500 grit, and broad beam argon-ion milled.

***Fig. 3.19*** compares two nanoindentation tests; 10 seconds holding time in blue, and 600 seconds extended holding time in black. Because 10 seconds hold was insufficient to quantify the steady-state creep, hold time was extend to 600 seconds. For this test, 36 indentations were placed around the sample in four grids of 3x3.

A model presented by Dean et al. (2013) was used to obtain the parameters from the secondary creep. In ***Fig. 3.20,*** the holding time segment displays creep rate as a function of time. There is an initial rapid decrease in rate during the first seconds; however, there is a transition from

primary to secondary creep after three minutes. Note that extending the holding time from 10 to 600 seconds is supported.

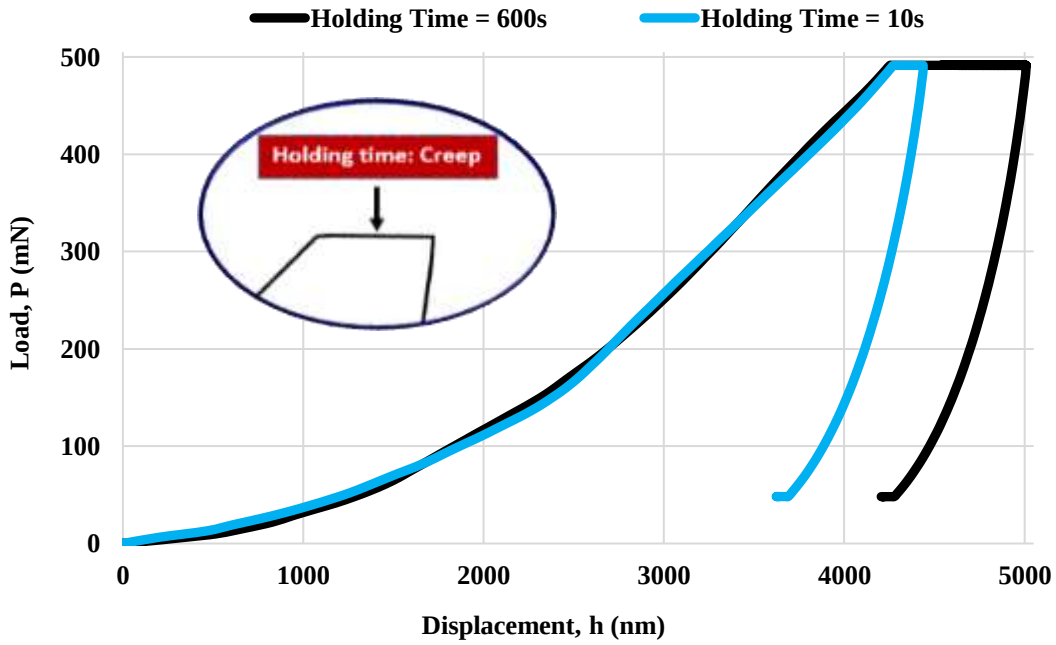


*Figure 3-19. Nanoindentation curves for standard tests with holding time of 10 seconds (blue) and creep tests with increased in holding time to 600 seconds (black). Creep is imperceptible during either hold time.*

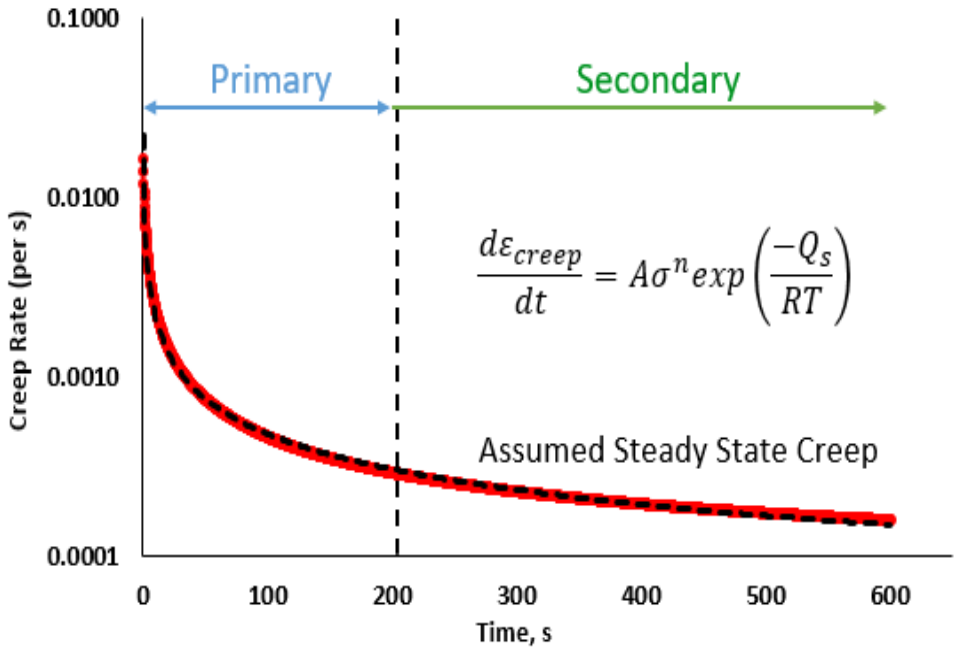


*Figure 3-20. Creep rate during the 600 seconds of holding time. Primary creep happens in the first 200 seconds, and then an assumed steady state creep is modeled.*

### *3.2.3 Petrophysics*

Petrophysical properties, mineralogy, porosity, and TOC were measured on each sample. Porosity was obtained from the core sample using a helium porosimeter. A small portion of each sample was taken and used in mineralogy and TOC measurements. Samples were crushed using a mortar and pestle, and 100 mg were measured and acidized using HCl (16 wt. %), where carbonates were removed. TOC was obtained using the LECO™ instrument. With the same crushed material, transmission Fourier Transform Infrared Spectroscopy (FTIR) was used to obtain mineralogy (Hunt et al., 1950). The rock composition was divided into four main categories. 1) Quartz, 2) Carbonates, 3) Clays, and 4) TOC, as indicated in ***Fig. 3.21***. Each mineral group has a wide composition range, where clays and quartz are the most abundant; carbonates are more visible in samples 7-13, and TOC ranges from 1 to 9 wt%.

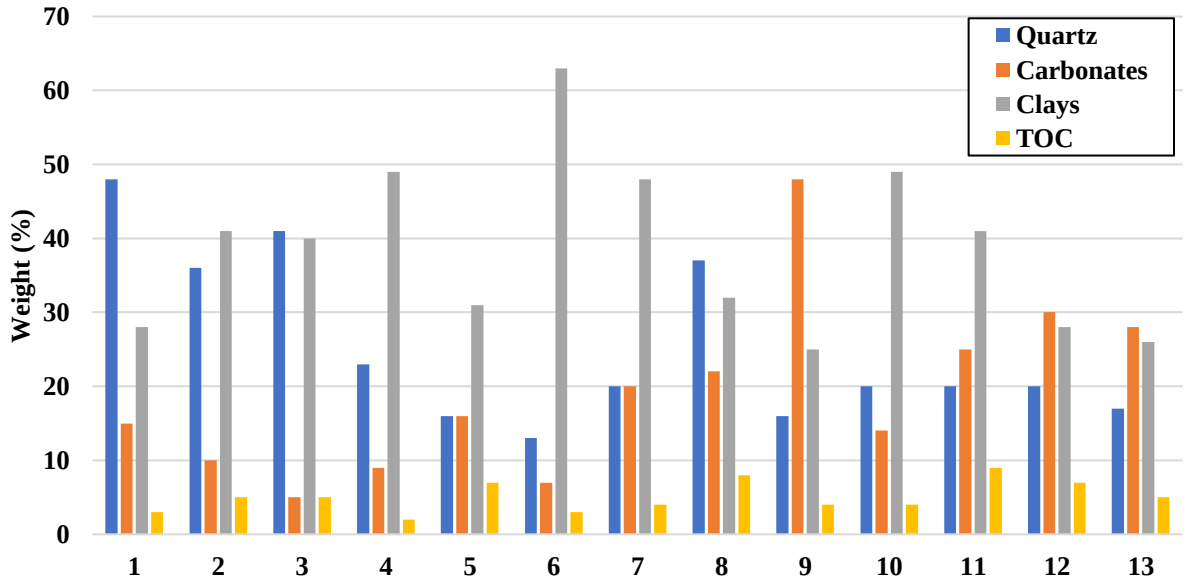


*Figure 3-21. Sample mineralogy and TOC (%) of the 13 Barnett shale samples. Four groups were separated into quartz, carbonates, clays, and TOC. Note the high variability in all the mineral groups. TOC ranged from 2-9 wt%.*

### *3.2.4 Results*

Creep displacement is the displacement measured during holding time; creep rate is the change in displacement per time step; creep strain is the creep displacement divided by the total displacement, and the stress exponent is a value used to compare stress and strain.

***Impact of sample composition***

Creep displacement directly correlated with TOC and clay content (***Fig. 3.22***). The higher the clay and TOC, the greater the plastic deformation. The point circled in red illustrated an outlier, which corresponded to a high drift coefficient during testing.

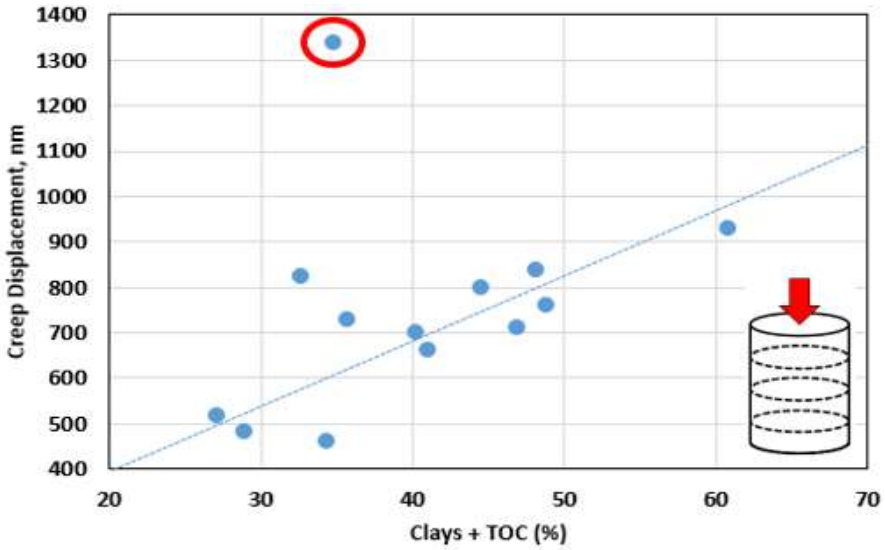


*Figure 3-22. Creep displacement vs clay + TOC (wt.%). The cylinder represents the orientation of the indentation perpendicular to the bedding planes. Higher clay and TOC percentages led to greater deformation.*

***Impact of hardness***

The measured creep displacement was compared to hardness in each sample. ***Fig. 3.23*** shows creep displacement and hardness inversely proportional; the higher the hardness, the lower the plastic deformation. Note that both parameters were acquired through different physical measurements.

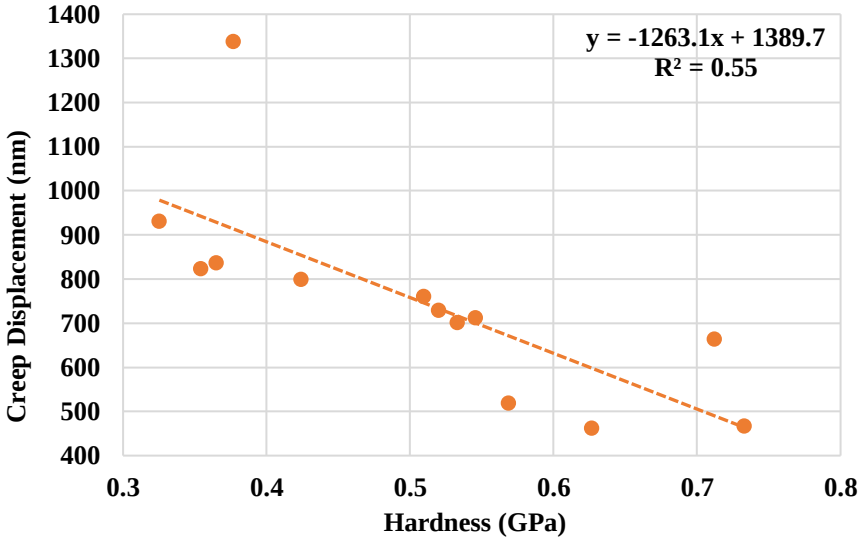


*Figure 3-23. Creep displacement versus hardness. An inversely proportional relation is observed. Note the same outlier highlighted in Fig. 3.7.*

***Stress exponent***

Using the steady-state equation from Dean et al. (2013), terms were rearranged to establish a relation between stress and strain. The values of the universal gas (R = 8.3 J/mol*K), *A* ($3.8 \times 10^{-8}$ $MPa^{-1}s^{-1}$), and temperature (T = 298 K) were all assumed constant. The equation was simplified as given by ***Eqn. 3.3***:

$$\frac{d\varepsilon_{creep}}{dt} = A\sigma^n exp\left(\frac{-Q_s}{RT}\right) \rightarrow B\sigma^n \quad \text{.....(3.3)}$$

and by taking the natural log on both sides, it follows ***Eqn. 3.4***:

$$\ln\left(\frac{d\varepsilon_{creep}}{dt}\right) = n * \ln(\sigma) + \ln(B) \quad \text{.....(3.4)}$$

***Eqn. 3.4*** displays the stress exponent, **n**, to depend only on the applied stress and creep deformation change over time. The higher the deformation change per time for the applied stress, the higher the stress exponent. ***Fig. 3.24*** shows a plot of the log of creep rate against the log of stress. The more plastic deformation, the lower the calculated stress exponent.

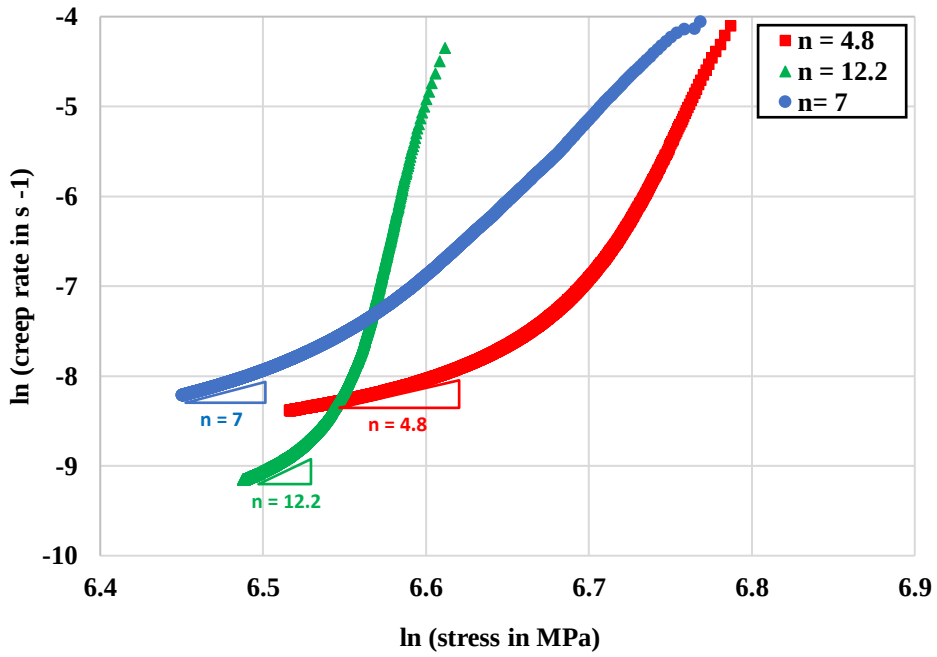


*Figure 3-24. Creep rate with respect to stress for different stress exponents. The lower the stress exponent, the faster the creep rate stabilizes and the sooner it achieves steady-state creep.*

The stress exponent averaged 7.1 for the 13 samples under dry conditions. This value is slightly higher compared to values obtained by Gupta et al. (2018), who measured an average stress exponent through the same methodology for three different formations: Eagle Ford (6.9), Woodford (6.0), and Wolfcamp (5.6), with the latter 2 overlapping within standard deviation. If compared to the other unconventional reservoirs, lower creep is expected in the Barnett, probably due to the higher quartz content.

Creep strain, the displacement during the holding time with respect to the total displacement, was compared with the stress exponent. ***Fig. 3.25*** shows a strong correlation, suggesting the creep exponent to be lower when there is low plastic deformation.

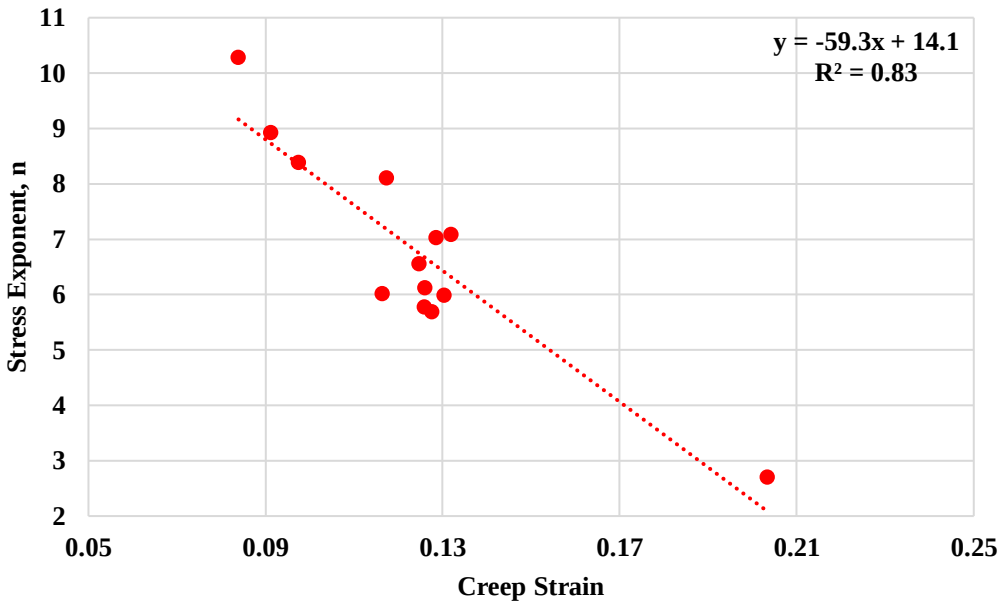


*Figure 3-25. Stress exponent compared to creep strain. Creep strain increases when the stress exponent decreases, suggesting greater plastic deformation.*

### *Creep on saturated samples*

Following the methodology used for dry samples, the stress exponent was also calculated under saturated conditions. A significant decrease was calculated from a 7.1 average on dry conditions to a 2.9 average under brine saturation. The lower stress exponent suggested more creep. The dry (red) and saturated (blue) stress exponent can be fit to one exponential decline function (see ***Fig. 3.26***).

A ratio between creep displacement under saturated to dry conditions was calculated. The saturated and dry creep ratio displacement is plotted against saturation (%) in ***Fig. 3.27***. The greater the saturation, the greater the ratio, essential that full saturation is important when running mechanical testing, as there will be a closer match to field conditions. Fluid saturation must always be considered in mechanical testing, not only with brine but also with other fluids.

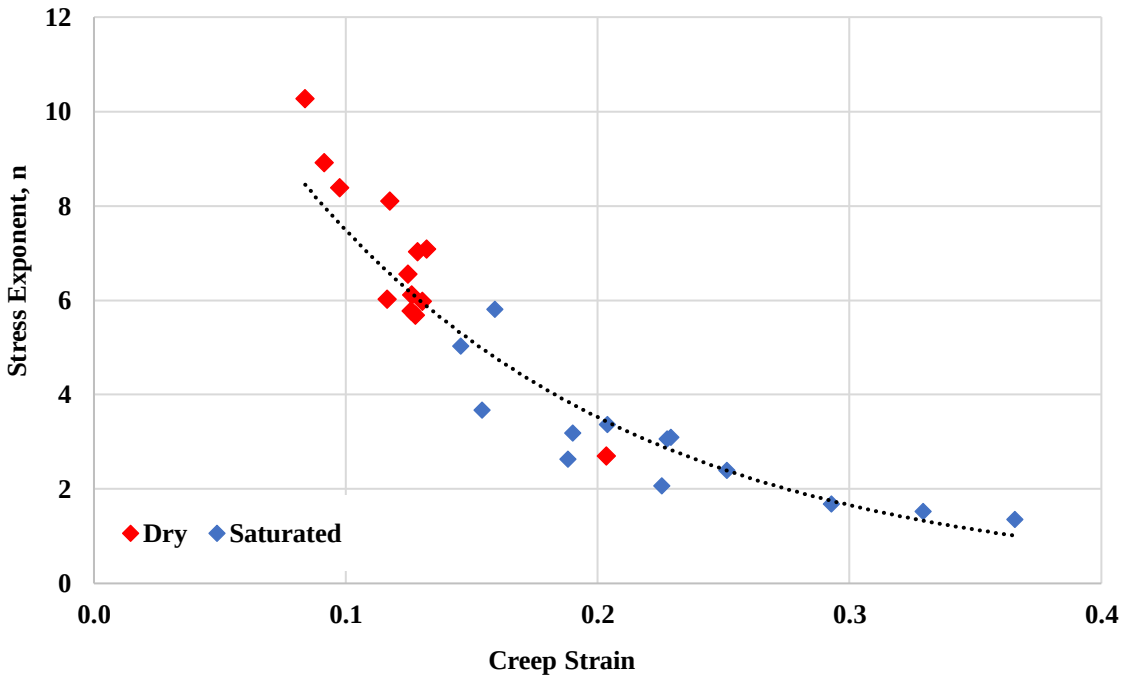


*Figure 3-26. Stress exponent as a function of creep strain for dry and saturated samples. Saturated samples follow the same trend. It also indicates higher creep under saturated conditions.*

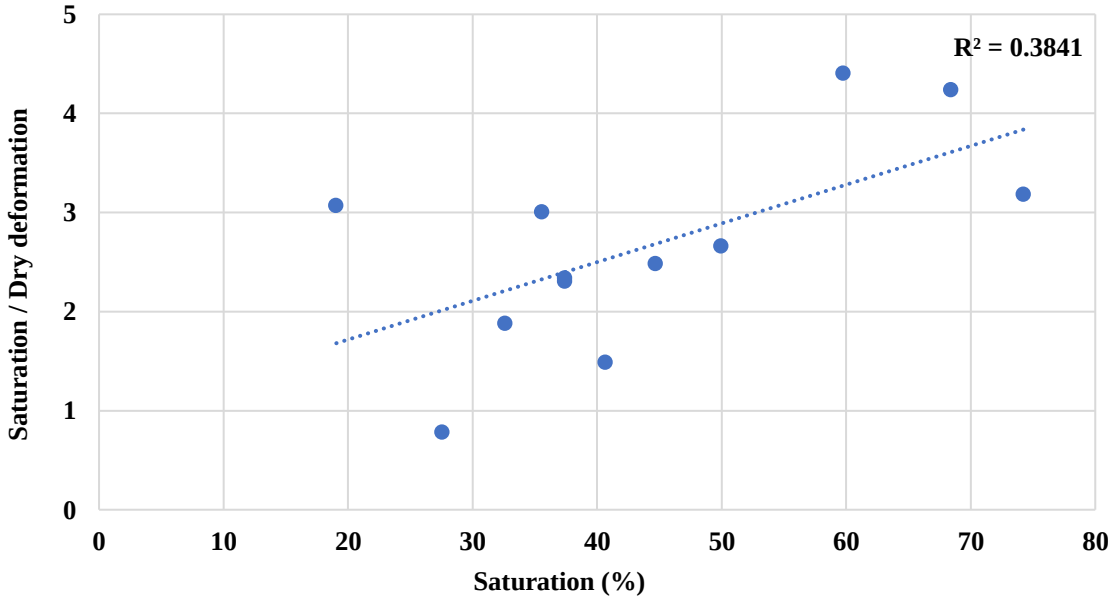


*Figure 3-27. Ratio of creep displacement from saturated to dry samples. A small correlation was observed between displacement change and the saturation (%).*

### *3.2.5 Discussion*

Wick et al. (2015) performed mechanical testing under fluid exposure. They measured the change in Young's modulus for shales under acid exposure. Gupta et al. (2018) found similar behavior after brine saturation and measured a decrease in Young's modulus and hardness. Others (Al-Bazali et al., 2013; Colback and Wiid. 1965; Lyu et al., 2018) found that compressive strength decreased with the presence of water.

The time factor must be considered to explain the behavior and change in creep displacement, as every nanoindentation test per sample took at least 5 hours. The weight difference before and after testing was small (less than 10%). Furthermore, the Young's modulus for the first and last indentations was similar, which would not have been the case if there was water loss.

Shales are clay-rich, and some of the Barnett samples reached more than 60% clay content. Clay swelling was considered as one of the main reasons for the difference in displacements (Lyu et al., 2015) showed how plasticity was directly correlated to clay percentage. Based on FTIR, illite was the primary clay, a non-swelling clay. However, some studies have observed that illite can interact with water (Aksu et al., 2015).

This study only considered one fluid. Literature showed that distinct behaviors occurred in the same material if exposed to different fluids (Wick et al., 2020). In the next chapter, I will continue to address this issue.

## 3.3 Mechanical and Microstructural Studies of Volcanic Ash Beds in Unconventional Reservoirs

The success of the 'shale revolution', which made US energy independent, strongly depends on horizontal drilling and hydraulic fracturing (HF). HF is used to increase the surface area through the creation of fractures. The greater the number and size of fractures, the greater the contacted reservoir and hydrocarbon production. Shale reservoirs are usually multi-layered, and the contrast in mechanical properties of those layers is one of the main factors determining the vertical growth of a fracture. Volcanic ash beds are thin layers commonly observed in unconventional formations (e.g., Eagle Ford and Vaca Muerta). They have a different mineral composition than the main shale reservoir, which can produce a considerable contrast in mechanical properties with respect to surrounding layers, decreasing the fracture extent and as consequence, total hydrocarbon recovery (Xu et al., 2016). Thus, quantifying the mechanical properties of ash beds becomes significant. However, it is still a challenge to subject samples to conventional testing methods because of their friability. Additionally, no previous measurements of mechanical properties of ash beds have been reported in the literature. This section reports the mechanical properties of ash beds and analyzes their contrast with the surrounding formation matrix from the Eagle Ford shale play.

### *3.3.1 Formation Evaluation*

The Eagle Ford Shale is one of the richest hydrocarbon formations in the United States. Located in south Texas, it has reserves in both oil and natural gas ("Eagle Ford Shale – Oil and Natural Gas Field", 2013). This formation is subdivided into two zones: the upper and lower Eagle Ford, lying underneath the Austin Chalk and over 11,000 ft deep and 470 ft thick. Wells are placed from southwest to northeast, as illustrated in ***Fig. 3.28,*** with different decreasing maturity windows

going from (S-N). The Lower Eagle Ford is the main production target. This zone also contains a high variability in mineralogy, having volcanic ash beds.

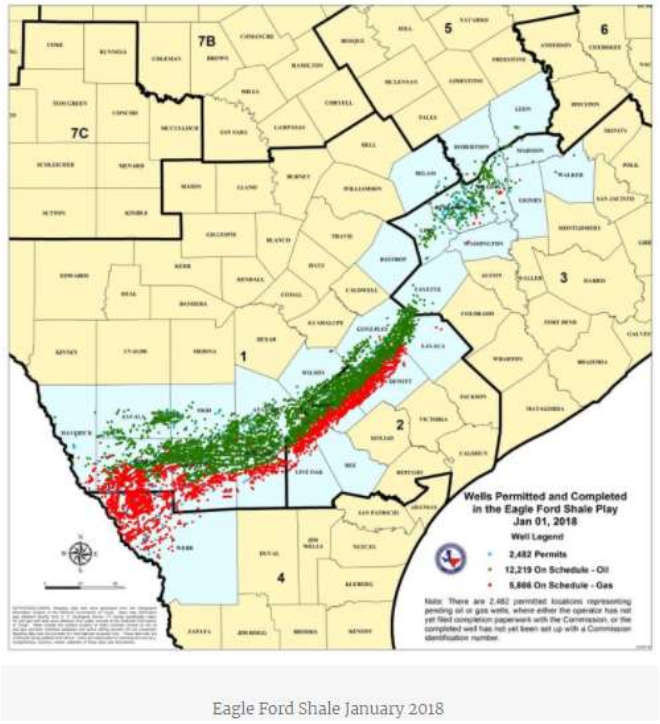


*Figure 3-28. Well placement and completion in the Eagle Ford in 2018 ("Eagle Ford News", 2019). The green and red dots illustrate the oil and gas scheduled wells. Note that the maturity increases from north to south.*

### *3.3.2 Methodology*

The 150-ft of core used in this study comes from La Salle County, Texas. Ash beds were easily identified under UV-Light. Their presence was detected from top to bottom with an average of a 5% thickness ratio. Two 1-in thick beds were selected for this study (***Fig. 3.29***). Ash bed #1 was located between clay and carbonate layers. This bed was chosen due to the high clay content (80 wt%), which clays included mica, kaolinite, illite, and smectite. Ash bed #2 showed a particularly rich composition in plagioclase and high clay content based on x-ray diffraction (XRD). This bed was adjacent to a calcite layer.

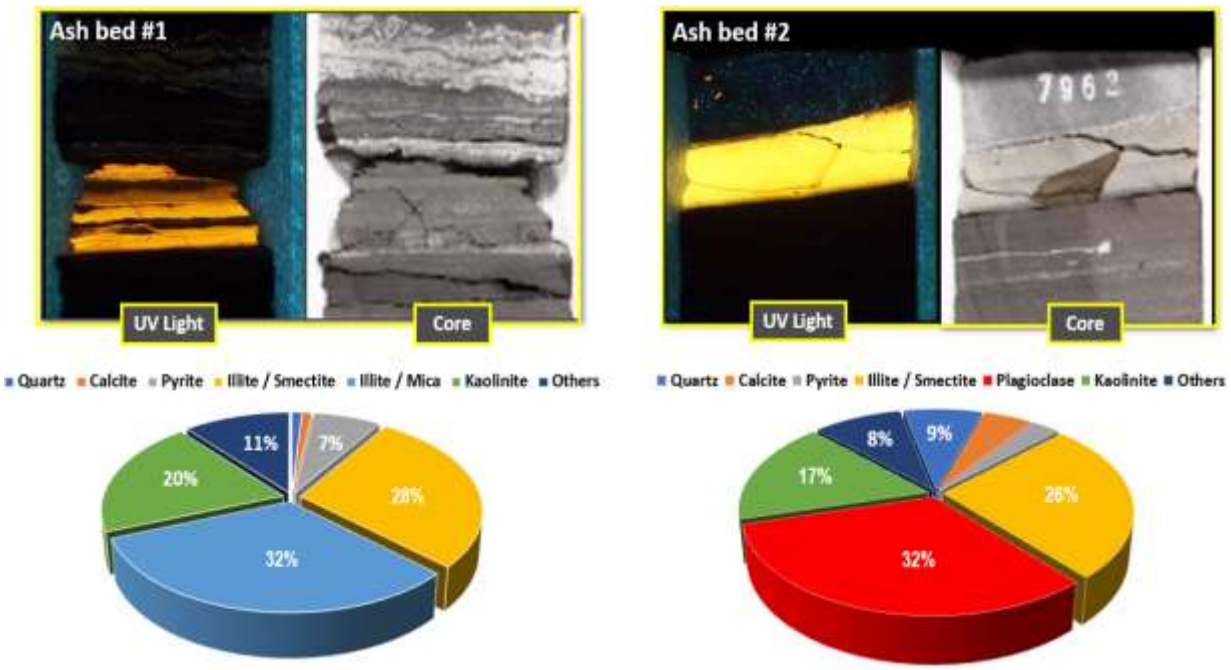


*Figure 3-29. Ash bed illustration with the correspond mineralogy. Ash bed #1 is a clay rich sample mainly composed of illite, kaolinite and smectite. Ash bed #2 is mostly composed of clays and plagioclase. Note the yellow color under UV light due to the illite composition.*

Ash beds were initially placed in aluminum discs and filled with rigid epoxy (JB-Weld). Epoxy was let to cure for 24 hours, followed by slices to obtain vertical and horizontal pieces. The surfaces were first polished with a 120-grit paper until the epoxy was removed from the surface: then, progressively dry polished to a 1200-grit. Lastly, broad beam argon-ion milling was completed.

Once the ash bed sample was prepared, mechanical testing started. The loading protocol was modified because the samples were more plastic. The maximum load was set to 49 mN, 10 times lower than the experiments on the Barnett and Wolfcamp samples. The holding time was initially set to 10 seconds, but it was extended to 400 seconds while measuring creep. A total of 100 indentations were made on each sample in multiple 5x5 grids.

### *3.3.3 Results*

The microstructural analysis includes both SEM imaging and thin-section analysis. On the other hand, mechanical properties will describe parameters such as Young's modulus, creep, and anisotropy.

***Microstructural analysis***

**Thin-section analysis** was used on both ash beds. ***Fig. 3.30*** shows optical microscopy on ultrathin sections (Courtesy: Dr. Richard Larese). Ash bed #1 shows illite and illite/smectite matrix with small calcite grains. Forams were observed in portions of the sample; these were often replaced with diagenetic kaolinite, calcite, or pyrite. In Ash bed #2, the illite and illite/smectite matrix was observed but with the presence of many plagioclase grains which underwent chemical alteration.

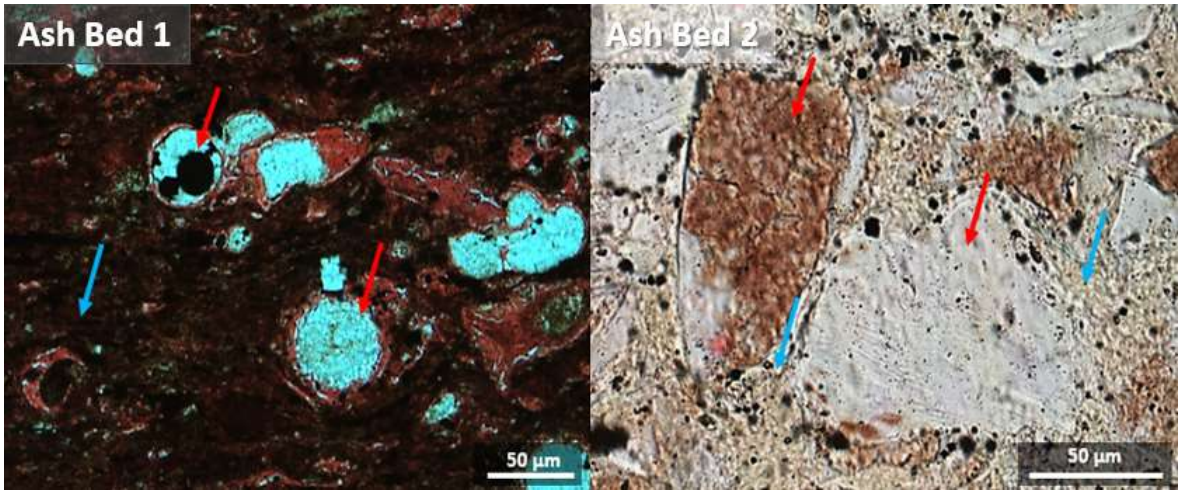


*Figure 3-30. a) Thin section image of Ash bed 1 with illite-smectite matrix and calcite grains (blue arrows), and fossil forams replaced with diagenetic kaolinite, pyrite, and calcite (Red arrows). b) Thin section of ash bed 2 which shows plagioclase grains with diagenetic alterations (red arrows). Blue arrows show a clay matrix of mainly illite and smectite.*

**Scanning electron microscope** describes surface observations through backscattered electron imaging. ***Fig. 3.31*** illustrates Ash bed #1. Note that the right image is at a higher magnification. This bed had illite and kaolinite as the main components, the lighter and darker

regions in the right images, with some pyrite (bright) present. Pyrite seemed to be a replacement mineral in fossils, as noted in the left image of ***Fig. 3.31***. Most of the porosity occurred in illite, smectite, and mica zones. Kaolinite had very low porosity.

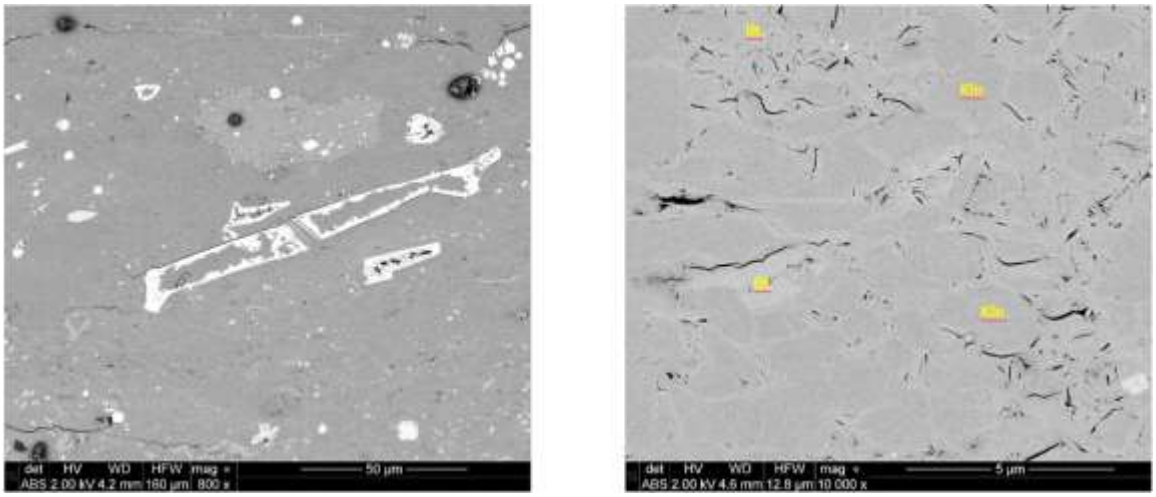

*Figure 3-31. Ash bed #1. Illite and kaolinite are the main components on the sample surface, which also has a pyrite (brightest objects) presence. Porosity is observed in the illite. Courtesy: Dr Mark Curtis.*

Ash bed #2 showed a highly heterogeneous matrix (***Fig. 3.32***). Minerals such as quartz, calcite, pyrite, and plagioclase are present, but illite and kaolinite dominate clay components, while plagioclase is the main non-clay mineral. Note the porosity difference in two adjacent kaolinite minerals, partially due to diagenesis.

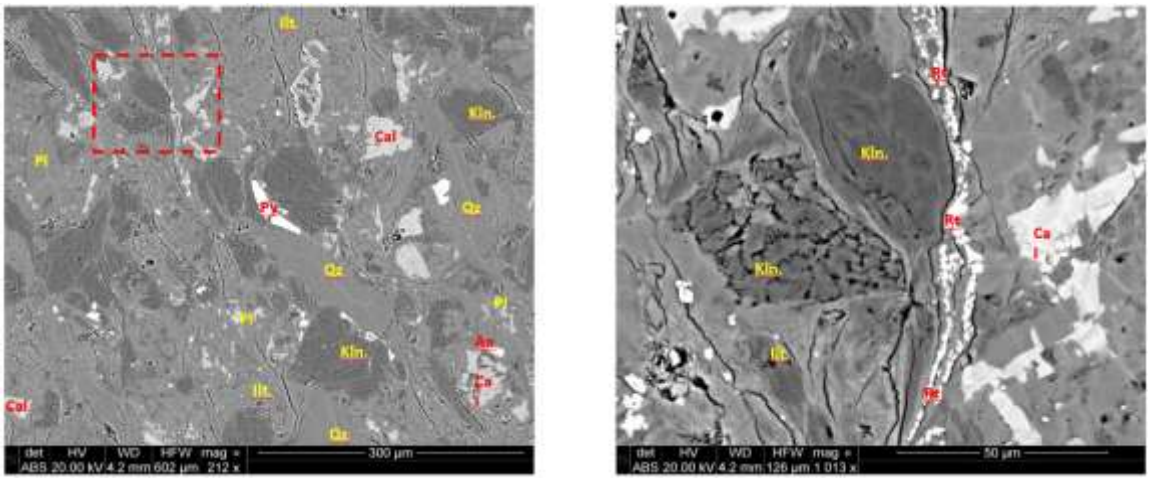

*Figure 3-32. Ash bed #2. Heterogeneous matrix is observed with clays, calcite, and plagioclase. Note the two kaolinite grains; one of them is porous and the other is not. Courtesy: Dr Mark Curtis.*

### *Mechanical Properties*

Young's modulus was initially measured on each bed (***Fig. 3.33***). Ash bed #1 moduli ranged from 12 to 24 GPa, with an average near 17 GPa. This ash bed has fairly homogeneous mineralogy mainly composed of clays (80%). On the other hand, Ash bed #2 had a higher standard deviation in Young's modulus, ranging from 7 to 47 GPa, with a mean of 25 GPa. This higher modulus was attributed to the plagioclase and quartz content, corresponding to 40% of the total composition.

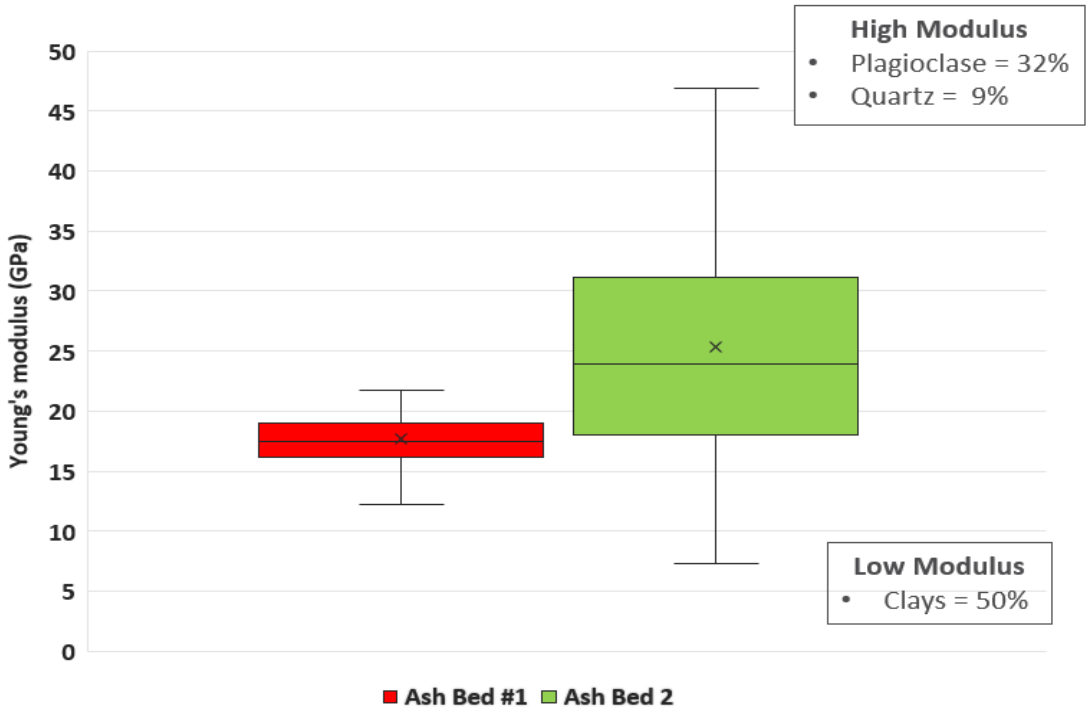


*Figure 3-33. Young's modulus for both Ash bed #1 and #2. There is a small standard deviation in ash bed #1 as it is mainly composed of clays. Ash bed #2 has a higher standard deviation due to mineralogic heterogeneity.*

***Fig. 3.34*** shows slightly greater horizontal moduli than the vertical value for Ash Bed #1; however, their standard deviations overlapped. The range in Young's modulus oscillated between 12 to 24 GPa. This showed little to no anisotropy within the ash beds.

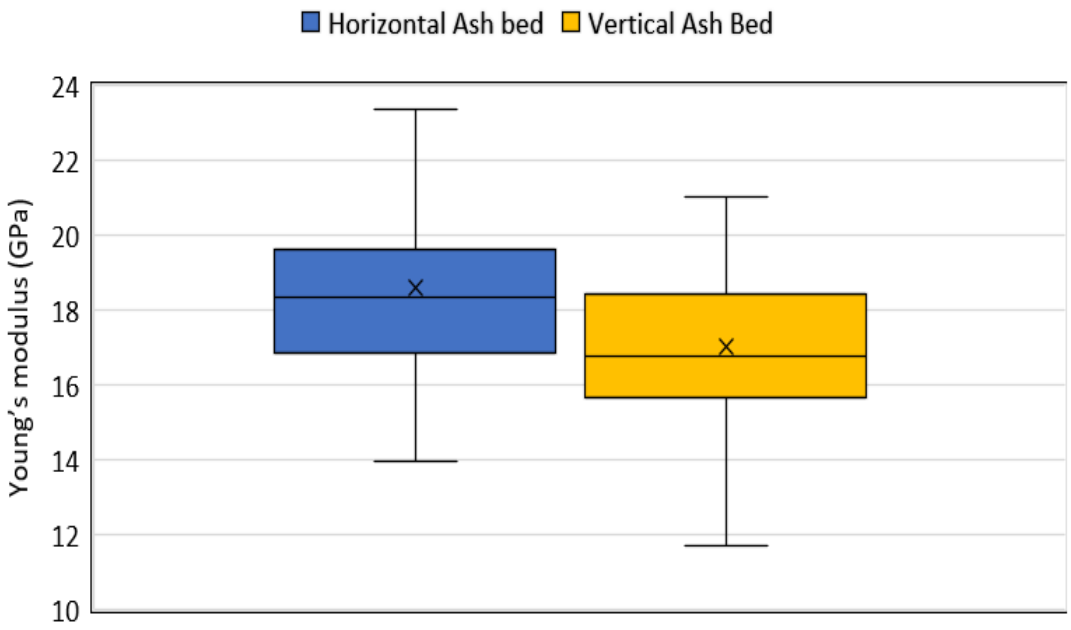


*Figure 3-34. Anisotropy within an ash bed. Horizontal direction in Ash bed #1 has a slightly higher Young's modulus than the vertical, but they overlap within the standard deviation. The average is around 17 GPa. The degree of anisotropy is small.*

A comparison in elastic properties was performed between the ash bed and the adjacent layers to determine the contrast in elastic parameters. ***Fig. 3.35*** shows core images with their respective mineralogy on the left. A calcite bed and two mixed layers of carbonate and clay content were adjacent to the ash bed. The calcite bed had a higher modulus with an average of 68 GPa, similar to the standard value of pure calcite. The mixed layer had a high standard deviation in Young's modulus, ranging from 25 to 85 GPa and a 45 GPa average. The large range was due to the extreme mineralogic composition of clays and carbonates. The ash bed #1 had the lowest Young's modulus (17 GPa average), with significant contrast. A 1:2 ratio of Young's modulus was observed with the mix zones, while a 1:4 ratio was observed with the calcite bed. This contrast was significant but is not noticed in logging tools, and it is significantly high over such small distances, which can have a tremendous impact on fracture propagation.

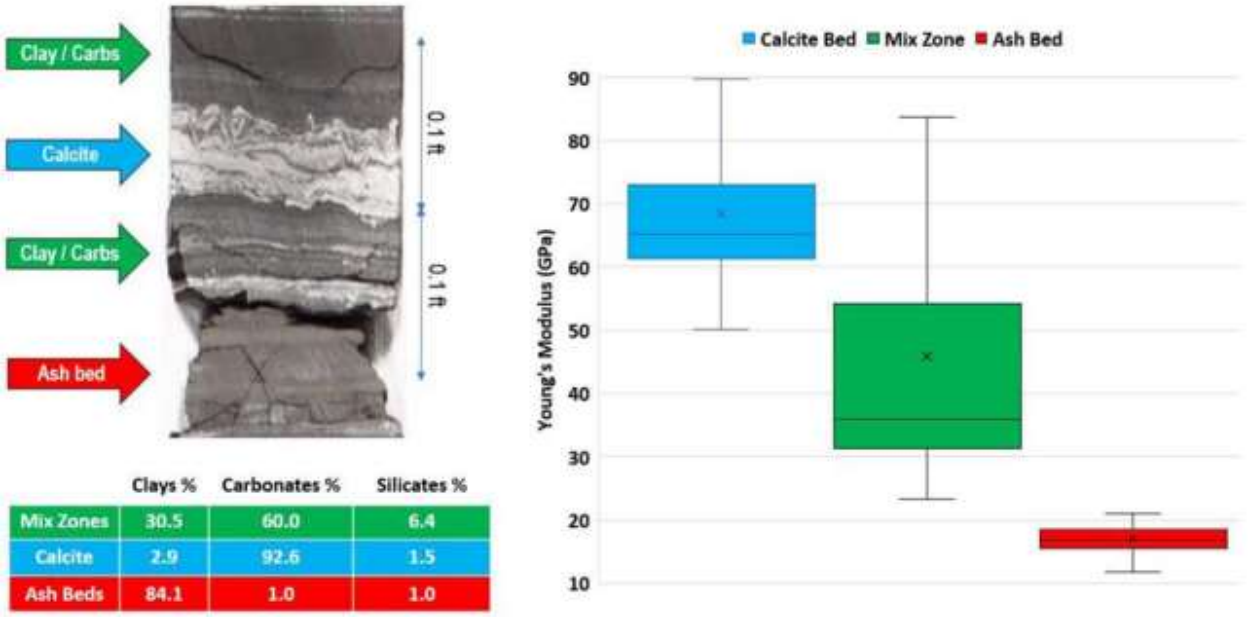


| | Clays % | Carbonates % | Silicates % |
|---|---|---|---|
| Mix Zones | 30.5 | 60.0 | 6.4 |
| Calcite | 2.9 | 92.6 | 1.5 |
| Ash Beds | 84.1 | 1.0 | 1.0 |

*Figure 3-35. Ash bed #1 and adjacent layers with their compositions (wt.%). The boxplot (right) shows a significant contrast between the ash bed Young's modulus and the remaining layers.*

Creep properties were also measured. Instead of using the standard 10 second holding time, 400 seconds were used to capture secondary creep parameters. ***Fig. 3.36*** shows the indenter tip displacement as a function of time. Each curve shows the average displacement with the solid line and the standard deviation. A steadier, almost linear deformation rate follows a rapid deformation during the first seconds. During this steady time, ash beds deformed at a rate of nearly 0.9 nm/s, three times higher than the rate in the mixed and calcite zone. This is critical as proppant embedment can be a significant issue in ash bed rich zones.

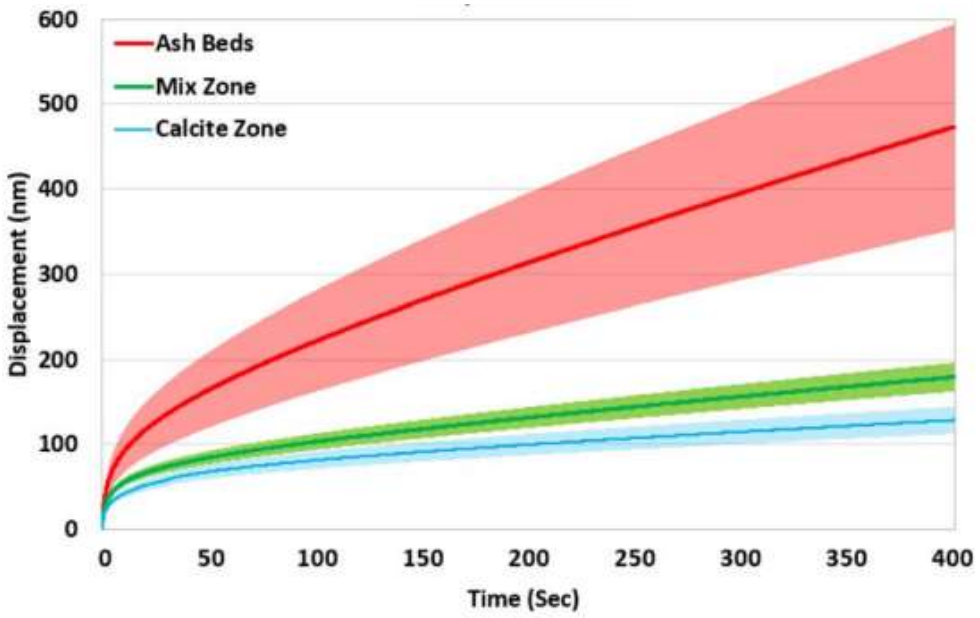


*Figure 3-36. Displacement as a function of time for the 400 seconds holding time. Ash beds have the highest plastic deformation, being nearly three times greater than the mix zone and the calcite bed.*

After determining little to no anisotropy in the ash beds and calculating such high contrast in elastic parameters between the ash beds and the Eagle Ford matrix, the impact of ash beds in the formation anisotropy was calculated. The Backus Averaging technique was used to determine anisotropy for potential ash bed thicknesses (Kumar et al., 2013). The same three layers used in this study were assumed to be the dominant layers in the Eagle Ford with the corresponding properties as shown in ***Table 3.2***.

*Table 3-2. Input properties for calculating the Backus average. The description on each property was acquired is explained in this section.*

| | Carbonates (wt. %) | Clays (wt. %) | Others (wt. %) | $V_S$ (m/s) | $V_P$ (m/s) | Density (kg/m$^3$) |
|---|---|---|---|---|---|---|
| Calcite Bed | 90 | 5 | 5 | 2930 | 6000 | 2735 |
| Mix Zone | 60 | 30 | 10 | 2260 | 3700 | 2780 |
| Ash Beds | 5 | 85 | 10 | 1850 | 2600 | 2685 |

The elastic stiffness matrix was calculated using the formulas below, *where ρ is the bulk density, while ε, γ, and δ are the Thomsen parameters.*

- $C_{33} = V_p^2 * \rho$
- $C_{44} = C_{55} = V_S^2 * \ \rho$
- $C_{11} = (1 + 2\varepsilon) * C_{33}$
- $C_{66} = (1 + 2\gamma) * C_{44}$
- $C_{13} = \sqrt{2\delta C_{33}(C_{33} - C_{55}) + (C_{33} - C_{55})^2} - C_{55}$

Input parameters are required:

- ***The bulk density (ρ)*** was obtained using the X-Ray Fluorescence (XRF) mineralogy (***Fig. 3.37***). Based on the mineral composition, the density was calculated.

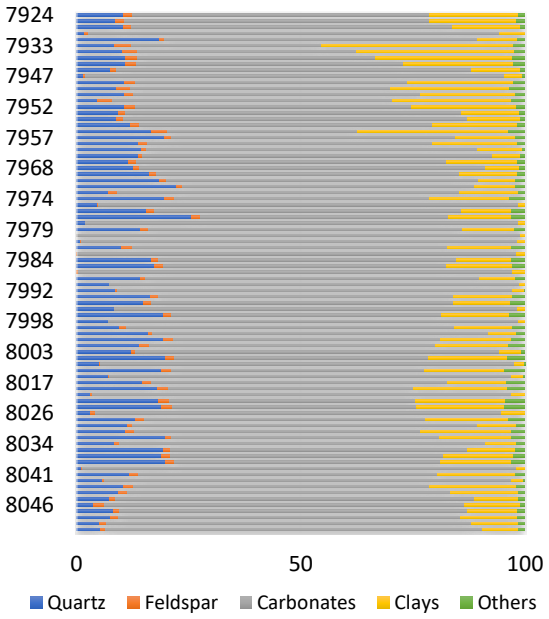


*Figure 3-37. Well mineralogy measured with the XRF. Note that carbonates are the main components with clays and quartz as the secondary minerals. Ash beds are not observed due to the low XRF resolution.*

- ***The shear velocity*** was obtained from a shear modulus using an empirical relation established for the late time loading of the nanoindentation data (Gupta et al., 2018). As shown in ***Fig. 3.38***, the shear modulus and bulk density were used to obtain the shear velocity with ***Eqn. 3.5***.

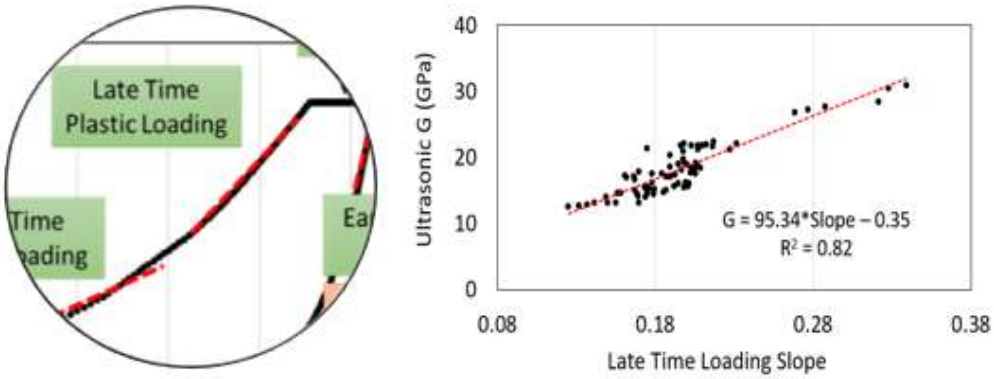


*Figure 3-38. Empirical correlation between the ultrasonic velocity and late time loading slope in nanoindentation (Gupta et al.,2018).*

$$\mu_d = \rho V_s^{\,2} \quad \text{.....(3.5)}$$

- ***Thickness ratio*** was measured over the 150-ft core length. The ratio of the ash bed thickness with respect to the total thickness was calculated.
- The ***P-wave*** velocity was calculated using a combination of two formulas. The Poisson's ratio (ν) was obtained using ***Eqn. 3.6***:

  $$E_d = 2\rho V_s^{\,2}(1-\nu) \quad \text{.....(3.6)}$$

  Then, ***Eqn. 3.7*** was used to solve for the p-wave velocity:

  $$\nu = \frac{0.5*\left(\frac{V_p}{V_s}\right)^2 - 1}{\left(\frac{V_p}{V_s}\right) - 1} \quad \text{.....(3.7)}$$

The Thomsen parameters were calculated as followed:

- $\varepsilon = \frac{C_{11} - C_{33}}{2C_{33}}$
- $\gamma = \frac{C_{66} - C_{44}}{2C_{44}}$
- $\delta = \frac{(C_{13} + C_{55})^2 - (C_{33} - C_{55})^2}{2C_{33}*(C_{33} - C_{55})}$

Based on the XRF mineralogy, a starter composition was assumed, with 25% calcite and 75% mixed zones. The presence of each zone was gradually decreased by 1% and compensated with an increase in 2% of ash beds until reaching a 10% ash bed thickness. ***Fig. 3.39*** shows that

increasing ash bed thickness increases the overall anisotropy; nevertheless, the parameters were small. This suggested that ash beds do not make the Eagle Ford significantly anisotropic, and their detection with seismic will be difficult.

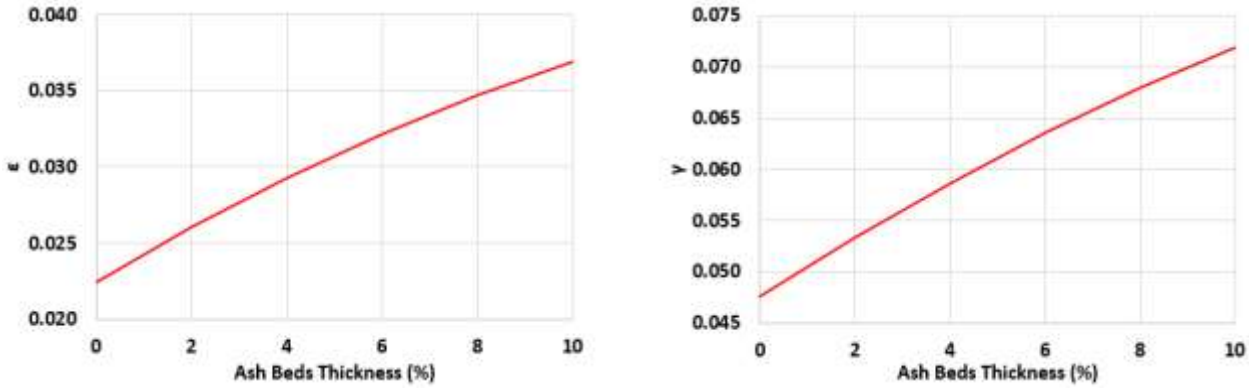


*Figure 3-39. Thomsen parameters as a function of ash bed thickness. The anisotropy increases as the ash bed thickness increases. Calculations based on Backus averaging ash bed thicknesses and properties.*

### *3.3.4 Discussion*

Nanoindentation has been successfully applied to measure Young's modulus and creep in ash beds. Young's modulus for the ash beds ranged between 12 to 24 GPa with an average of 18 GPa, giving rise to a large mechanical property contrast between the formation matrix and these beds. Young's modulus was up to five times smaller in ash beds compared to neighboring layers. The ash beds also displayed more creep than other layers, leading to issues such as proppant embedment and fracture closure. Based on the Backus averaging, the presence of ash beds does not make the Eagle Ford formation significantly anisotropic; note that the core used in this study, came from La Salle County, which is one of the lowest in cumulative bentonite thickness (Antía et al., 2013). Fig. 3.40 shows that zones towards the northwest are richer in ash beds, with cumulative thickness up to 7.0 ft. Well placement needs special consideration in those zones.

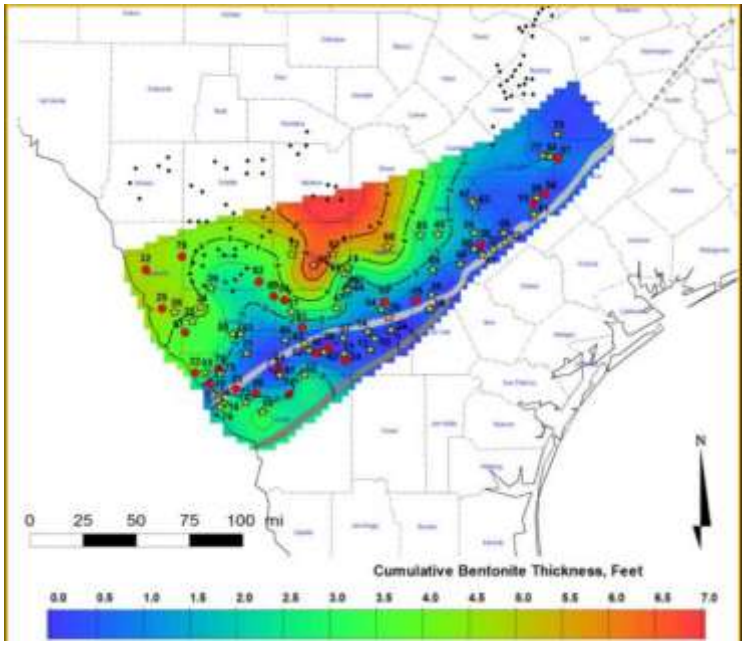


*Figure 3-40. Bentonite characterization and distribution in the Eagle Ford (Antía et al., 2013).*

There was high variability in the ash beds mineralogy. Illite and kaolinite were the primary clays, plagioclase and calcite were also common components depending on the ash bed type, and porosity was highly variable and largely depended on the presence of clays and smaller calcite grains.

# 4. HYDRAULIC FRACTURING

Hydraulic fracturing has become a main stimulation technique in exploiting unconventional resources. Acids are pumped downhole to clear the pathway for fluid flow, and fracturing fluid is injected, raising the pressure to exceed the fracture pressure. The fractures open from the wellbore in the direction of least resistance and propagate perpendicular to it. Proppant (sand) is injected at this stage to hold the fractures open, and hydrocarbons are extracted. Lastly, fracture closure occurs due to in-situ rock stresses after injection stops and continues during hydrocarbon withdrawal. Parameters such as fracture length and width are measures of effectiveness; the greater the contacted area, the greater the recovery. Changes in hydraulic fracturing protocol design are required to increase recovery; fluid viscosity, fluid flow rates, injection pressures, and proppant sizes are commonly evaluating factors. Acoustic waves and emissions (microseisms) are used to determine the stimulated reservoir volume. Acoustic emissions are known as microseismics in the field. They refer to the energy generated by a crack during fracturing. These emissions contain important information related to fracture mechanics (location, magnitude, frequency, mechanism, orientation) and are a determinant factor in deciding the success of a job.

In this section, the steps considered for data acquisition and processing during hydraulic fracturing will be explained. Next, two main hydraulic fracturing studies are considered. First, three different laboratory hydrofracturing protocols were studied using acoustic emissions. This study considers a constant injection rate test, a pre-cyclic injection test, and a variable rate injection test under dry conditions. Based on the results of the first study, pre-cyclic injection is further analyzed by changing the number of cycles used before breakdown, aiming to determine an optimal number of cycles. This latter test was achieved under brine-saturated conditions.

## 4.1 Experimental Procedure

### *4.1.1 Sample preparation*

A) Tennessee sandstone cuboids of 12” x 12” x 6” are cut into four smaller blocks. Then, 4” diameter – 6” length samples are cored in the vertical direction and polished using a surface grinder. Samples are dried for 48 hours in the oven at 100°C.

B) Circumferential velocity analysis (CVA) is performed to determine the velocity anisotropy of each sample. ***Fig. 4.1*** shows the CVA set-up elements, including the computer, signal generator, oscilloscope, and amplifiers. An acoustic wave is sent across the sample using the signal generator, and the travel time is recorded on the oscilloscope. The travel time is measured across the cylinder every 10°, using a motor to rotate the sample. A curve of P-wave velocity as a function of the azimuth is generated.


*Figure 4-1. Circumferential Velocity Analysis (CVA) set-up. It includes A) the motor that rotates the base, B) The oscilloscope which digitizes the acoustic wave, C) the signal generator which sends the pulse to the excitation transducer, D) Amplifiers, E) Computer.*

C) Wellbore preparation starts by drilling a 0.25” OD hole in the center of the sample, with a length equal to the core half-length plus 0.2”. Then, a 0.25” OD steel tubing with two slit

holes 180° apart on the bottom end is inserted and epoxied (***Fig. 4.2***). The sample is set to cure for 24 hours.

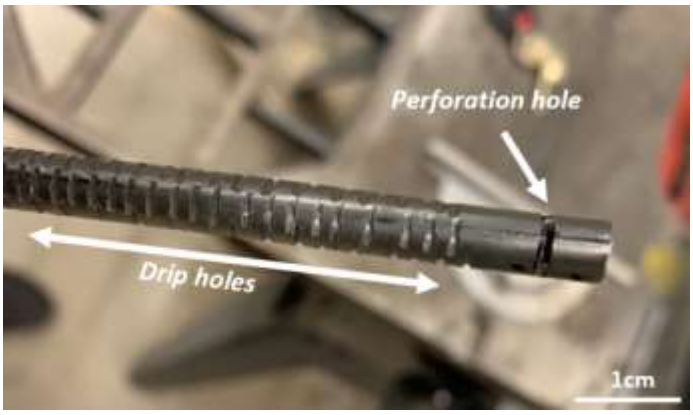


*Figure 4-2. Wellbore tubing. Note the drips which allow the epoxy to settle once the tubing is inserted at the hole. There are two holes 0.2" away from the bottom of the tubing which act as perforation holes in the tubing. There are no perforation holes in the sample.*

D) A copper jacket (0.01" thick) is placed around the sample to avoid confining fluid penetration. First, natural honey is spread on the outer surface of the sample, and then the jacket is placed and tied with rubber bands. At the jacket end, a strip of JB Weld epoxy is placed to secure the jacket and seam soldered. Then, the sample is dried for 24 hours. Vertical lines are drawn in the outer jacket from top to bottom with 45° spacing for transducer placement.

E) The sample is weighted at dry conditions, and a brine solution (2.5% KCl) is prepared with deionized water. The cylindrical sample is placed in a pressure vessel and pressurized to 5000 psi for 48 hours. Post-saturation, the sample is extracted, cleaned, and re-weighted.

F) Two endcaps are placed at the top and bottom of the sample, secured with heat-shrinkable rubber and JB weld epoxy. The rubber boot is shrunk using the heat gun. Metal wires are cut to twice the circumference length, wrapped around the rubber, and tightened at both ends. Clamps are also used to firmly secure the rubber boot (***Fig. 4.3a***).

*Figure 4-3. a) Sample with acoustic sensors. The flatjacks are placed on each side to apply the maximum horizontal stress. b) Hydraulic confining chamber. The chamber is lowered before starting the test.*

G) Lastly, fourteen 500 kHz piezoelectric crystals mounted on conformal brass stubs are and are placed in their corresponding locations, as illustrated in ***Fig. 4.4***. Note that the x and y coordinates correspond to the transducer position (top view), while the z coordinate is the depth with respect to the top (tubing end). The sixteen acoustic sensors are connected to Panametrics – NDT$^{TM}$ model 5660B wide band preamplifiers at 40 dB, that capture the signal in an FM-1$^{TM}$ low-frequency unit manufactured by Digital Wave Corp, and send it to the monitor.

| Sensor | Sensor coordinates meters | | |
|---|---|---|---|
| | X | Y | Z |
| 1 | -50.80 | 0.00 | 50 |
| 2 | -50.80 | 0.00 | 100 |
| 3 | -35.92 | -35.92 | 25 |
| 4 | -35.92 | -35.92 | 75 |
| 5 | -35.92 | 35.92 | 25 |
| 6 | -35.92 | 35.92 | 75 |
| 7 | 35.93 | 35.93 | 25 |
| 8 | 35.93 | 35.92 | 75 |
| 9 | 50.80 | 0.00 | 25 |
| 10 | 50.80 | 0.00 | 50 |
| 11 | 50.80 | 0.00 | 75 |
| 12 | 50.80 | 0.00 | 100 |
| 13 | 35.92 | -35.93 | 25 |
| 14 | 35.92 | -35.93 | 75 |
| 15 | 0.00 | 32.50 | 0 |
| 16 | 0.00 | -32.50 | 142 |

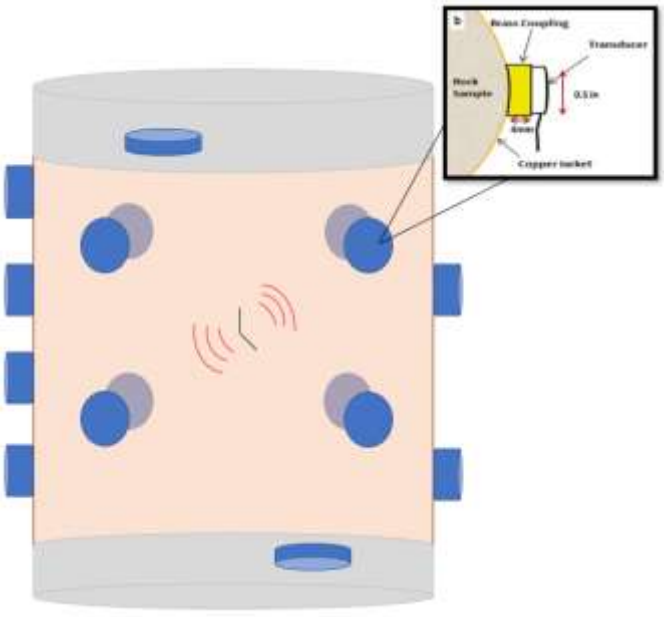

*Figure 4-4. Acoustic sensors position. There are 16 transducers, two of which are placed at the top and bottom, while the remaining 14 are placed on the exterior of the copper jacket.*

### *4.1.2 Running protocol*

The sample is placed in a closed chamber (***Fig. 4.3b***). Hydraulic fracturing experiments start by setting the stresses to the desired magnitudes. One vertical stress and two horizontal stresses are applied.

***Fig. 4.5*** shows the applied stress orientations. The vertical stress is applied using an internal piston ($\sigma_v$ = 1500 psi). Mineral oil is the confining pressure fluid and represents the minimum horizontal stress ($\sigma_h$ = 500 psi). The maximum horizontal stress is set by pressurizing a pair of flatjacks ($\sigma_H$ = 3000 psi).

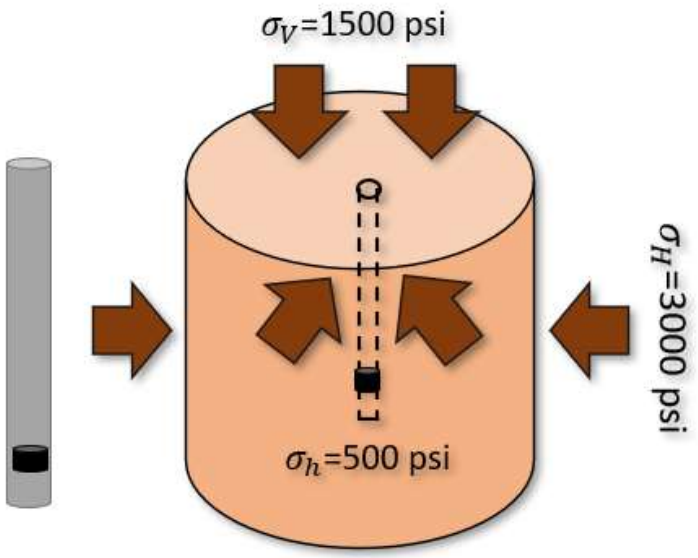


*Figure 4-5. Applied stresses ($\sigma_V$=1500 psi, $\sigma_H$=3000 psi, $\sigma_h$=500 psi).*

A Teledyne Isco pump with a capacity of 102.93 mL was used to inject the fracturing fluid. Once all the stresses are adjusted, fluid is pumped into the wellbore, building up the injection pressure until breakdown. The fracture propagates away from the wellbore in the direction of the maximum horizontal stress. When the pump is shut off, the fracture closes. Simultaneously, acoustic emissions are recorded, and pressure versus time and events versus time are plotted.

### *4.1.3 Post experimental analysis*

Permeability measurements, Scanning Electron Microscopy, and Computerized Tomography (CT) scanning were performed post-fracture. Those studies compare each protocol's effectiveness and provide insights with respect to fracture dimensionality and damage.

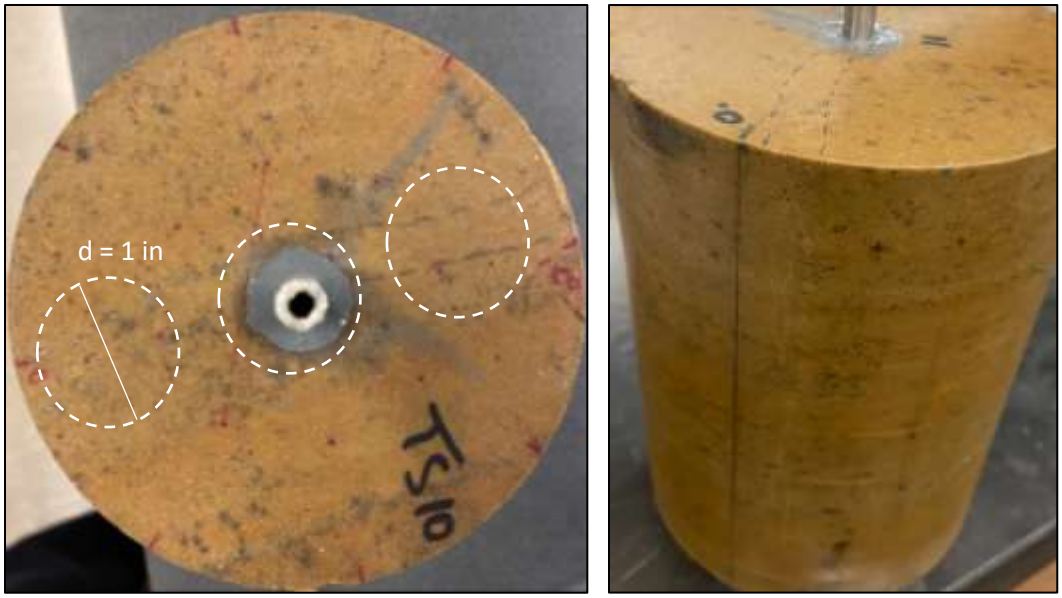


*Figure 4-6. Extracted core plug locations after fracturing. The two side cores were used for permeability and SEM Imaging, while the middle plug was used for CT-Scanning.*

After failure, two fractured wings are induced. Generally, one of them would be greater in length than the other. A 1" diameter by 4" long core is extracted at the center and at each wing (***Fig. 4.6***). Permeability tests are carried out with an AP-608, which uses a pulse decay technique as described by Jones (1971). For SEM imaging, a similar procedure was followed in core preparation; Soxhlet extraction is used for core cleaning and broad beam argon ion milling after polishing with 1200 grit. SEM images capture other parameters such as fracture width and connectivity.

### *4.1.4 Data analysis*

*a) Signal processing*

Each signal is sampled at a rate of 5MHz and consists of 1024 data points at a time step of 0.2 µs, for a total recorded time of 204.6 µs. Signal attributes were extracted from the time domain signal displayed in ***Fig. 4.7***. The ***arrival time*** is the time at which the acoustic wave is first detected. The ***signal polarity*** is either positive or negative based on the direction of the first deflection. The ***peak envelope*** is extracted by calculating the maximum absolute of the envelope during the first

10μs after arrival. The envelope function in MATLAB was used to return the upper envelope of the input sequence (wave), as the magnitude of its analytic signal. The analytic signal is found through the discrete Fourier transform. The ***signal-to-noise ratio*** is calculated as a ratio of the signal peak (after arrival time) with respect to the absolute noise peak (before arrival time).

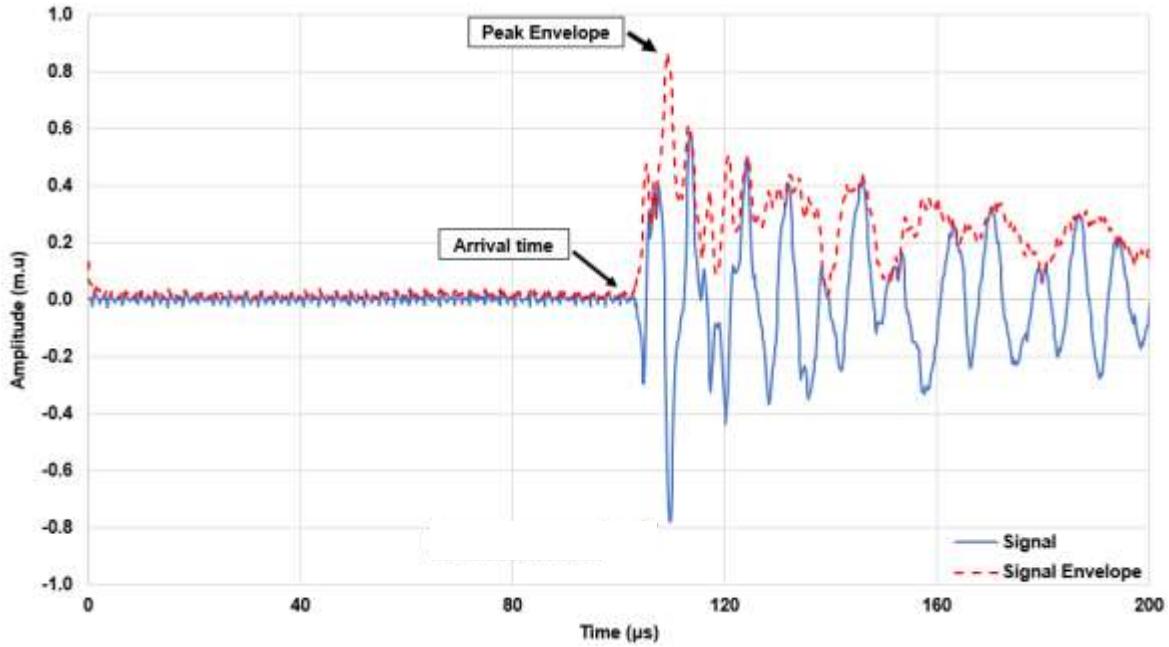


*Figure 4-7. Acoustic emission waveform for an individual event recorded by one acoustic receiver (transducer). The arrival time and peak amplitude are some of the parameters acquired.*

Signal-to-noise metrics are used to eliminate noisy events. Arrival times are used to calculate the event hypocentral. Polarities are used for focal mechanisms and seismic moment calculations.

*b) Acoustic Emission Location*

Using an algorithm developed by Ortiz (2010) and further improved by Moreno (2011), acoustic emissions are mapped based on the P-wave arrival time and the P-wave velocity. The sensor locations are known, and assuming a constant isotropic velocity and obtaining at least four clean first arrivals from 4 transducers, a system of equations (4) can be solved (***Eqn. 4.1***). The unknowns are the three event coordinates ($x_s$, $y_s$, and $z_s$) and the acoustic event origin time ($t_o$).

The arrival times ($t_i$) are recorded at the transducer locations ($x_i$, $y_i$, and $z_i$) complete calculations can be found in Moreno (2011). Note that even though only four transducers are required for calculating the hypocenter, an event is accepted if it has at least 6 good quality first arrivals.

$$t_i = t_o + \frac{\sqrt{(x_i - x_s)^2 + (y_i - y_s)^2 + (z_i - z_s)^2}}{v} \quad \text{.....(4.1)}$$

*c) Frequency Analysis*

A Fast Fourier Transform (FFT) is performed on the time signal to convert it from the time domain into the frequency domain. However, having 16 transducers means having 16 frequency spectra for each event. Thus, the received signals are sequentially stacked, and the Fourier transform is performed over the new composite waveform (***Fig. 4.8***). The frequency resolution is calculated using ***Eqn. 4.2***, with a time step (Δt) of 0.2 μs, and 1024 data points recorded (N).

$$\Delta F = \frac{1}{\Delta t * N} \quad \text{.....(4.2)}$$

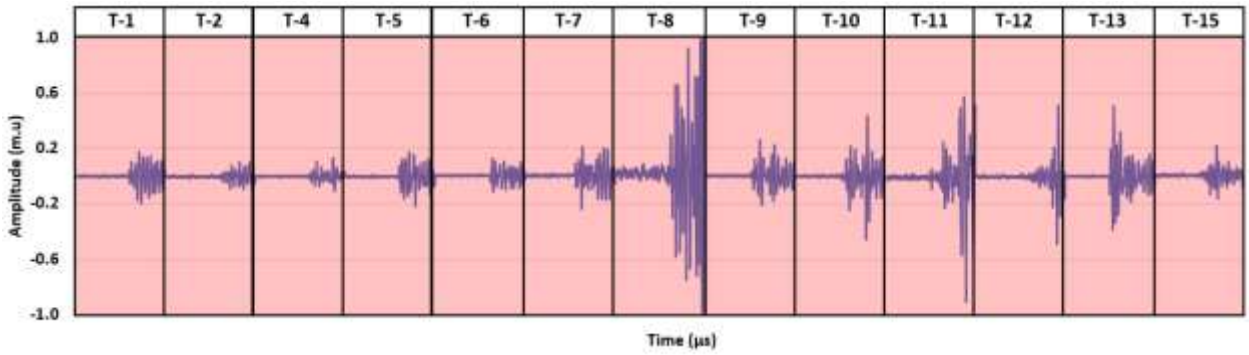


*Figure 4-8. Acoustic emissions stacking for one event. In this event, thirteen transducer signals were received and stacked sequentially.*

The spectral peak is observed from 20 to 600 kHz, with the main peak being from 90 kHz to 200 kHz (***Fig. 4.9***). This range is selected as the study interval. Two methodologies are carried out to calculate a dominant frequency: an absolute peak frequency and a mean frequency.

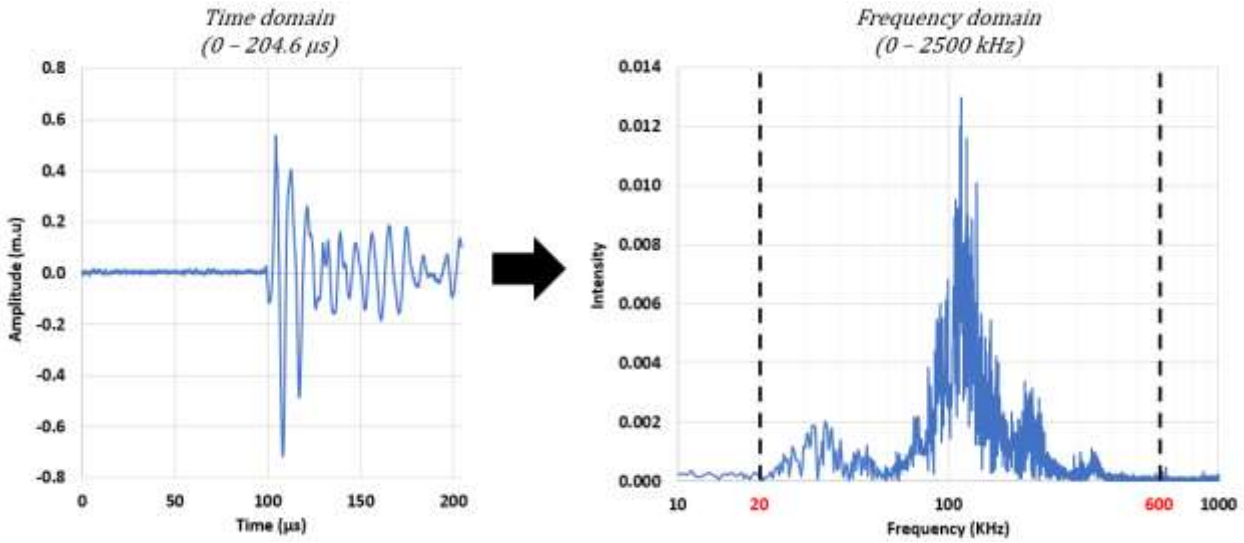


*Figure 4-9. Signal transformation for one event. In most of the events, the frequency signal decays after 400 kHz, so this signal bandwidth is set between 20 to 600 kHz for our analyses.*

The absolute peak frequency is calculated by obtaining the point at which the frequency shows the highest amplitude. On the other hand, to calculate the mean frequency, I used ***Eqns. 4.3 and 4.4***, where $Y_i$ is the amplitude for each frequency, and $X_i$ is the corresponding frequency.

$$Y_{Norm} = \frac{Yi}{\sum_1^n Y_i} \quad \text{.....(4.3)}$$

$$Mean\ Frequency = \sum_1^n (X_i * Y_{Norm}) \quad \text{.....(4.4)}$$

The absolute and mean frequencies are compared by calculating the FFT over two different time windows as illustrated in ***Fig. 4.10***: The complete signal and a 40-μs window after the arrival time is in the left plot. On the right, note the mismatch between some of the data points in the peak frequencies between different time windows; however, note the consistency between the mean frequencies in both windows.

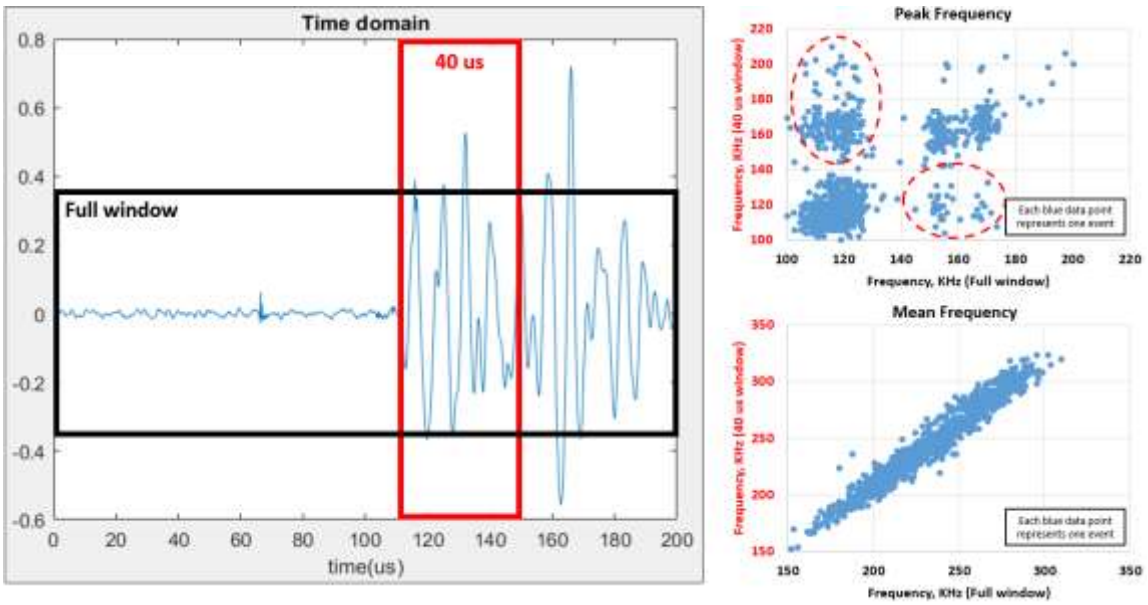


*Figure 4-10. Frequency response for two different time windows for one event. Note that the mean frequency method has a direct correlation between the 40 µs window and the full window. On the other hand, the peak frequency does not give the correlation, but shows some mismatch.*

***Fig. 4.12*** displays the frequency signal for different time windows after the arrival time. Peak frequency changes for every time window, being close to 100 kHz for 40 and 20-µs windows and significantly increasing for the 10-µs window (≈200 kHz). The peak frequency is dependent on many factors such as reflections, attenuation, and time window. The peak frequency is not the optimal parameter to indicate a dominant frequency for an individual event; however, it is useful to filter out noise events (See ***Fig. 4.11***).

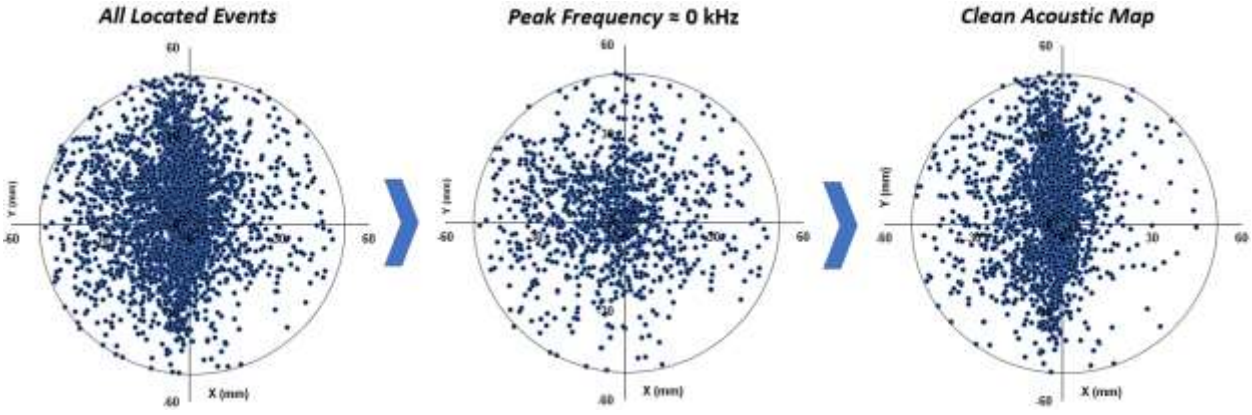


*Figure 4-11. Acoustic emission filtering through frequency. The left map shows all the located events, while the right figure has the map after removing those events with peak frequency near 0 kHz.*

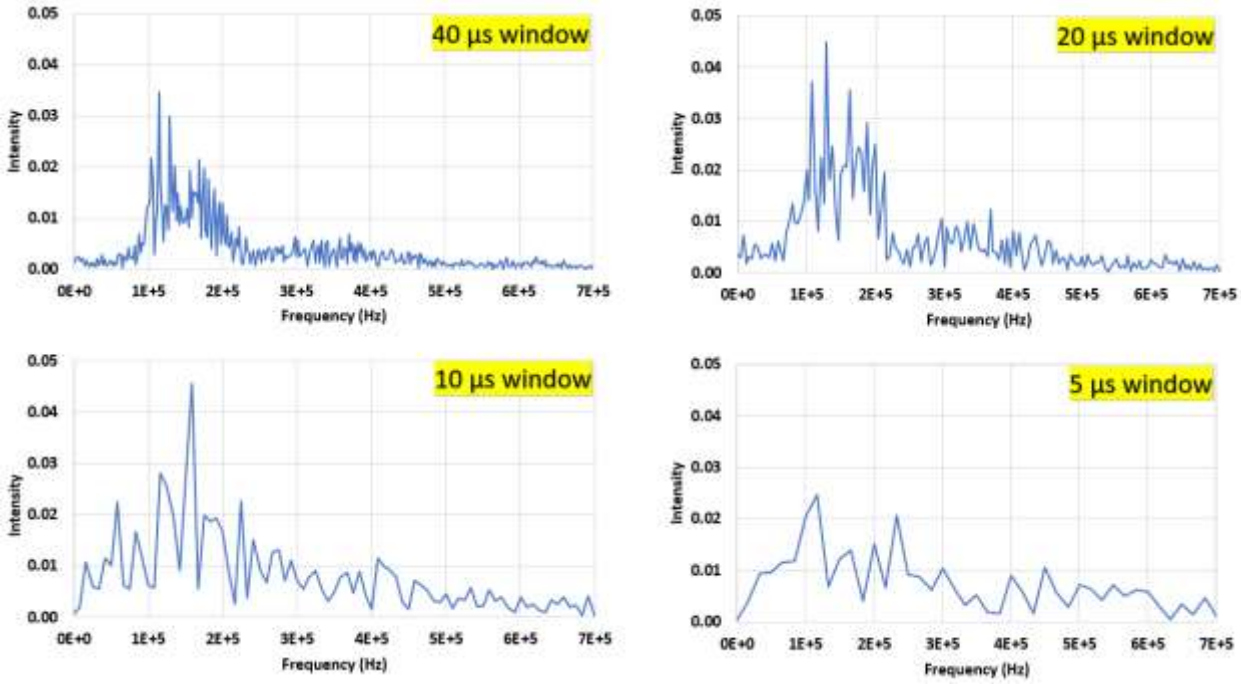


*Figure 4-12. Frequency spectral for different time windows. Note that the peak frequency changes for each image, showing variability across time windows. This is partly due to smaller windows mostly capturing the initial P-wave. The peak frequency is useful as it can separate whether the event is noise or an actual fracture event.*

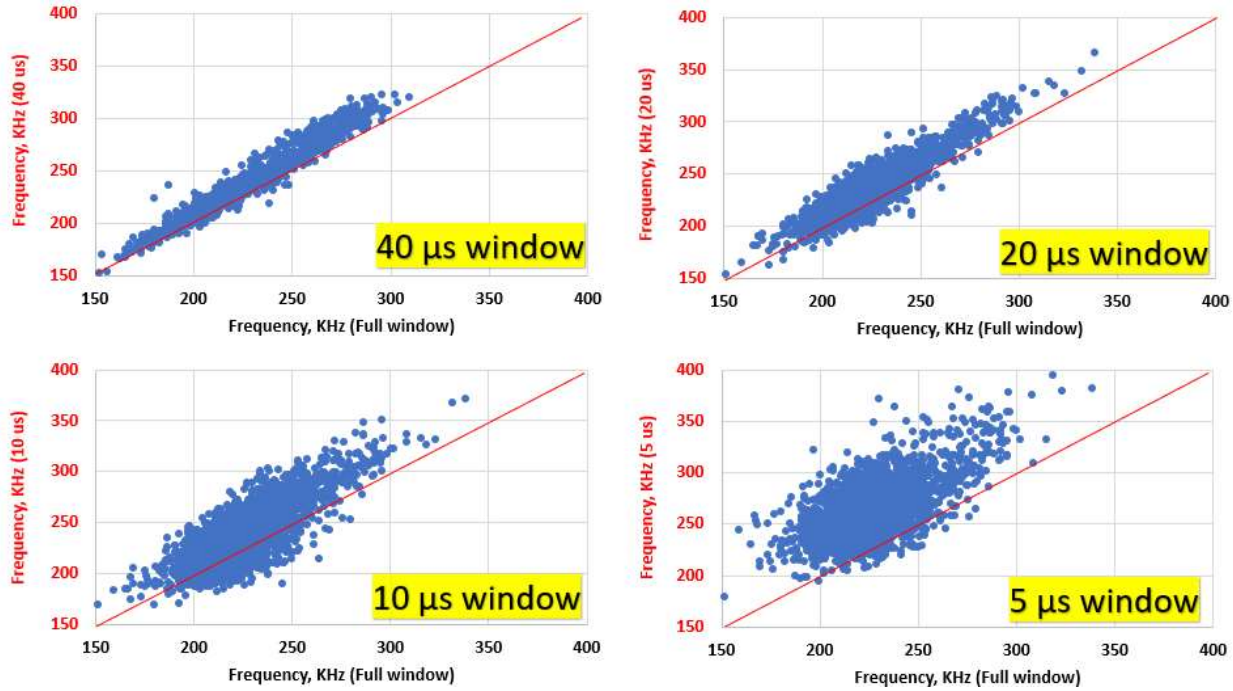


*Figure 4-13. Mean frequency correlation for different time windows. Using windows of 40 and 20 µs there is a strong correlation. For smaller time windows the trend is preserved, but the smaller time windows have a higher frequency meaning the earlier arrivals suffer less attenuation and perhaps reflect the source spectra more accurately.*

The mean frequency is consistent across time windows. ***Fig. 4.13*** shows a direct correlation in the mean frequency for the 40 and 20-μs windows. The correlation is weaker for the 10 and 5-μs windows. This is explained by two main factors: first, fewer data points affect the signal transformation as the resolution decreases. Second, the small-time windows mostly capture the P-wave arrival, while the longer time windows might partially have the P-wave and part of the S-wave and scattered or reflected waves. Note that the smaller time windows contain higher frequencies, which suggest P-waves have the highest frequencies.

*d) Seismic moment and b-values*

Event attributes are calculated to determine the failure mechanism associated with each crack event. Corner frequency, source radius, seismic moment, stress drop, displacement on the fracture plane, and moment magnitude are obtained. This section describes the method for calculating them:

***Corner Frequency***: Consider ***Fig. 4.14***, start with a time domain signal (A). The time signal is integrated (B). The signal is then detrended using a Matlab function (C). The FFT is executed over the resulting signal (D). Lastly, the logarithm is taken on both axis, and the change in trend between the low and high frequencies is the corner frequency (***Fig. 4.15***). Note that the y-axis corresponds to the displacement spectrum, $\Omega_o$, a parameter used to calculate the moment magnitude.

***Source Radius:*** also defined as the rupture length, it is a measure of damage of a specific crack. Using Eqn. 4.5 for corner frequency presented by Mizuno et al. (2013), the source radius, r , is calculated, where $V_p$ is the P-wave velocity and $f_c$ is the corner frequency.

$$r = \frac{2.34 * V_p}{2\pi * f_c} \quad \text{.....(4.5)}$$

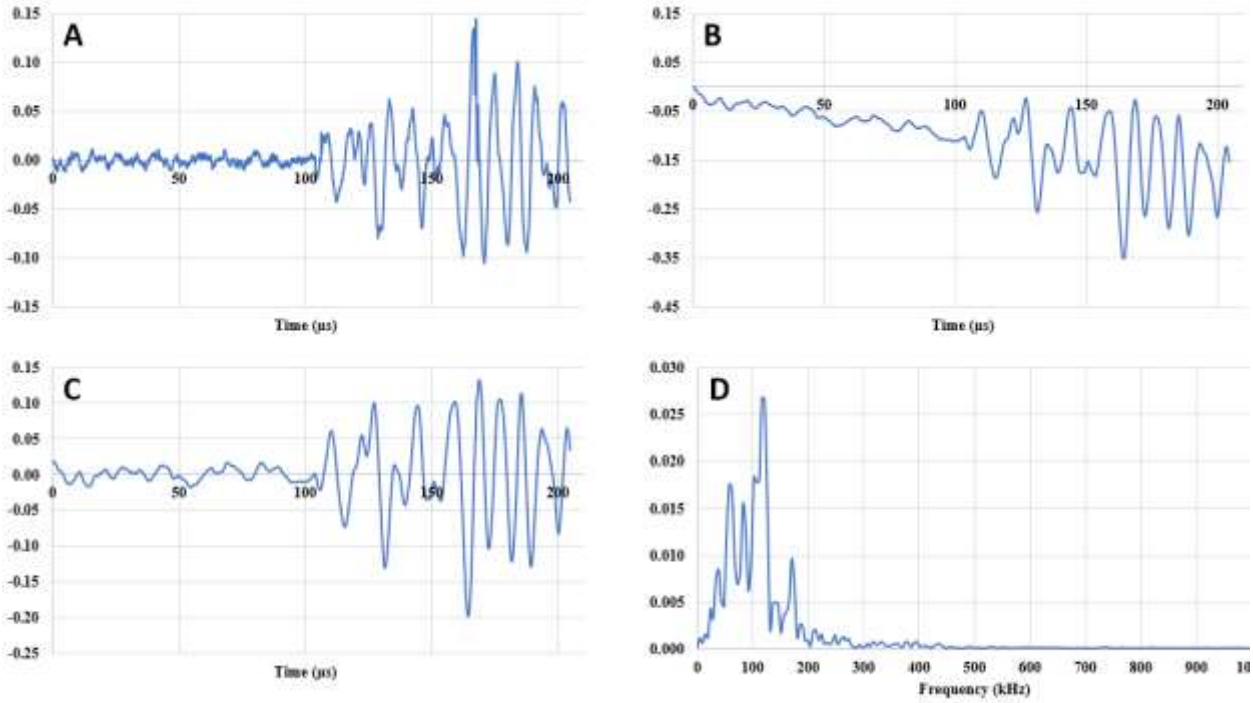


*Figure 4-14. A) Time domain waveform for one event. B) Area under the curve for the time domain waveform. C) Detrend waveform for the area under the curve. D) Frequency spectrum for the detrended waveform.*

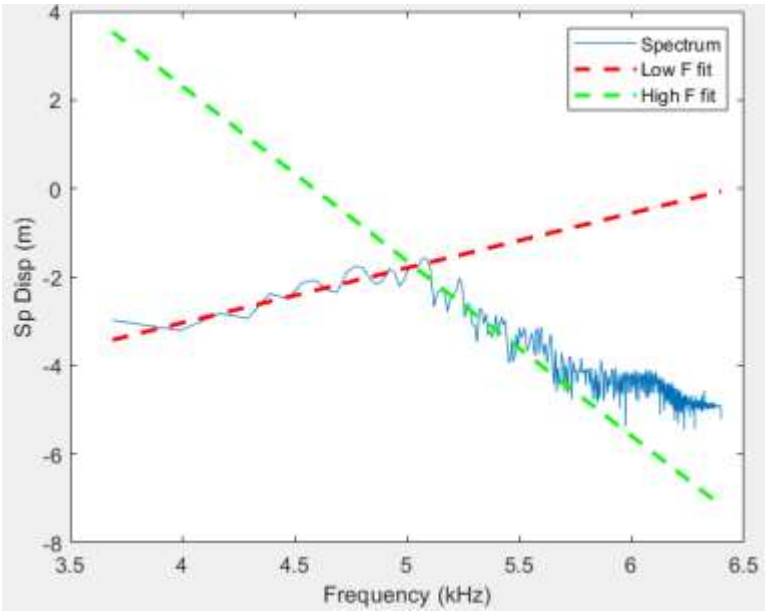


*Figure 4-15. Log-log plot for spectral displacement as a function of frequency. Low(red) and high(green) frequency fitted lines. The intersect is defined to be the corner frequency.*

***Seismic moment:*** the moment of an event is measured using Goodfellow et al.'s (2015) equation (see ***Eqns. 4.6 and 4.7)***. Both the seismic moment (Mo) and the moment magnitude (Mw) are used. Note that ρ is the bulk density, and R is the distance from the event to the source.

$$M_o = \frac{\Omega_o}{R_{o\emptyset}} 4\pi\rho R V_p^3 \qquad (4.6)$$

$$M_W = \frac{log_{10} M_o - 9.1}{1.5} \qquad (4.7)$$

***Stress drop:*** this is the difference between the stress across a fault before and after the rupture. ***Eqn. 4.8*** relates the seismic moment ($M_o$) and the source radius (r) on a circular fracture (Madariaga et al., 2007).

$$\Delta\sigma = \frac{7 * M_o}{16 * r^3} \qquad (4.8)$$

***Displacement on the fracture plane:*** using the seismic moment ($M_o$), the source radius (r), and the shear modulus (μ), the displacement on the fracture plane can be obtained by using ***Eqn. 4.9*** from Mizuno et al. (2013).

$$D = \frac{M_o}{\pi * r^2 * \mu} \qquad (4.9)$$

***b-value:*** using the Gutenberg-Richter magnitude frequency relationship, ***Eqn. 4.10*** is plotted with the logarithm of the number of earthquakes that exceed a specific magnitude (M) on the y-axis, versus the magnitude (M) on the x-axis. The negative slope is the b-value.

$$\log(N) = a - bM \qquad (4.10)$$

*e) Failure mechanism*

Field experiments have claimed that shear failure is the dominant mechanism for fracture propagation. In laboratory studies, having more events is often related to inducing more damage. We are also interested in classifying events as tensile, compressive or shear. Tensile events are thought to be associated with fracture initiation.

The polarity of the transducers was checked before the start of the test by performing a pencil break test. The transducers mostly showed a negative polarity. Positive first arrivals (up) were associated with tensile events, while the negative first arrivals are compressive failure (***Fig. 4.16***). Event classification is defined as having at least 85% of signals towards either positive or negative. If the event recorded mixed polarities, it was classified as shear. For the experiments performed in sections 4.2 and 4.3, two acoustic sensors were turned off due to noise in the system, thus, 14 transducers were active. Only events with at least 7 clean arrivals (polarity reading) were used to classify the event failure mechanisms.

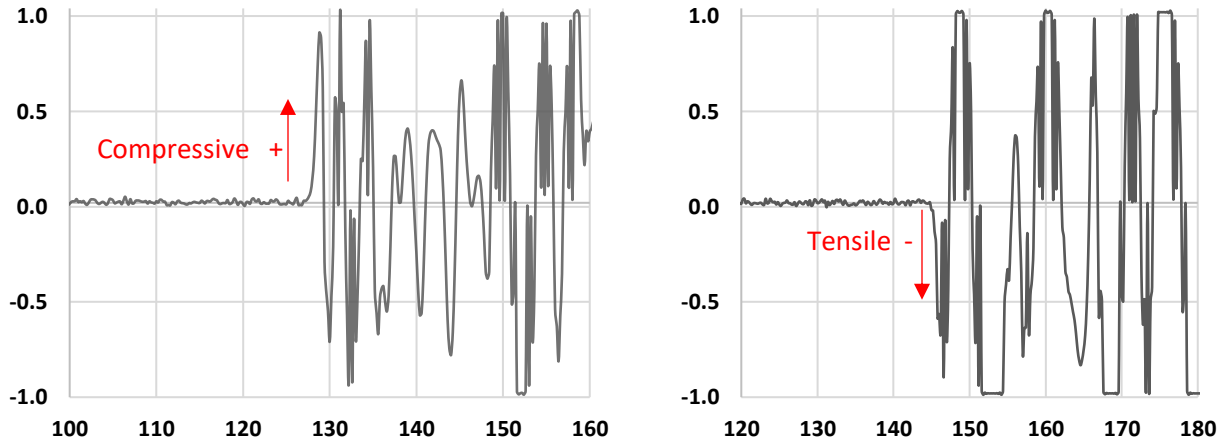


*Figure 4-16. Classification of events based on polarity of first arrival. Positive arrivals are classified as compressive while negative arrivals are tensile. Polarities were inverted because the transducers polarity was negative (Modified from Chitrala et al., 2013).*

## 4.2. Acoustic Attribute Analyses in Different Fracturing Protocols

In these experiments, microseismic attributes were used to evaluate the behavior of three hydraulic fracturing protocols. The acoustic emission attributes were analyzed in the time and frequency domains in three stages (Pre-breakdown, propagation, and shut-in or closure). ***Fig. 4.17*** shows the pressure curves for each protocol.

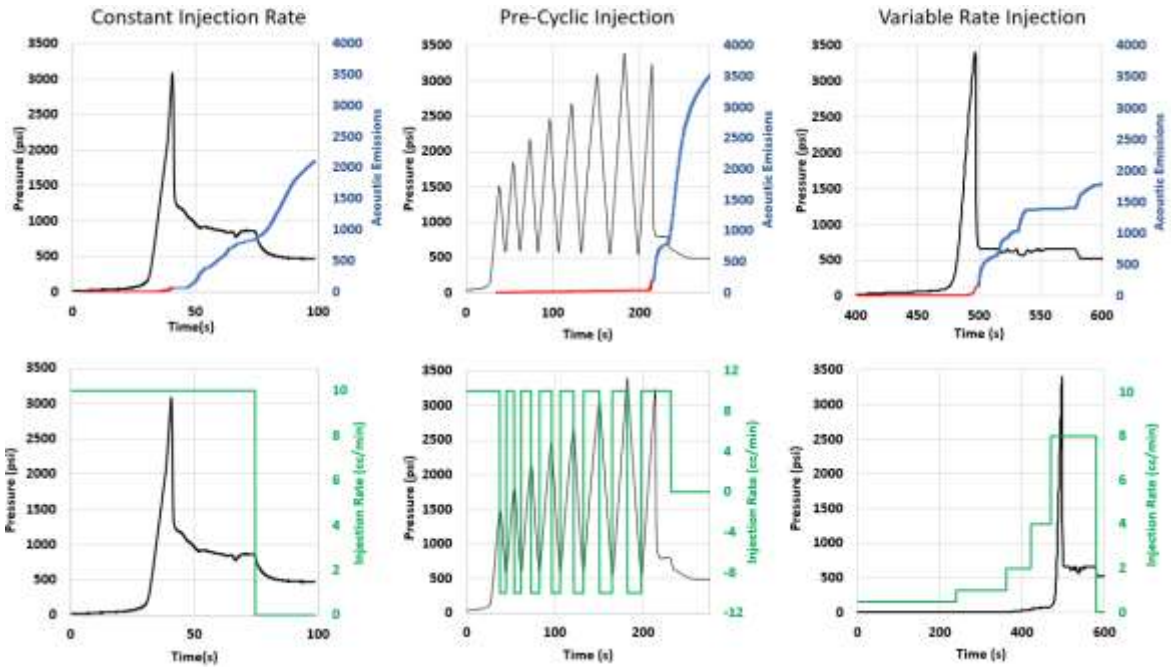


*Figure 4-17. Top row: Pressure (black) and locatable acoustic events pre-(red) and post-breakdown(blue). Note the significant number of events located in pre-cyclic injection. Bottom row: Pressure (black) and Injection rate (green) as a function of time. Note failure occurred on the 9th cycle of the pre-cyclic injection and at a much-reduced pressure.*

### *4.2.1 The protocols*

***Constant injection rate:*** the injection pressure increases at the injection rate of 10 cc/min. This was a monotonic test, meaning that pressure increased steadily until failure. This is the most common test used in the field.

***Pre-cyclic injection:*** this test increases pressure to a specific limit and then the pressure decreases to a base level, e.g., 500 psi. This is consistently performed, increasing previous pressure

by a set amount until breakdown is reached. Greater cumulative fluid volumes are injected before failure.

***Variable rate injection:*** the flow rate is changed as a function of time. Starting with 0.5 cc/min for 4 minutes, the flow rate was gradually increased by doubling it (1.0 cc/min, 2.0 cc/min) until reaching 8.0 cc/min, while the time for each rate was held to half the previous time (***Table 4.1***).

### *4.2.2 Results*

Acoustic emissions signals were used to locate events. Even though the number of recorded events was a reasonable indicator of the stimulated volume, the locatable number of events was better. Pre-cyclic injection produced the greatest number of locatable events compared to the other two testing protocols, suggesting a greater stimulated reservoir volume (SRV).

*Table 4-1. Protocol results for each test. The percentage of events located in constant rate injection was smaller than Pre-cyclic and variable rate tests. The injection volume was the highest in pre-cyclic injection.*

| | Total Events | Located Events | Breakdown Pressure [psi] | Injection Rate [cc/min] | Injection Volume [cc] |
|---|---|---|---|---|---|
| **Constant rate** | 17,283 | 2,184 | 3070 | 10 | 6.8 |
| **Pre-cyclic** | 9,648 | 4,041 | 3230 | 10 | 15.0 |
| **Variable rate** | 5,214 | 2,024 | 3408 | Variable | 12.8 |

The frequency spectra were calculated for each stage (pre-breakdown, propagation, and shut-in) in the three experiments. Overall, the propagation and shut-in phases showed a similar frequency response in each test; however, the ranges fluctuated between tests (**see *Fig. 4.18***). Pre-breakdown events showed a significantly higher frequency response as compared to those events after failure. This could be due to difference in source mechanism, crack density or attenuation.

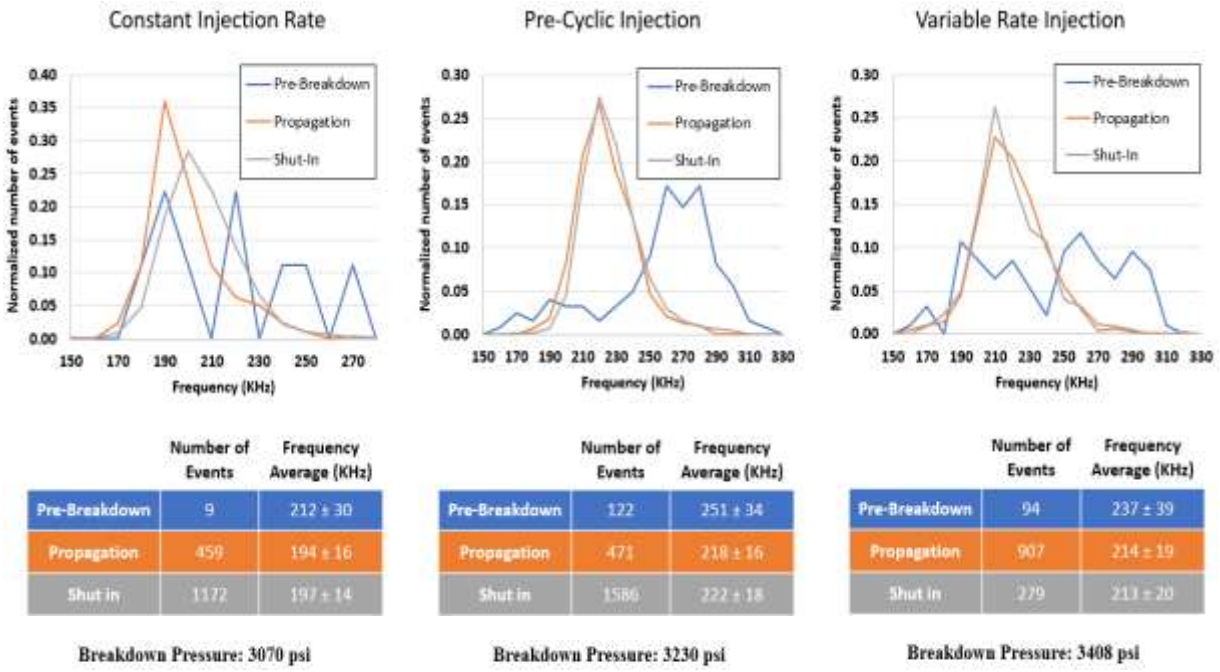


*Figure 4-18. Frequency distribution for each experiment. Pre-breakdown events had the highest frequencies. Note that shut-in phases tend to locate a larger number of events as compared to the propagation phase.*

The constant injection rate recorded most of the locatable events after breakdown, with a frequency between 150 to 270 kHz. Only 9 events appeared before the breakdown. In addition, frequencies were analyzed for propagation and shut-in, having similar ranges with an average of 195 ± 15 kHz.

The pre-cyclic injection test recorded similar frequencies between the propagation and shut-in stages; however, recorded frequencies were higher in the constant injection rate test (220 ± 17 kHz). The average frequency for pre-breakdown events (251 ± 32 kHz) was significantly higher than any other phase. These frequency differences suggested a different failure mode.

Lastly, in the variable pumping rate, the propagation phase recorded the larger number of locatable events, with the pre-breakdown events having a marginally higher frequency than in propagation and shut-in phases. Within the pre-breakdown events, there were two frequency ranges; the first matched the propagation ranges (200 ± 20 kHz), occurring in the early times, while

the second group was significantly higher frequency (268 ± 18 kHz), and these events corresponded to the last 2 seconds before failure. This implied that two different types of failure mechanisms were induced.

The acoustic map for each test is shown in ***Fig. 4.19***. The constant rate fracture test had a planar fracture with the greatest length, while the pre-cyclic test had the highest crack density, with the most damage near the wellbore.

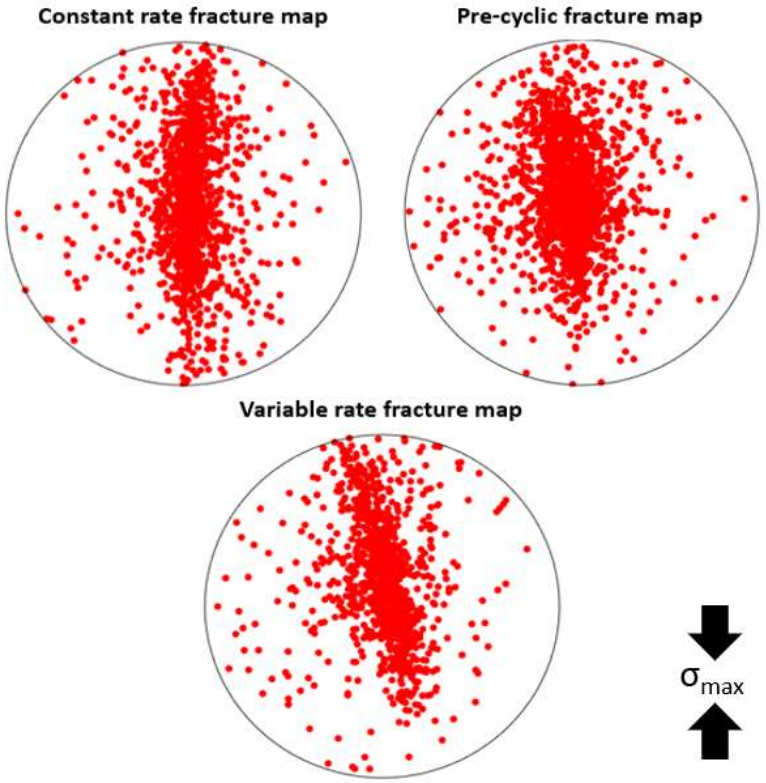


*Figure 4-19. Acoustic emission map (plan view looking down on the sample) for each test post-filtering. Pre-cyclic injection shows a wider fracture as compared to constant rate and variable rate tests. The variable injection rate test appears to have the narrowest distribution. Note the orientation of the main fracture is the same in all tests, aligned with the maximum horizontal stress direction. The samples were brine saturated Tennessee sandstones.*

### *Pre-breakdown analysis*

Further analysis was carried out on the pre-breakdown events based on the frequency content, in the pre-cyclic and variable rate tests; the constant injection rate test had too few events to warrant analysis.

In pre-cyclic injection, the first six cycles averaged a frequency of 200 kHz; however, the last two cycles noted frequencies higher than 250 kHz and up to 310 kHz (***Fig. 4.20***). After fatiguing the rock, the last cycles overcame a critical threshold and initiated new fractures, even with higher frequency changes before final failure suggested a different failure mechanism.

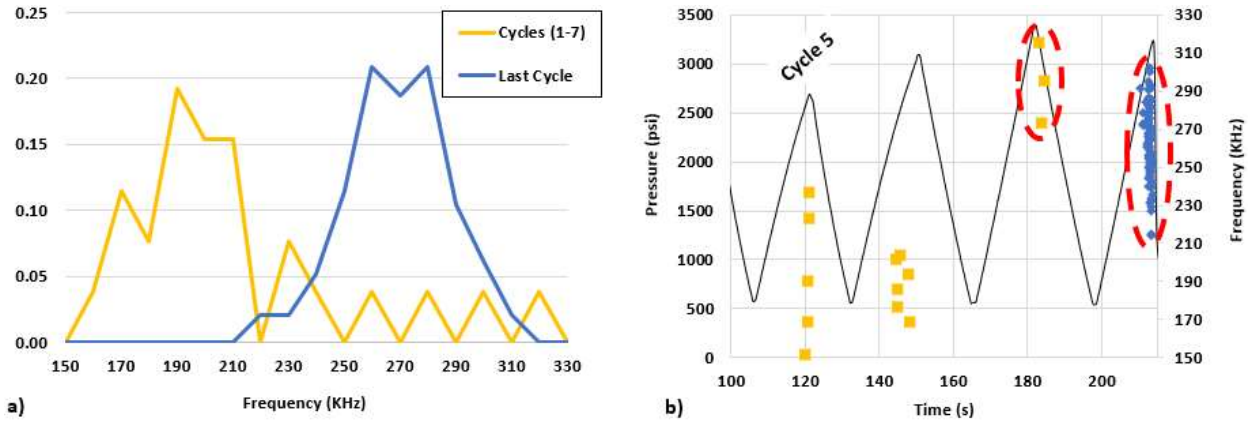


*Figure 4-20. Frequency distribution for pre-breakdown events in cyclic injection. Note the bimodal distribution with the first cycles showing lower frequencies, and the last cycle having a higher frequency. b) pressure as a function of time with the event frequencies. Cycles 7 and 8 recorded the highest frequency.*

In the variable pumping rate test, two frequency ranges were recorded (***Fig. 4.21***). Early events recorded a similar frequency to those in the propagation and shut-in phases, while latter events (2 seconds before failure) had a considerably higher frequency. The unexpected and abrupt change in frequency before failure suggested a transition to new and different failure mechanisms

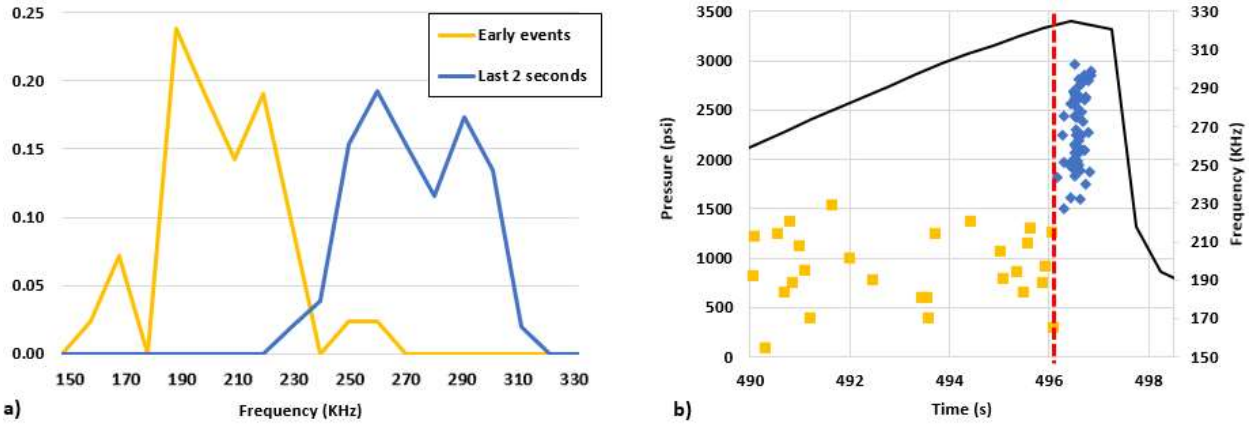


*Figure 4-21. a) Frequency distributions for events in the variable injection rate test at different times. Note again the bimodal distribution. b) injection pressure (black) as a function of time with the recorded event frequencies. The last second contains events with significantly high frequencies, suggesting a change in source mechanisms since damage is at its maximum.*

***Amplitude***

The average amplitude was calculated through an arithmetic average with the available signals per event. ***Fig. 4.22*** displays the logarithm of the number of events having an average amplitude greater than an amplitude (A), with the pre-breakdown phase on the left and the propagation phase on the right. The pre-cyclic test had the highest amplitude in both pre-breakdown and propagation phases. The constant injection test was not analyzed during pre-breakdown because there were too few events. Additionally, propagation events possessed higher amplitudes as compared to pre-breakdown.

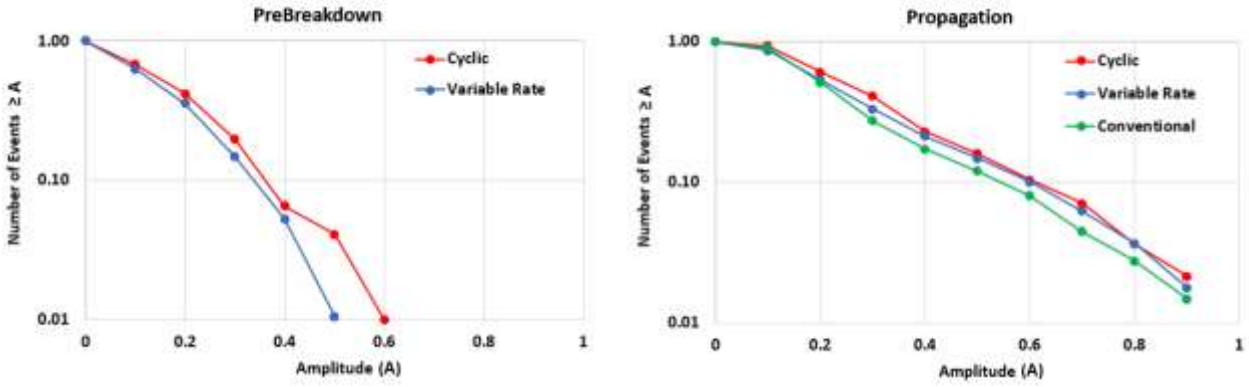


*Figure 4-22. Normalized distribution of acoustic event amplitudes for both pre-breakdown (left) and propagation (right) phases. Pre-cyclic (red) injection has the highest amplitudes during both phases.*

Wave amplitude was compared with frequency for the pre-cyclic injection events (***Fig. 4.23***). Pre-breakdown events showed a low amplitude range, between 0.05 to 0.4 (m.u). The pre-breakdown events with a high-frequency range (250-310 kHz) were considered part of the crack initiation. The propagation and shut-in events showed a large range in amplitude but with no correlation to frequency.

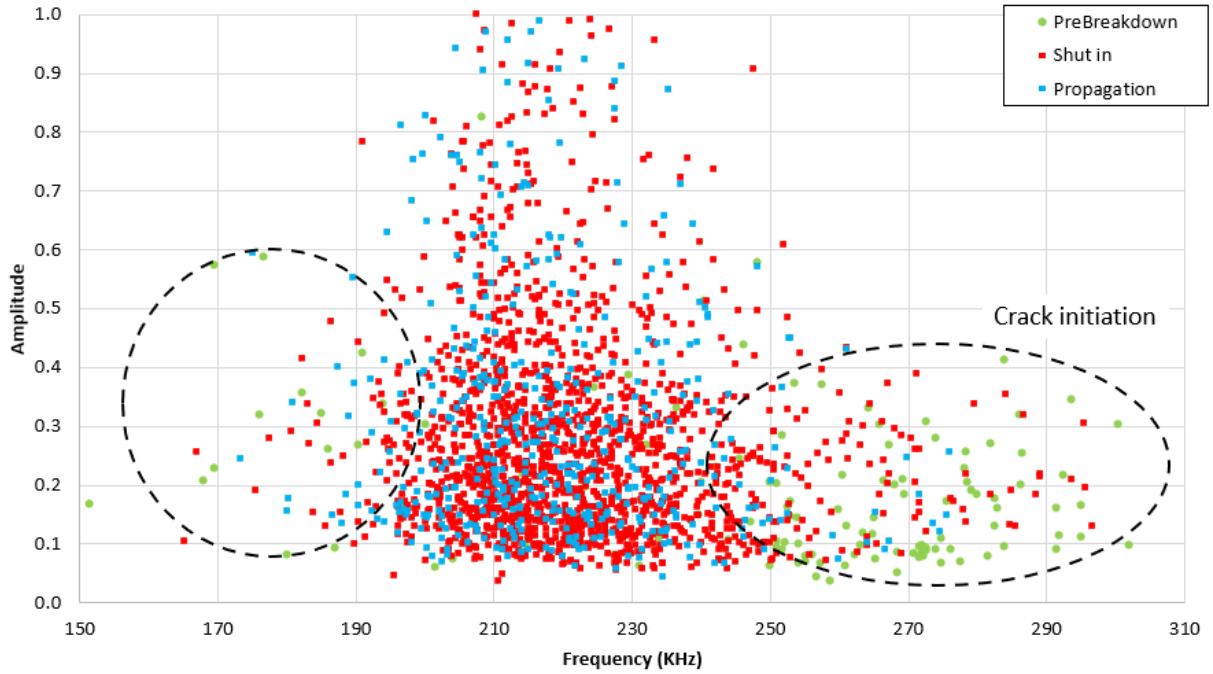


*Figure 4-23. AE event amplitudes versus event frequency. Pre-breakdown events are characterized by low or high frequencies, and low amplitudes. The propagation and closure phases have higher amplitudes. The highest frequencies are associated with the pre-breakdown events.*

***Attenuation***

Attenuation is a significant factor affecting the frequencies in recorded events especially under saturated or partially saturated conditions (Shatilo et al., 1995). Using data from a saturated Tennessee sandstone from Patel et al. (2016) fractured under pre-cyclic injection, a comparison was made between the AE frequency content for dry and saturated conditions. The events recorded in the saturated sample showed lower frequency ranges, i.e., consistently 20% less than the dry sample (***Fig. 4.24a***). Furthermore, the pre-breakdown phase dominated the brine-saturated test. The saturated sample showed a main spectral peak near 100 kHz (***Fig. 4.24b***).

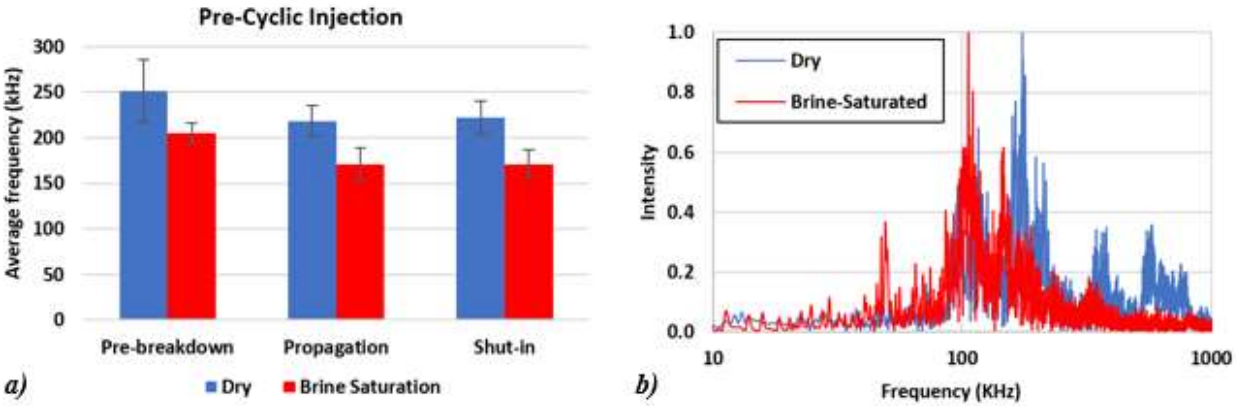


*Figure 4-24. a) Average frequency for AE events recorded in saturated vs dry pre-cyclic injection tests. Note that Pre-breakdown events have the highest frequencies. b) Frequency signals for one event in dry and brine-saturated tests. Not the faster decay of high frequencies in the saturated sample as compared to the dry.*

### *4.2.3 Discussion*

Acoustic emissions are essential to understanding failure modes in hydraulic fracturing experiments. High-frequency events (250-310 kHz) were dominant during pre-breakdown in both pre-cyclic and variable rate testing, especially within the last 5 seconds before failure. Tensile failure is associated with high-frequency events. Shear events are associated with low-frequency events during propagation and closure. This is consistent with observations of Chitrala et al. (2013) and Damani et al. (2018), where focal mechanisms showed tensile events to occur mainly in the early propagation phase.

Locatable acoustic emissions are directly correlated with crack density. ***Fig. 4.25a*** shows that most of the acoustic events occurred within 1 cm of the main fracture. Using a threshold of 250 kHz to account for high frequency events, events with higher frequency than 250 kHz occurred within 1 cm of the main fracture and decayed with distance away from the main fracture plane (***Fig. 4.25b***). Grain size is a parameter that should be considered to analyze the different frequency and amplitude ranges.

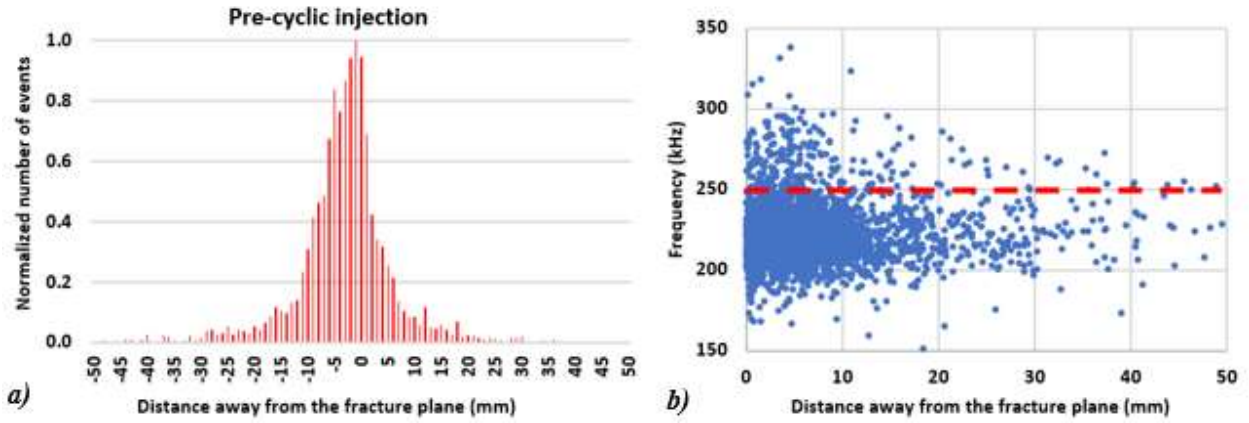


*Figure 4-25. a) Normalized number of AE events for pre-cyclic injection. The center of the distribution does not occur at 0, but it is slightly to left. b) Event frequency as a function of distance away from the fracture plane. Note that high frequency events occur close to the wellbore, while low frequency are more distant.*

The projection of the hypocenter distribution of the events was fitted to a Lorentzian function with distance away from the fracture plane (***Eqn. 4.10***), where $I$ is the peak height, $x_0$ is the location parameter, and γ is the scale parameter to determine the spread.

$$f(x) = \frac{I}{\left[1+\left(\frac{x-x_0}{\gamma}\right)^2\right]} \quad \text{.....(4.10)}$$

***Fig. 4.26*** shows the AE event distribution along the fracture and the z-axis for each test. Constant injection rate had the smallest γ, with the smaller process zone, which agrees with the secondary fracture count by Patel et al. (2016). The greatest process zone was calculated in the pre-cyclic injection, which also had the highest spread, explaining the greatest event distribution away from the fracture plane and potentially having the highest recovery on the field scale. Furthermore, a higher process zone also implies a higher surface area, which is crucial in EOR experiments.

The pre-cyclic injection was the test that yielded the greatest fault length and process zone. Values of the 5-cm fault length and the 1-cm process zone are consistent if scaled to field

observations and natural faults developed by Zang and Stephansson (2010) as illustrated in ***Fig. 2.1***.

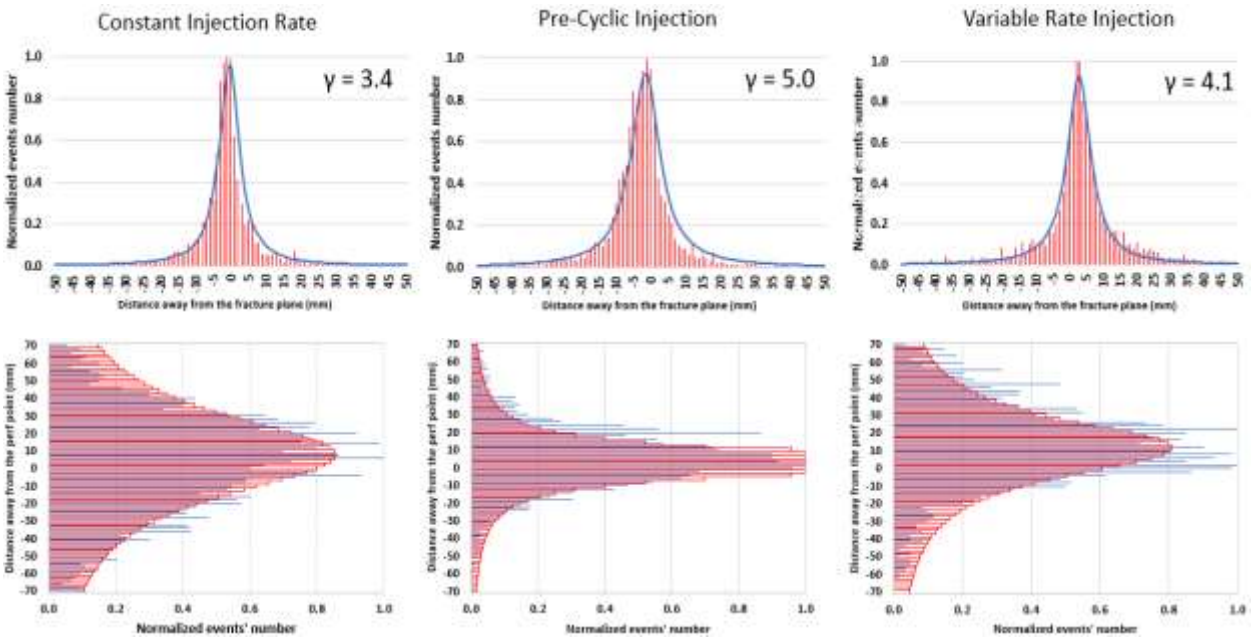


*Figure 4-26. Normalized fracture distribution with respect to the maximum number of events for each test. The γ defines the event spread in the fracture axis. Pre-cyclic injection has the largest spread. Constant injection shows the smallest spread. In the vertical direction, the events for pre-cyclic occurred more in the perforation area, while the other tests show a wider vertical distribution. Note that the pre-cyclic test had a higher number of events.*

Even though the amount of fluid used in pre-cyclic injection was greater than for the constant injection test by 25%, the number of locatable induced events by pre-cyclic injection was 85% higher, suggesting a significant surface area difference with the volume addition. It is recommended for operators to follow pre-cyclic injection in the field as more damage is created. The induced fracture intensity is greater, which creates greater surface area for better recoveries in EOR studies.

## 4.3. Pre-Cyclic Injection Study

The pre-cyclic injection was an effective and damaging protocol. Compared with experiments such as constant or variable rate injection, the pre-cyclic test generated more locatable acoustic emissions, suggesting higher process zones. However, larger quantities of fluid were injected. A method for reducing injection time was desired. As such, it was decided to study cyclic injection further, in this case, reducing the number of cycles, aiming for an optimal number that can create damage with less fracturing time and fluid volume.

### *4.3.1 Methodology: the protocols*

Three different tests are performed. As described in the previous section, 8 cycles were used for cyclic injection at dry conditions. The following tests were performed under 2.5% KCl saturation. Because of the weakening that saturation causes in sandstone, fewer cycles were used. The baseline was set to 500 psi, and the number of cycles in the tests was 2, 4, and 6. The measured pressure using monotonic injection (1-cycle) was 2872 psi.

### *4.3.2 Results*

The analysis will consist of pressure and acoustic events curves versus time, permeability data, SEM imaging, acoustic emission attributes and source parameters. Focus will be on the located events instead of the total recorded events, being consistent with the previous section (***Table 4.2***).

*Table 4-2. Total number of events per phase on each test. The total recorded events are in the left while the located number of events are in parenthesis. Note that the test with 6 cycles has the greatest number of events.*

| | Total Number of Events (Located) | | | |
|---|---|---|---|---|
| | **Pre-Breakdown** | **Propagation** | **Closure** | **Total** |
| **2-Cycles** | 62 (32) | 2027 (655) | 1817 (808) | 3910 (1523) |
| **4-Cycles** | 82 (29) | 4447 (1508) | 1938 (1048) | 6698 (2685) |
| **6-Cycles** | 165 (102) | 4740 (2038) | 2169 (1262) | 7203 (3479) |

- **HF Cyclic Injection: Two cycles**

The first cycle ramped injection pressure to 1900 psi, and the second was increased to failure. 1900 psi was selected because it was enough pressure to cause damage in the sample although not enough for failure in one cycle (monotonic). Note that this pressure is equivalent to 66% of the breakdown for monotonic injection. With this method, the sample fractured at 2588 psi (***Fig. 4.27***).

Slightly more than 60 events were induced before breakdown, with 32 located. During propagation, 655 were located, where most of them occurred within the first 10 seconds. The closure phase had the most located events (808). Note that the percentage of located events was higher during closure than propagation.

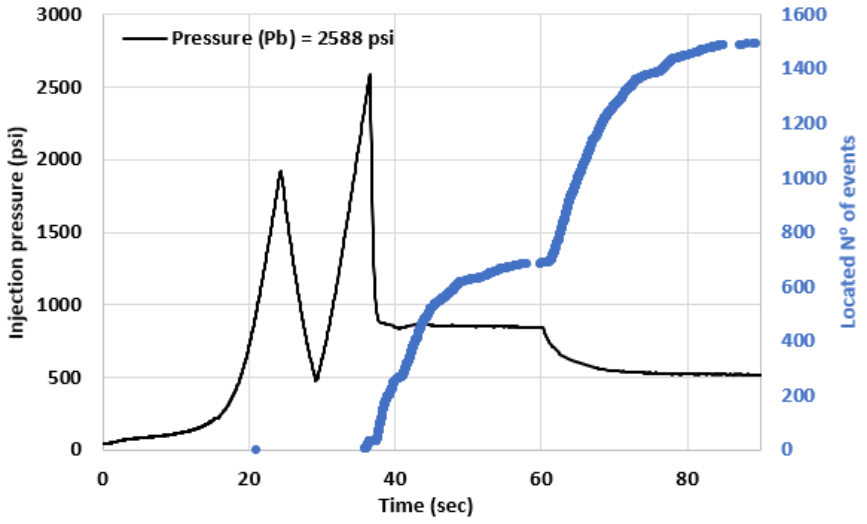


| Cycles | Pressure (psi) |
|---|---|
| Cycle No 1 | 1900 |
| Cycle No 2 | 2588 |

*Figure 4-27. Injection pressure and acoustic events vs time. The number of events increase during propagation and closure. Note that the first cycle was about 75% of the breakdown pressure.*

***Fig. 4.28*** shows injection pressure as a function of time (black), with the event rate per second (red). After breakdown, there is a rapid increase in the event rate with approximately 250 events per second during the first 7 seconds. As time progresses, the event rate declines, and after 10 seconds, it is about 25 events per second, which is 10% of the event rate at its peak. Once shut-

in starts, there is a quick ramp-up in events followed by a new decline. Note that the event rate is slightly higher during propagation than during closure.

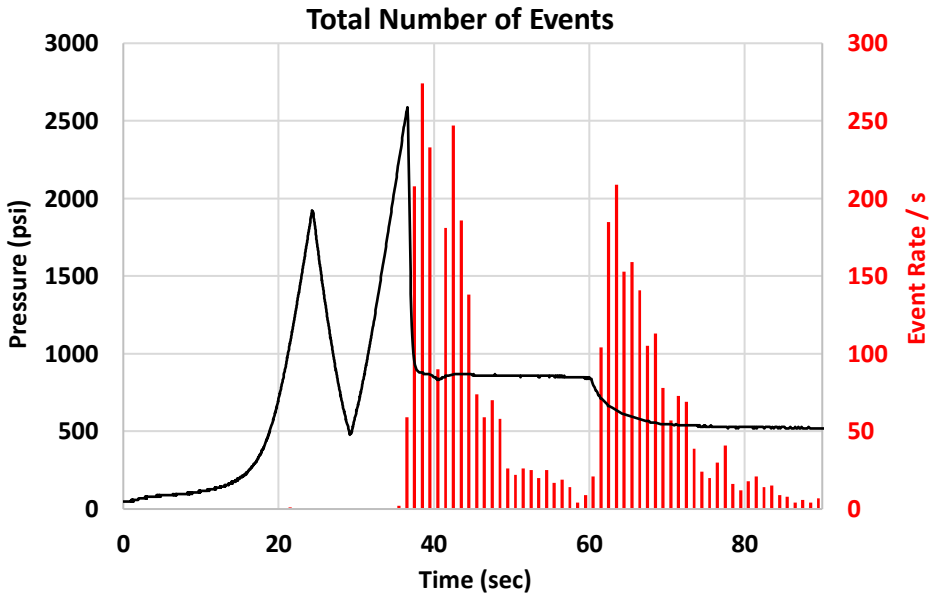


*Figure 4-28. Injection pressure and event rate vs time(s). There is a rapid increase in the number of events after breakdown followed by a decline after 7 seconds. The events rate increases again after closure.*

- **HF Cyclic Injection: Four cycles**

The first cycle ramps injection pressure to 1450 psi, equivalent to 50% of the monotonic breakdown, and gradually increases by 400 psi until reaching breakdown (***Fig. 4.29***). The cycle number 4 is programmed to reach 2650 psi, an injection pressure higher than breakdown for the 2-cycle test ($P_b$ = 2588 psi).

The first three cycles produced a small number of acoustic events, but the last cycle recorded 82 events before failure, with only 29 located. The breakdown pressure was 2432 psi, decreasing by 6% with respect to the 2-cycle test. Furthermore, the number of acoustic events induced during propagation increased significantly, with over 4000 events recorded, and with 1508 located. After shut-in, close to 2000 acoustic events were induced. There was an increase of 71% in the total recorded acoustic emissions and 76% in the located emissions.

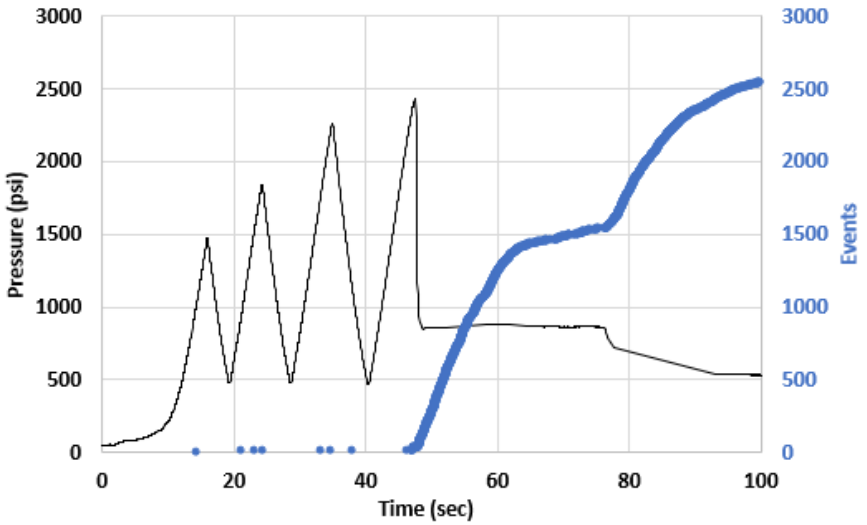


| Cycles | Pressure (psi) |
|---|---|
| Cycle No 1 | 1450 |
| Cycle No 2 | 1850 |
| Cycle No 3 | 2250 |
| Cycle No 4 | 2432 |

*Figure 4-29. Four cycle experiment. There is an increase of 400 psi per cycle after starting with 1450 psi. The fourth cycle reached pressures between 2250 and 2650 psi; sample fractured at 2432 psi.*

An event rate of 400 events per second was reached after breakdown (***Fig. 4.30***). The rate holds and decreases over time. Note that there are over 200 events recorded per second post-breakdown during almost 15 seconds. The peak only rises to 200 events per second during closure, similar to observations in the 2-cycle test. The main difference in the acoustic emissions count happens during fracture propagation, which significantly exceeds the previous test.

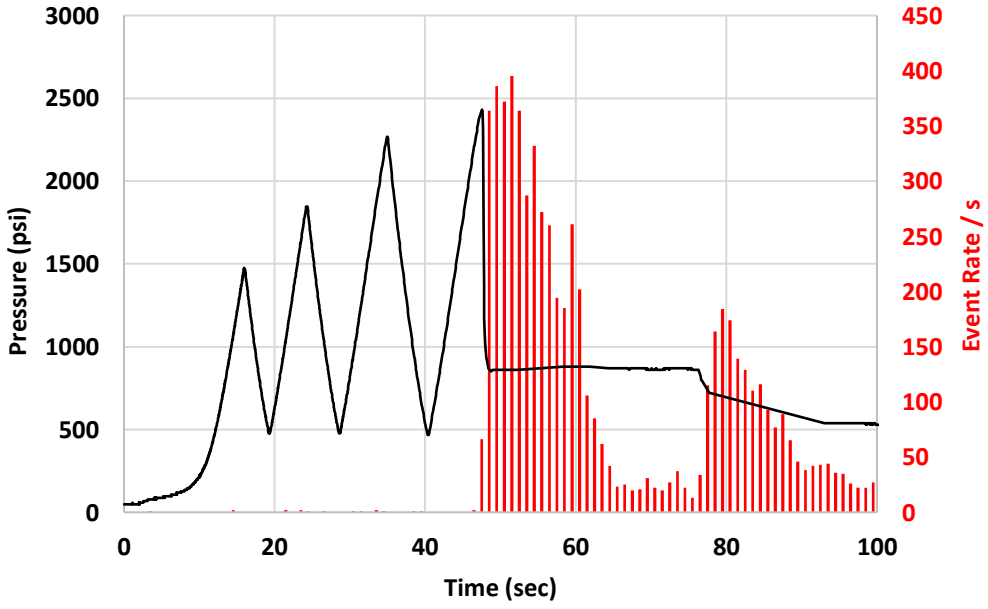


*Figure 4-30. Pressure and event rate as a function of time. The 4-cycle test shows a rapid increase but that holds longer than for the 2-cycle test. About 400 events per second are recorded during propagation.*

- **HF Cyclic Injection: Six cycles**

The 6-cycle test was initially expected to have the lowest breakdown pressure and the AE highest count. An initial injection pressure of 1250 psi, which was equivalent to 40% of the monotonic breakdown, was followed by increments of 250 psi. The sixth cycle was set to reach 2500 psi, pressure higher than the breakdown in the 4-cycle test (***Fig. 4.31***).

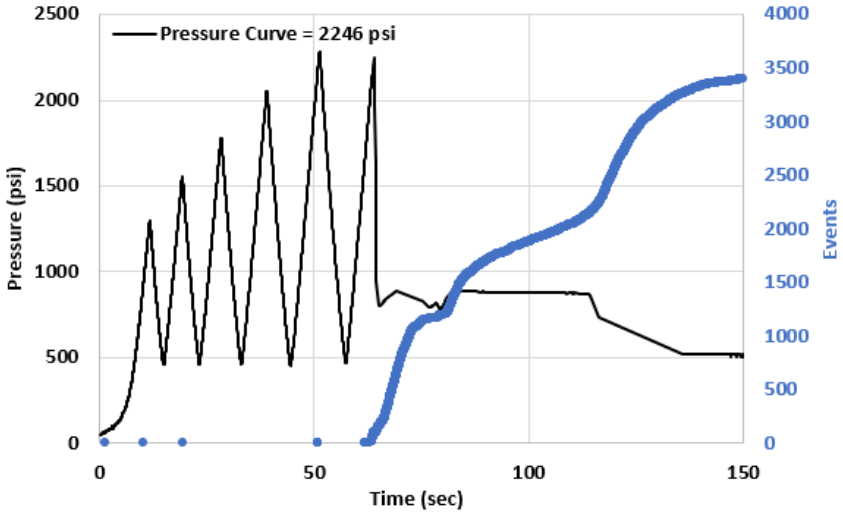


| Cycles | Pressure (psi) |
|---|---|
| Cycle No 1 | 1250 |
| Cycle No 2 | 1500 |
| Cycle No 3 | 1750 |
| Cycle No 4 | 2000 |
| Cycle No 5 | 2250 |
| Cycle No 6 | 2500 |

*Figure 4-31. 6-Cycle test. It had the largest number of acoustic emissions (3476), while it also had the lowest breakdown pressure (2246), being the most efficient. It also consumed the largest fluid volume before breakdown. Note the pressure steps are lower than the previous tests.*

The breakdown pressure decreased, only 2246 psi. It was lower than the breakdown pressure in the 4-cycle test (by 8%) and 2-cycle test (by 13%). During pre-breakdown, the number of events was considerably higher, twice the number of events and located three times more events than other tests. Propagation and closure were not significantly different from the 4-cycle test. However, the percentage of located events was 48% of events, the highest among all tests.

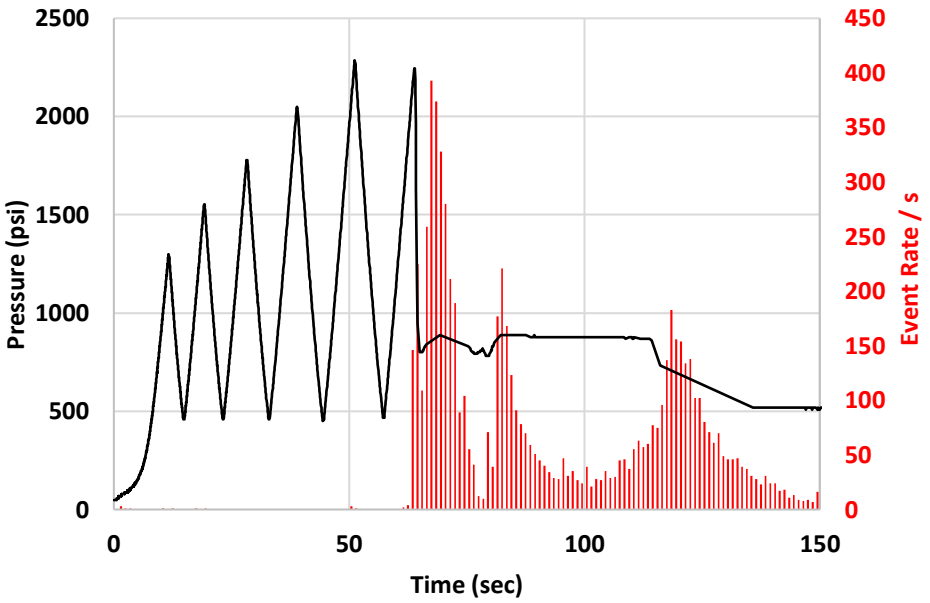


*Figure 4-32. Rate of AE events per second for the 6-cycle test. There is a sharp increase in events at failure which is followed by a rapid decrease, and a second increase. A third increase in events occurs during closure.*

The plot of the rate of events per second (***Fig. 4.32***) showed two main characteristics: 1) during propagation, two ramps were observed. Initially, the first peak reached 400 events per second, followed by a steady decay, and a second peak which reached 220 events per second. 2) the closure signature was comparable to the other tests. This implies that the main difference in events' count across each test occurs during fracture propagation.

A comparison of events rate per second for each test is presented in ***Fig. 4.33***. The increase in event rate after failure is different for each test. The 4- and 6-cycle tests had similar performance within 10 seconds after failure, recording up to 400 events per second and significantly higher than the recorded with 2 injection cycles. Notice that the 6-cycle test had longer recording times after failure as compared to the other tests, explaining the difference between the number of events per test. It shows that in terms of acoustic emissions, both the 4-cycle and 6-cycle tests create a similar damage which would suggest 4-cycles are more optimal than 6.

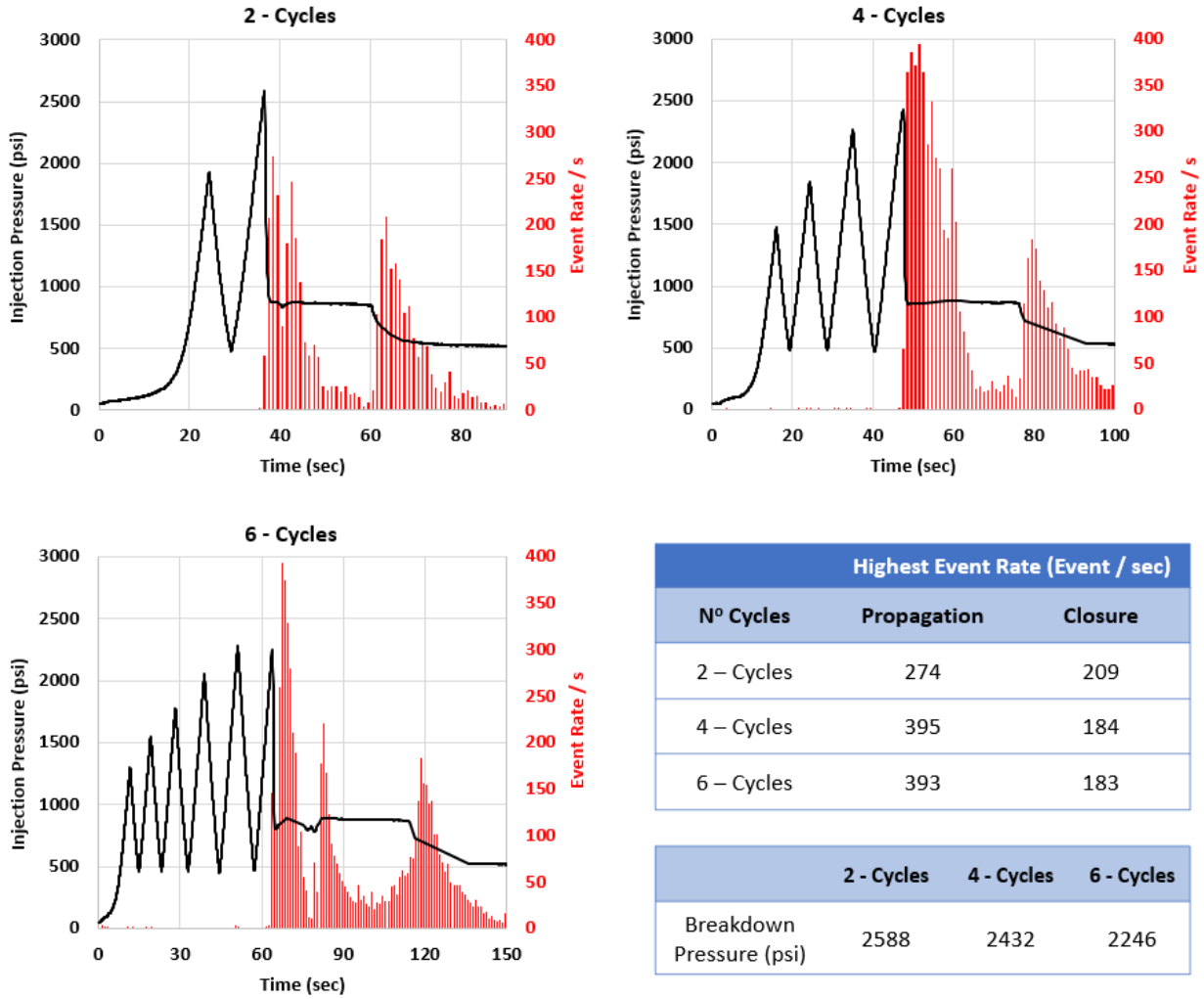


| | Highest Event Rate (Event / sec) | |
|---|---|---|
| Nº Cycles | Propagation | Closure |
| 2 – Cycles | 274 | 209 |
| 4 – Cycles | 395 | 184 |
| 6 – Cycles | 393 | 183 |

| | 2 - Cycles | 4 - Cycles | 6 - Cycles |
|---|---|---|---|
| Breakdown Pressure (psi) | 2588 | 2432 | 2246 |

*Figure 4-33. Rate of AE events per second for all the tests. Note the similarity on the event distribution and event count during the closure phase. The peak during propagation increased for the tests on 4 and 6 cycles. Rates suggest 4-cycles might be optimal.*

The breakdown pressure decreased as a function of number of cycles (***Fig. 4.34***). Based on our testing conditions, the more cycles were used contributed to the reduction of breakdown pressure. The 6-cycle test had the greatest reduction of breakdown pressure, with 22% reduction with respect to the monotonic breakdown. This is a significant development for operations performed deep in the formation, and with rocks that require greater injection pressure, such as granite.

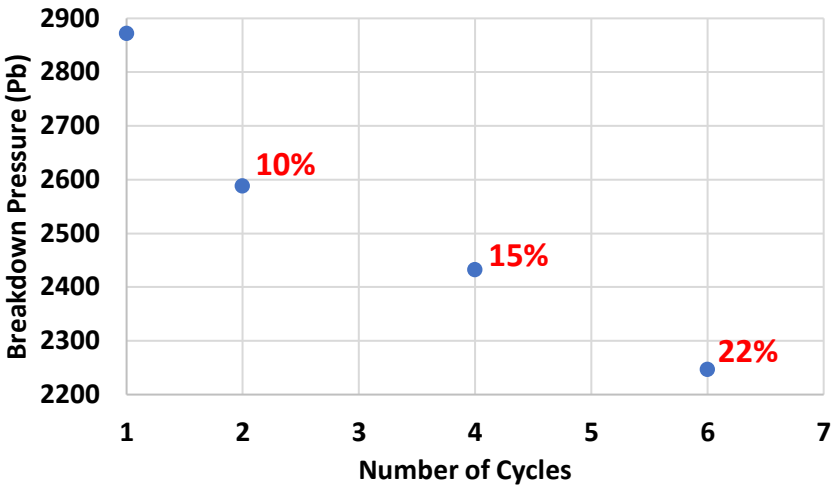


*Figure 4-34. Reduction in breakdown pressure with respect to the number of cycles. The 6-cycle test had a 22% reduction, with the greatest reduction as compared to the other two tests.*

- **Acoustic Emission maps and fracture distributions**

The acoustic emissions were mapped from the top view and paired with the corresponding fracture side view (***Fig. 4.35***). The events that showed a peak frequency near 0 kHz (0.5-1.0 kHz) were eliminated as these events are considered noise and do not represent the main fracture.

For the 2-cycle test, the maps show most of the events located around the wellbore, with an orientation towards the maximum horizontal stress. The events were located within 30 mm of the main fracture. The side view shows that the events are mainly in the upper half of the sample, with fewer events located towards the bottom of the sample.

The AE distributions for the 4-cycle test is far broader in the top view. The acoustic emissions reached a farther extent. The fracture side view shows the right wing (positive) to have more events towards the center of the sample. The left wing is wider from top to bottom.

The 6-cycle test shows the most compact fracture from the top view. The fracture is slightly deviated from the maximum horizontal stress direction, with a deviation of $5^{o}$. The map shows the events in the middle of the sample, reaching part of the bottom section but mainly located in the top half.

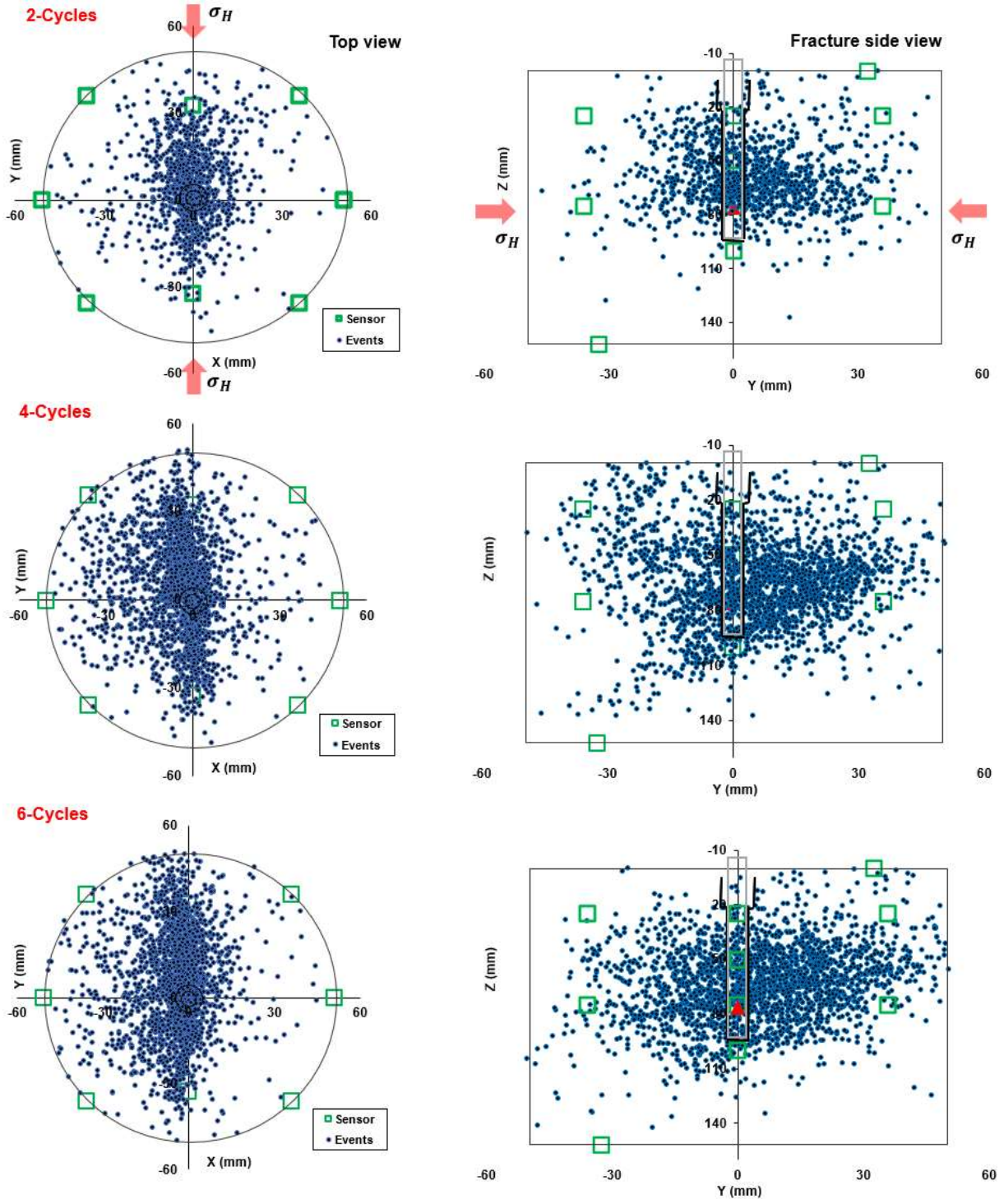


*Figure 4-35. Acoustic map from the top view (left) and fracture plane side view (right) for the 2, 4 and 6-cycle tests. The 4- and 6-cycle tests show a more composed fracture distribution across the sample. These plots only show events that passed the frequency filter as the others are considered noise.*

The fracture distribution on both the fracture plane and the z-axis were fit to a Lorentzian function as described in section 4.2 (***Fig. 4.36***). The distribution in the y-axis was normalized with

respect to the greatest number of events on a 5 mm interval among the three tests. Propagation is always stronger in one of the fracture wings, contrary to symmetry assumed in field tests. There is a significant difference between the 2-cycle test and the remaining tests. The 6-cycle test shows a slightly greater number of events in the center than the 4-cycle test; however, the difference is minimal.

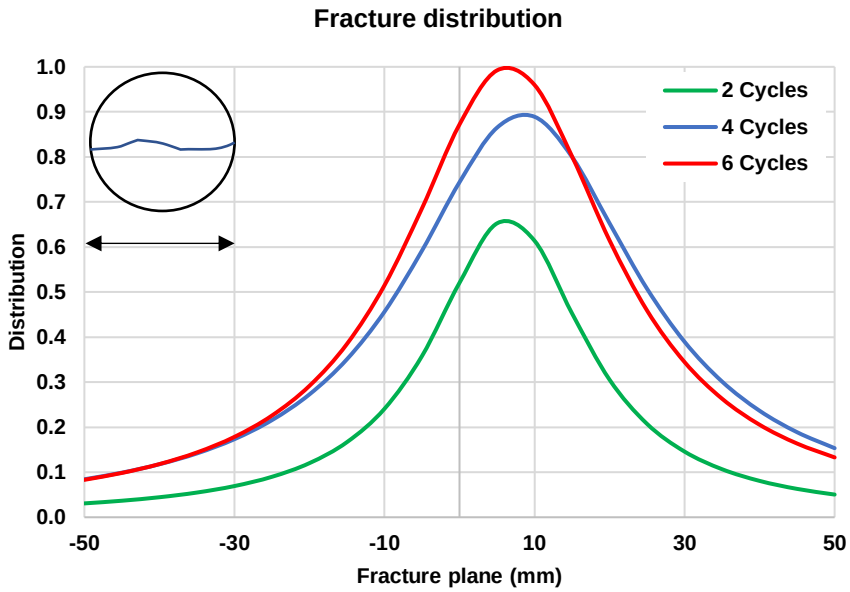


*Figure 4-36. Fracture distribution about the fracture plane in plain view for the three tests. The distribution for the 4- and 6-cycle tests almost overlap each other.*

The distributions perpendicular to the fracture plane and vertical have a similar response (***Fig. 4.37***). The 2-cycle test shows the more narrowed vertical distribution, with the smallest process zone; most events happened at 70 mm depth, which is right above the injection point. Both tests with 4 and 6 cycles have a wider vertical distribution in the center of the sample and almost identical, and their process zone is wider. The events located in the upper and lower 40 mm are few and almost nonexistent in the 2-cycle test.

Based on the events distribution and acoustic maps, the 4- and 6-cycle test have a similar process zones and fracture networks. Calculating the area under each distribution, and multiplying

the three distributions, an approximate on the SRV is obtained. The 4-cycle test had a 5.6-fold increase with respect to the 2-cycle test, while the 6-cycle test had a 7.3-fold increase.

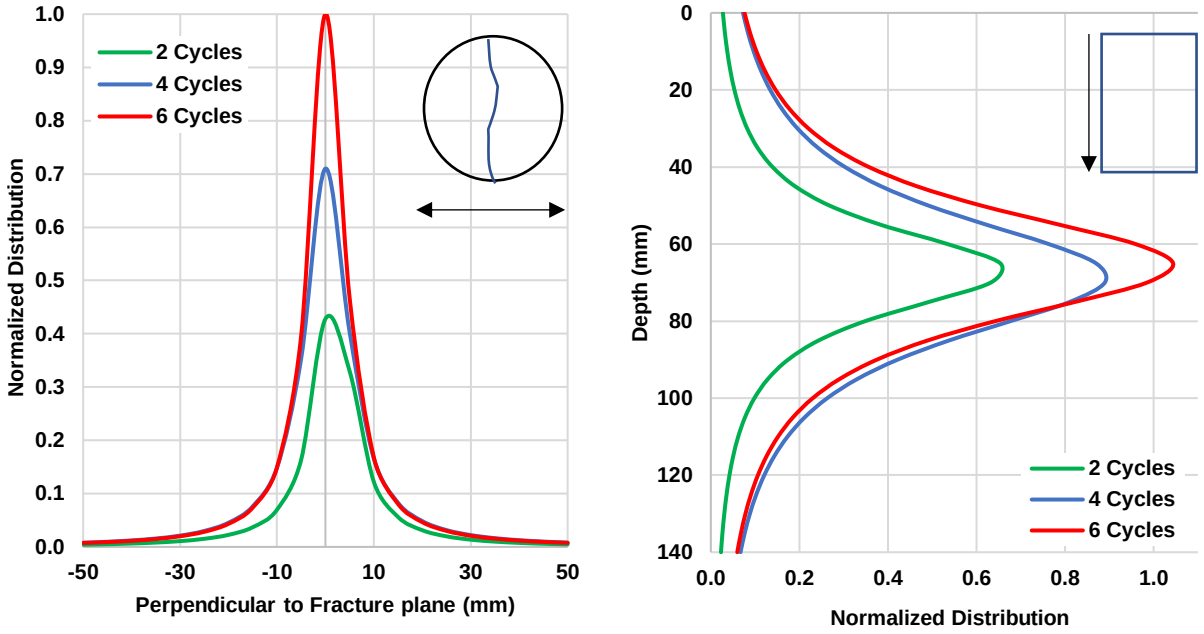


*Figure 4-37. Number of AE events in 5mm depth intervals (left) and Lorentzian distribution perpendicular to the fracture direction (left) and vertical (right). In this case, the 4- and 6-cycle test have a wider process zone (width) than the 2-cycle test. Similar response in the vertical distribution, where the 4- and 6-cycle tests almost overlap each other.*

- **Permeability**

Physical measurements were carried out to compare the influence of fracturing protocols on permeability. Permeability tests were performed on the right wing of each sample using the AP-608$^{TM}$ permeameter previously described in section 4.1.3. The native and conventional permeabilities were taken from Goyal (2020). There is a declining trend for each experiment as a function of confining pressure (***Fig. 4.38***). This is expected as higher pressure will close the fractures and pores. The greater the number of cycles, the greater the measured permeability, suggesting more damage is created as more cycles are applied to the rock. There is a two orders of magnitude difference between the cyclic experiments and the native sample, showing the significant permeability increase after fracturing. Even with 2 injection cycles, there is an

improvement with respect to the conventional monotonic test. The decline in permeability is almost parallel between each test; however, the permeability for the 2-cycle test has a shift in the trend at the highest pressure. Note that the 4-cycle experiment did not register permeability at 4000 psi, which is attributed to an error while running the experiment. The 5000 psi could be slightly overestimated.

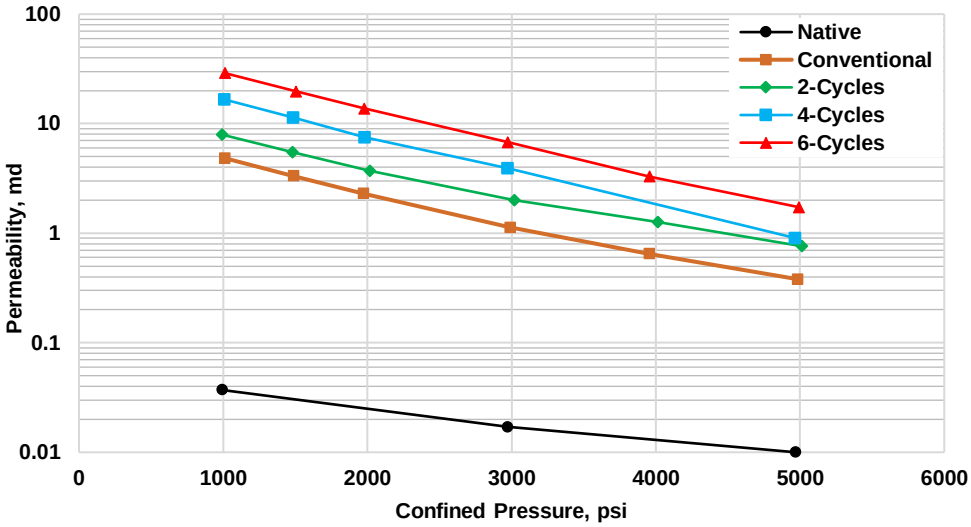


*Figure 4-38. Permeability measurements under different confining pressures. The greater number of cycles in a test, the greater the permeability increase. All the pressure dependencies are very similar.*

Walsh equation (***Eqn. 4.11***) was used for fracture permeability as a function of effective pressure (Walsh, 1981).

$$\left(\frac{k}{k_o}\right)^{\frac{1}{3}} \approx 1 - \left(\frac{\sqrt{2}h}{a_o}\right) ln\left(\frac{p}{p_o}\right)_e \quad \text{.....(4.11)}$$

The equation uses $k_o$ and $P_o$ as reference permeabilities and pressures, while k and P are the permeabilities obtained at different pressures (P); h is the root mean square roughness of the fracture surface, and $a_o$ is the half aperture of the fracture. The constant $\left(\frac{\sqrt{2}h}{a_o}\right)$ ends up as the slope between the relation of permeability with effective pressure, which is a parameter used to measure the effect of fracture as a permeability contributor (***Fig. 4.39***).

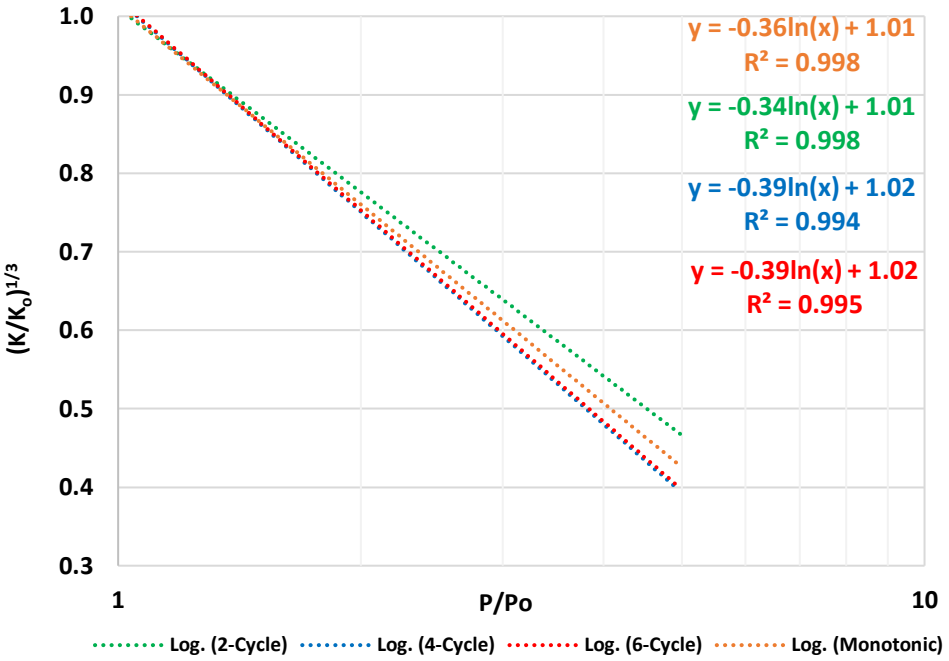


| Test | Constant $\frac{\sqrt{2}h}{a_0}$ |
|---|---|
| Monotonic | 0.36 |
| 2-Cycle | 0.34 |
| 4-Cycle | 0.39 |
| 6-Cycle | 0.39 |

*Figure 4-39. Walsh correlation for the monotonic test and the cyclic injection tests. There is an almost perfect relation between the effective permeability and the effective pressure for each of the cases. The tests executed with 4- and 6-cycle had the greatest constant $\sqrt{2}h/a_0$, suggesting those tests to have a greater contribution from the fracture in the permeability.*

The data for all the tests fits the Walsh equation, where the permeability decreases as a function of the effective pressure. The constants for the 4- and 6- cycle test are greater than the 2-cycle test, indicating that there's a greater contribution from the fracture in the measure permeability.

- **Test Efficiency**

To compare the efficiency between tests, the work generated on each test was calculated using ***Eqn. 4.12,*** where P is the peak at each pressure cycle measured in psi, and ΔV is the applied volume during each cycle in mL.

$$Work = P * \Delta V \quad \text{.....(4.12)}$$

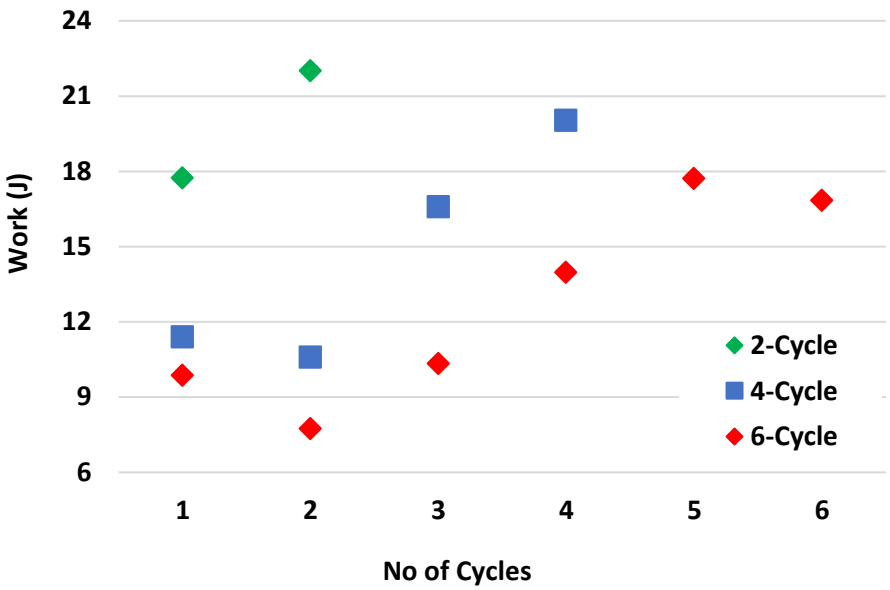


*Figure. 4-40. Work generated per cycle on each test. Note that the work used per cycle increases towards the latest cycles as higher pressure are reached with greater volumes.*

First, the work generated per cycle is displayed in ***Fig. 4.40***. The work generated increases towards the latest cycles on each test due to greater peak pressures reaching higher magnitudes. A total work inputted is calculated by adding the amount of work used under each cycle. By obtaining the ratio of total acoustic events recorded during propagation with respect to the amount of work inputted, the 4-cycle test was the most efficient under out test conditions (***Fig. 4.41***).

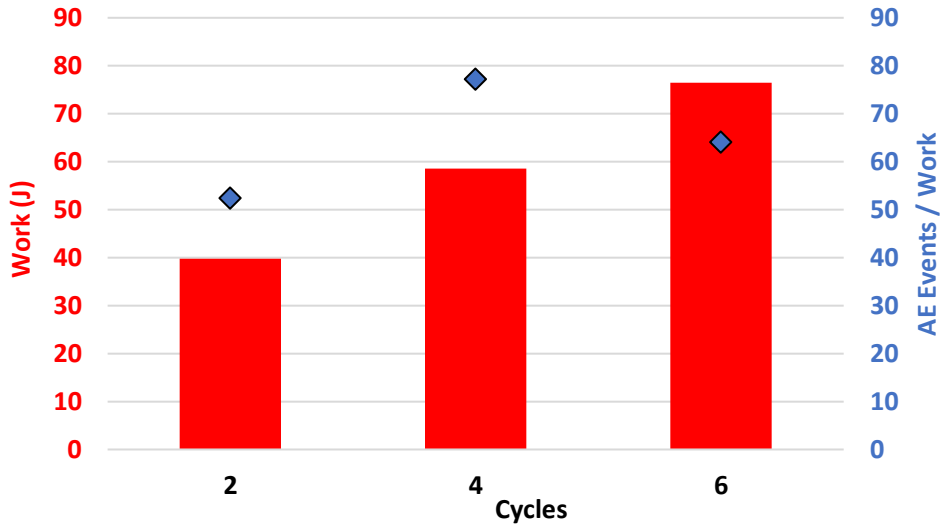


*Figure. 4-41. AE Events generated based on the total work inputted per test. The 4-cycle test was the most efficient under out test conditions, having near 80 AE Events per joule of work. The 2-cycle test showed to be the least efficient.*

- **SEM Imaging**

1-in diameter cores were cut and polished from the right fracture wing to perform SEM imaging. The 2-cycle test had a low count on the number of secondary fractures. Besides, the few secondary fractures had a small length, making them difficult to detect (***Fig. 4.42***). The 4-cycle test showed an increase in length for the secondary fractures. The largest secondary fracture measured 1.18 mm, extending parallel to the primary fracture, and connected to it in three different locations (***Fig. 4.43***). Some damage is also observed in the fracture wall. The last test had the most extended secondary fracture among the three tests, and the highest fracture count (***Fig. 4.44***). Damage was observed on both sides of the fracture wall.

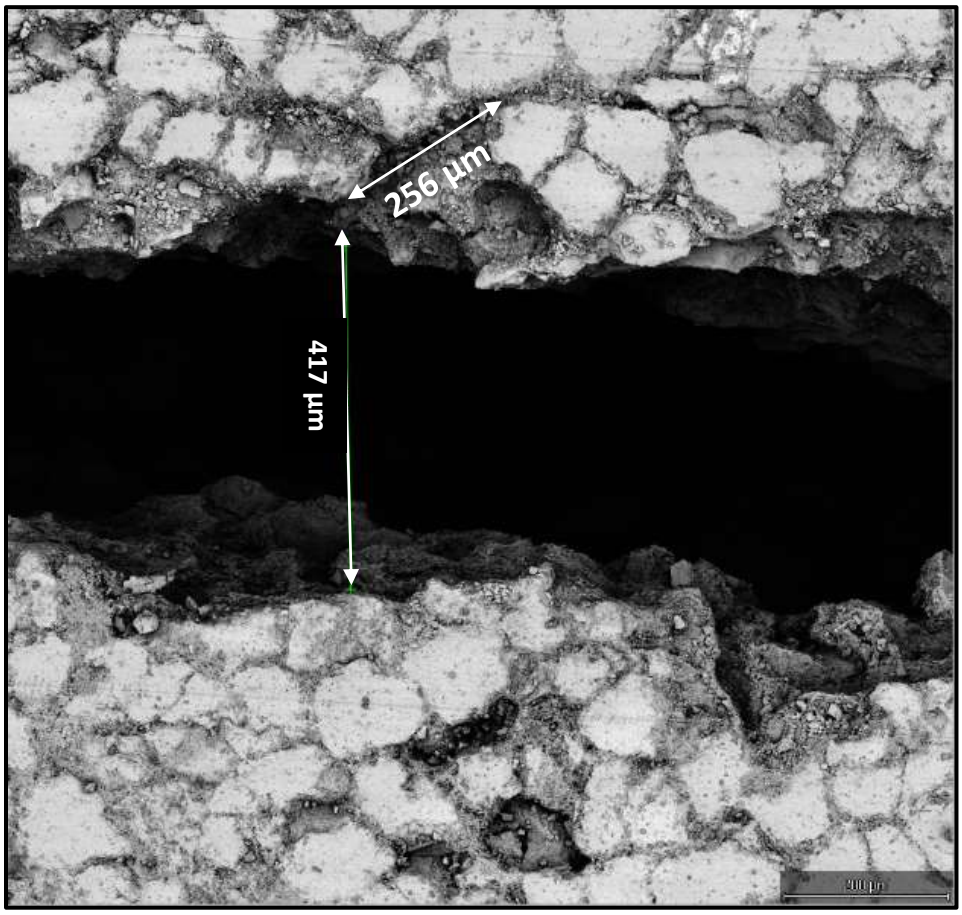


*Figure 4-42. SEM image for the 2-cycle test with a scale of 200 µm. There was a low secondary fracture count with a small length.*

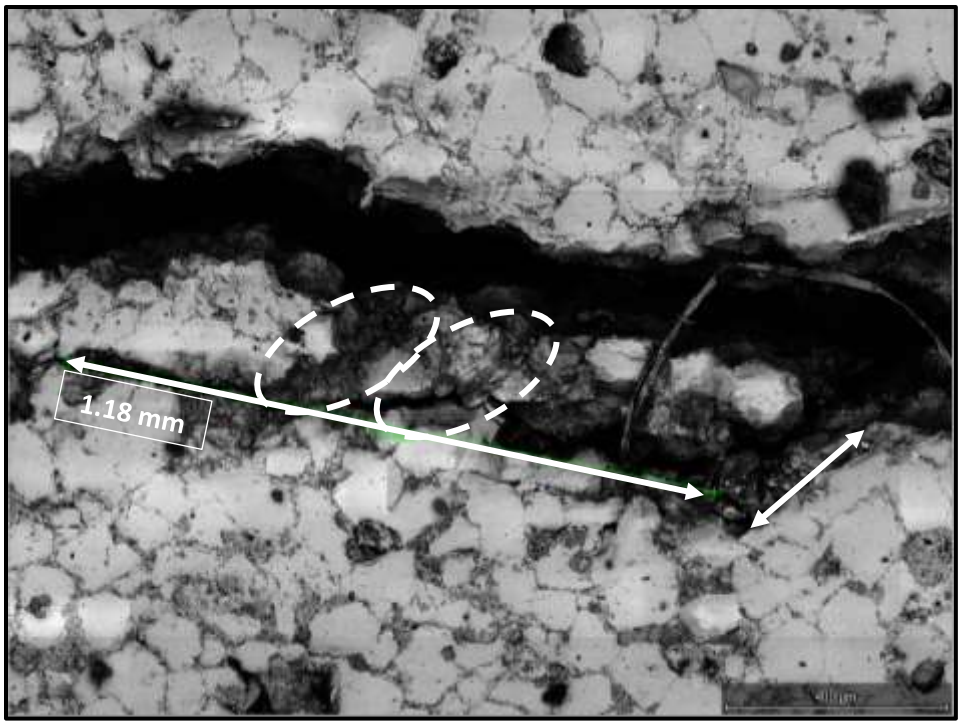


*Figure 4-43. SEM Image for the 4-cycle test with a scale of 400 µm resolution. A large secondary fracture was created connected through the primary fracture in three different zones. Overall, there was more secondary fractures that in the 2-cycle test.*

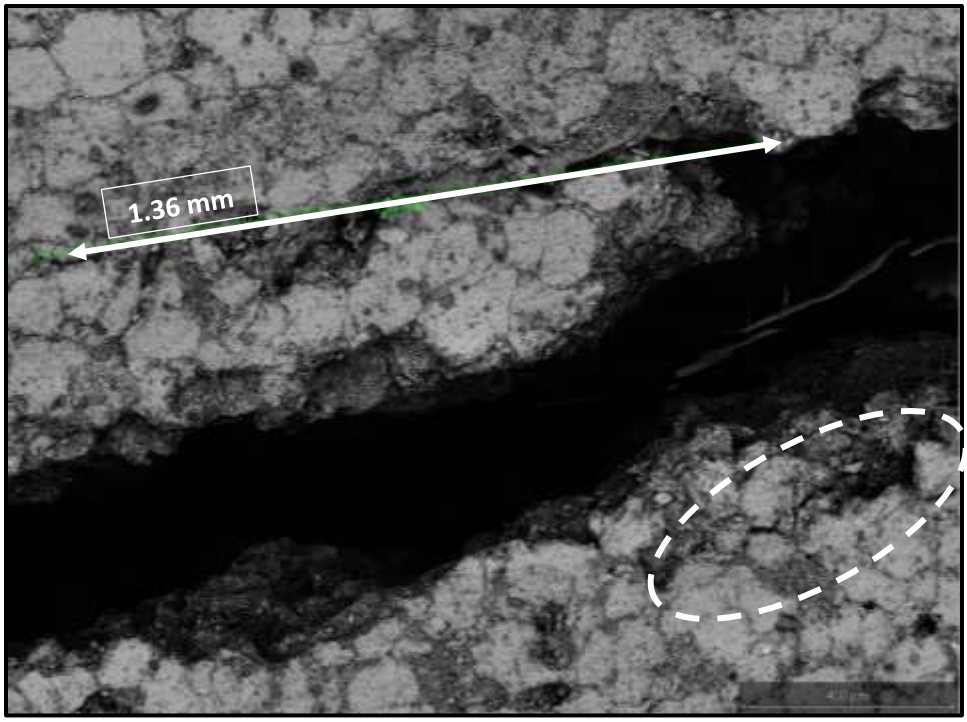


*Figure 4-44. SEM Imaging for the 6-cycle test at a resolution of 400 µm. The longest secondary fracture was observed in this test, with a total length of 1.36 mm. Both sides of the fracture wall showed secondary fractures.*

- **Acoustic emissions amplitude analysis**

The acoustic attributes, specifically amplitude, frequency, and source dimension parameters such as moment magnitude and crack radius were analyzed. The amplitude was calculated as explained in section 4.1.4 using the peak amplitude of the signal envelope. Then, an arithmetic average was taken across all the transducers that registered a clean signal.

Events before breakdown had the lowest peak amplitudes for every protocol (***Fig. 4.45a)***. Events in tests with 4- and 6-cycles had higher amplitudes than those in the 2-cycle test during this stage. The average peak amplitude during the remaining stages (propagation and closure) did not change as a function of cycles, however, it was higher than pre-breakdown.

***Fig. 4.45b*** shows the area under the frequency spectrum. The calculated area was assumed to represent the energy induced on each acoustic event and is calculated to detect energy variations for each stage. The pre-breakdown events showed the lowest energies, consistent with the peak amplitude.

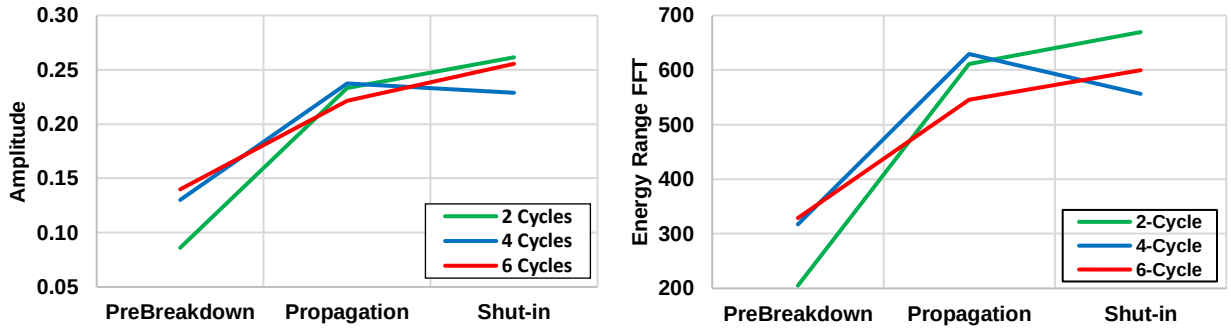


*Figure 4-45. a) Average wave signal amplitude b) average area under the signal envelope (right) The pre-breakdown phase shows the smallest amplitudes, and a reduction in amplitude is observed for higher number in cycles in a test (propagation and closure).*

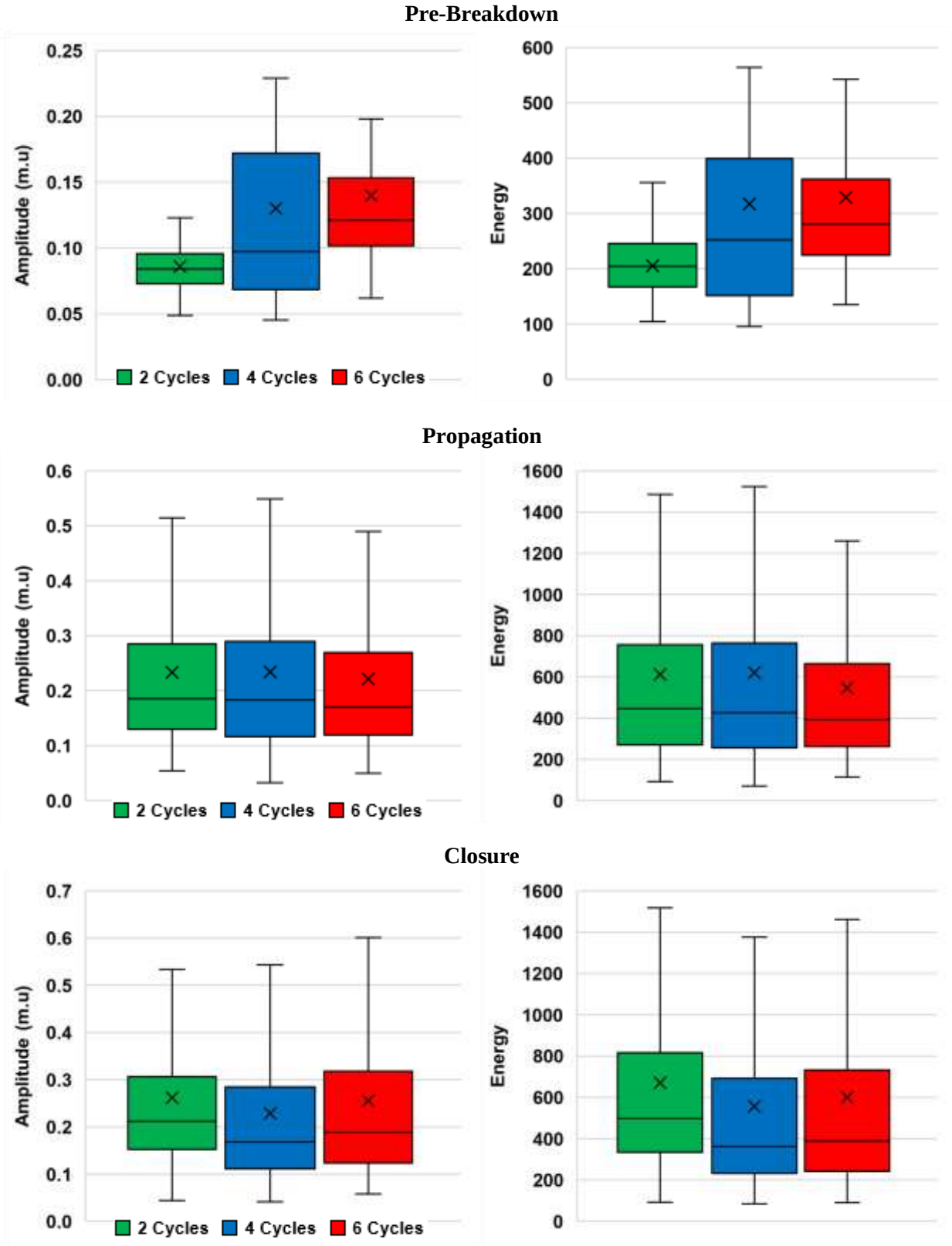


*Figure 4-46. Wave amplitude and area under the envelope for each phase. The pre-breakdown events have higher amplitudes for tests with more cycles. During propagation and closure, the signal peak amplitudes are similar among every test. The area under the envelope decreases for tests with more cycles.*

The amplitude and area were plotted for each phase (***Fig. 4.46***). During pre-breakdown, the events in the 2-cycle experiment yield the smallest amplitudes and lowest energies. The 4- and 6-cycle tests had larger amplitudes. Note that the amplitudes and energies have the same trends. Propagation and closure phases were harder to interpret as their ranges were very similar. However, during propagation, the 6-cycle test had lower amplitudes and energies than the other two tests. During closure, every test had behaved similarly.

The implications of seismicity in geothermal are significant, as lower seismicity means a reduction earthquake size. Opposite to pre-breakdown, those events induced during propagation had high amplitudes. Using cyclic loading under multiple cycles could reduce the magnitude induced earthquakes during fracture propagation (Zhuang et al., 2017).

- **Acoustic emissions classification**

Classification of acoustic events based on polarity was performed as explained in section 4.1.4. Tensile, shear, and compressive events were obtained. The classification was done based on the number of cycles per test and the event's phase occurred (pre-breakdown, propagation, or closure). Mapping of tensile and compressive events is also displayed. At least 7 clean polarity readings per event were required for classification, so those events that did not pass the threshold were not considered. Note that the events that registered frequencies near 0 kHz were not considered.

First, the total number of events was classified between tensile, compressive, and shear (***Fig. 4.47***). Every test was dominated by shear, which controlled more than 80% of events. Tensile events were the same relative to the total number of events, having between 3 to 4% per test. Compressive events significantly increased with the number of cycles.

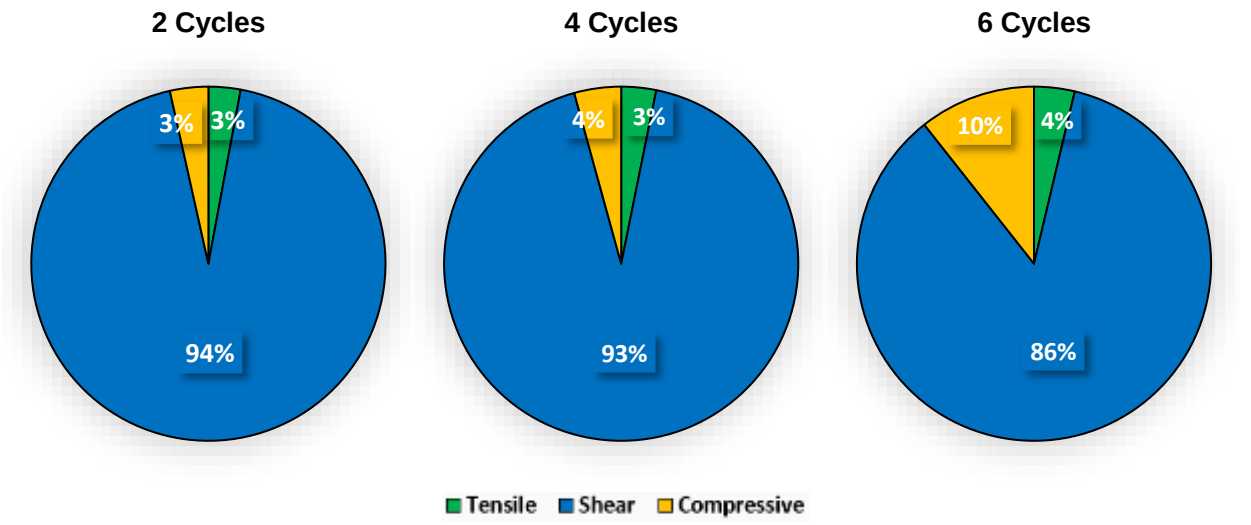


*Figure 4-47. Classification of acoustic events based on polarity. The higher number of injection cycles induce a higher percentage of tensile events, while compressive events are more consistent. Shear is the dominant failure mechanism.*

The damage by tensile and compressive events was also accounted for per phase. It is noted that most of the events correspond to shear failure, consistent with previous laboratory experiments (Damani et al., 2013; Warpinski et al., 2012). ***Fig. 4.48*** shows tensile events mainly occurred during the propagation phase. This suggests that tensile events are contributing to fracture opening. Note that the 6-cycle test showed the greatest number of tensile events during propagation, suggesting that a larger number of cycles induces more tensile events. The closure phase showed a little record of tensile events, mainly dominated by shear.

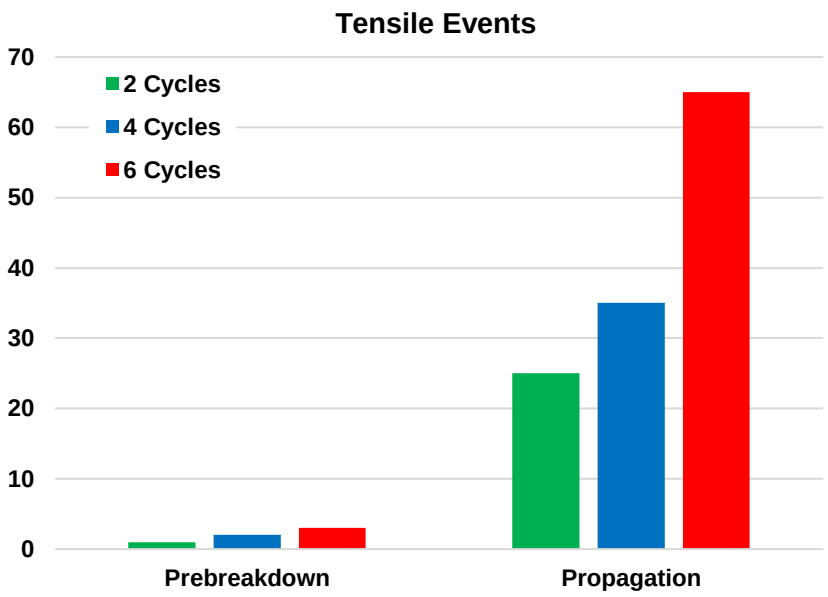


*Figure 4-48. Tensile events recorded for each test in each phase. They mainly occurred during the propagation phase, suggesting fracture opening is the main mechanism for tensile failure. Note that the 6-cycle test induces the largest number of events, which means that greater number of cycles causes more tensile events.*

In terms of compressive events, propagation was the phase where most of the compressive events were recorded (***Fig. 4.49***). In this scenario, we also observed many events during the closure phase. Note that the 6-cycle test has a drastic increase in compressive events.

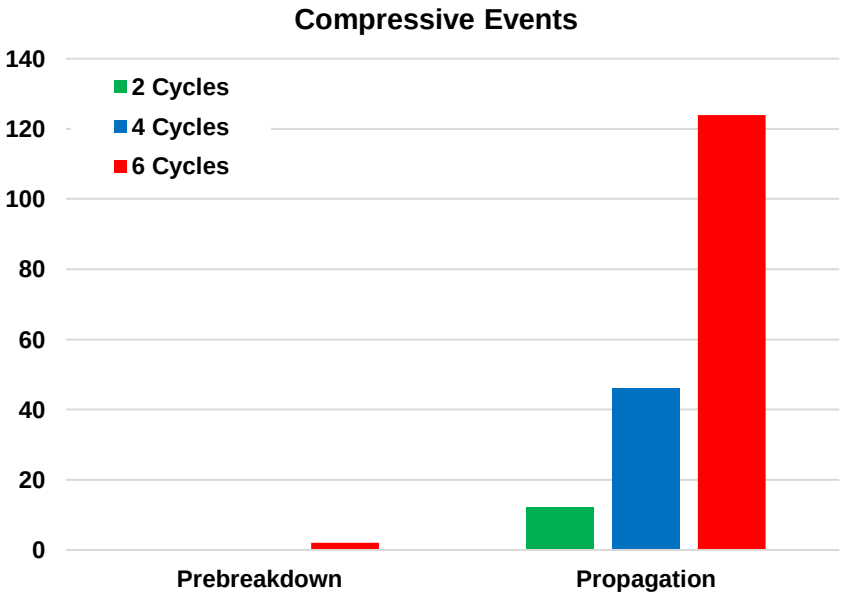


*Figure 4-49. Compressive events recorded for each test in each phase. The greater number of cycles induces a larger number of compressive events.*

Tensile and compressive events were mapped individually to capture their location with respect to the primary fracture (***Fig. 4.50***). The compressive events had a distribution through the main fracture. In the 2-cycle test, tensile events mostly locate near the wellbore. For the test with 4 cycles, some events are slightly distant from the main fracture towards the left. The 6-cycle test is the best in recreating the fracture plane. Tensile failure events tend to be associated with mode I fracture opening. Tests with 2 and 4 cycles hardly recreate the fracture plane but instead are more scattered. In the test with 6 cycles, tensile events fall along the primary fracture, most occurring near the wellbore area. Both compressive and tensile events can describe the primary fracture in the 6-cycle test.

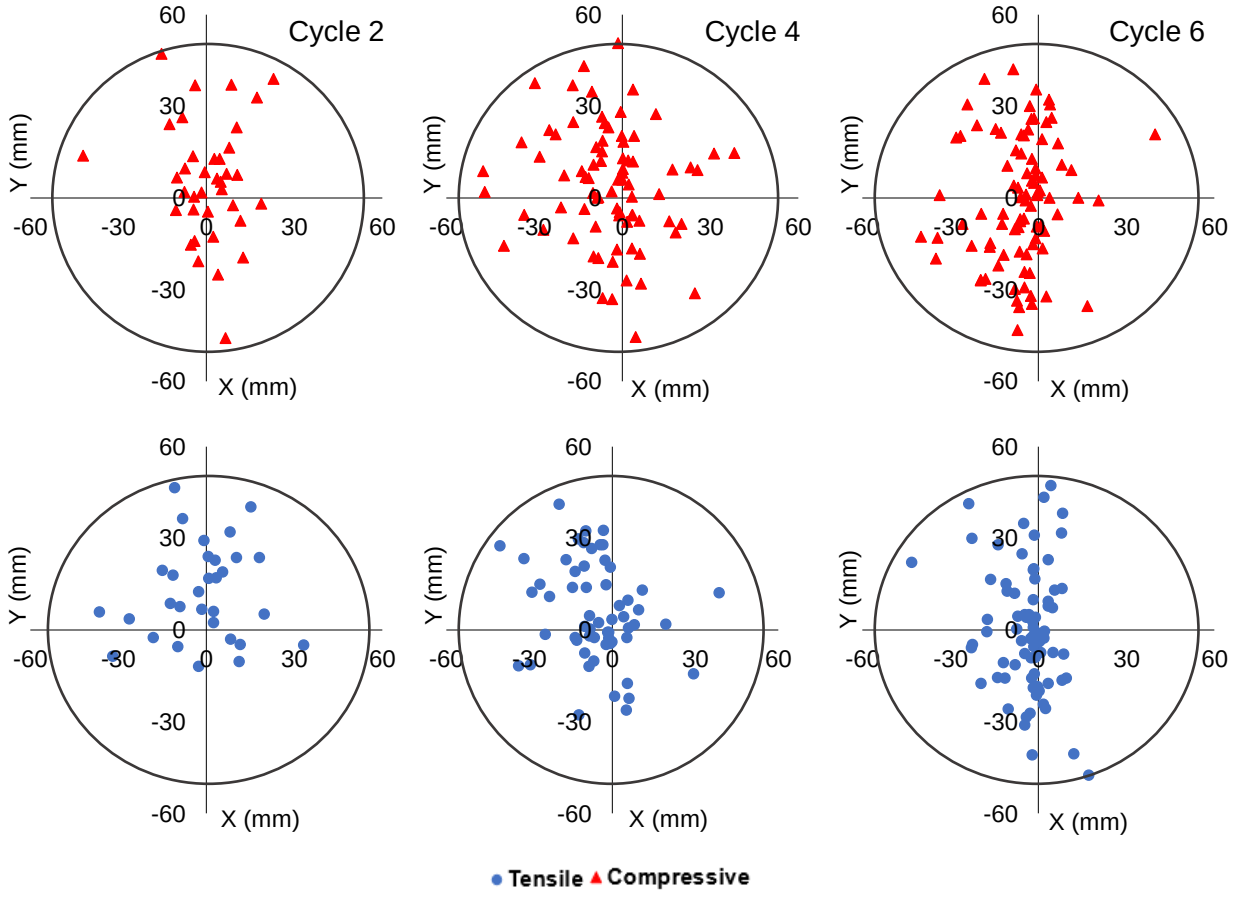


*Figure 4-50. Acoustic maps of tensile and compressive events from the top view. The compressive events are distributed along the fracture and are closely represent the primary fracture in the 4- and 6-cycle. Tensile events are more dispersed, and only represent the primary fracture in the 6-cycle test.*

- **Acoustic emission source dimensionality**

The last part of this study analyzes the moment magnitudes, source radius, event displacement on the fracture plane, and stress drop. The methodology is explained in section 4.1.4 will be used. The input mechanical properties are presented in ***Table 4.3***.

*Table 4-3. Tennessee Sandstone input parameters for source mechanisms calculations.*

| Parameter | Symbol | Value | Units |
|---|---|---|---|
| Bulk density | ρ | 2700 | Kg/m3 |
| Shear wave velocity | Vs | 2600 | m/s |
| Compressional wave velocity | Vp | 4335 | m/s |
| Shear modulus | G | 18 | GPa |
| Bulk modulus | K | 26 | GPa |
| Young's modulus | E | 45 | GPa |
| Poisson's ratio | v | 0.22 | |

The seismic moment is used as a method to measure the magnitude of each earthquake. In this case, two main observations are obtained (***Fig. 4.51***). First, the moment magnitude decreases as more cycles are used pre-fracturing, which is important as field studies have shown how higher seismic moments are more prone to induce larger earthquakes. Second, those events before failure have the lowest moments, while propagation have similar moments, agreeing with observations on waveform amplitudes. Seismic moment is a parameter that needs more attention in geothermal fracturing, where seismicity is one of the main issues.

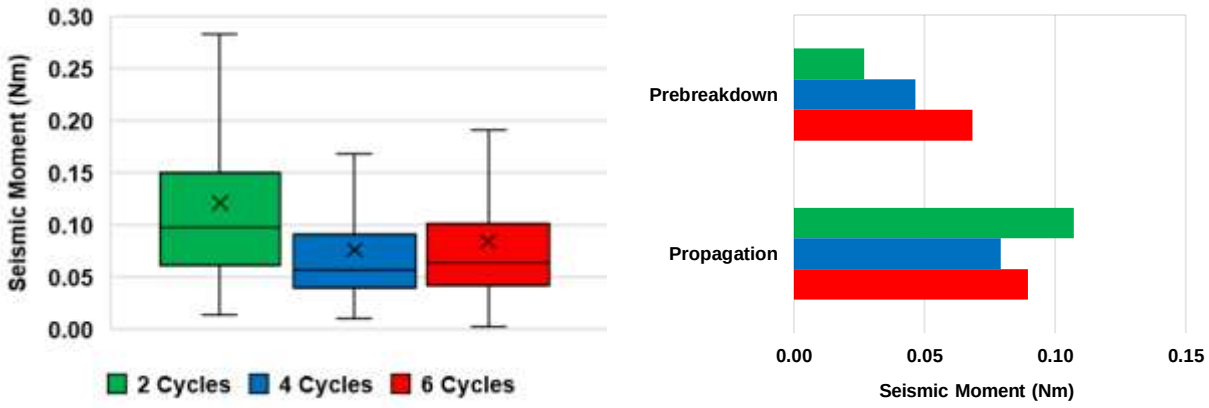


*Figure 4-51. Average seismic moment for each test separated by phases. The seismic moment is low during AE events in pre-breakdown and increases during post-breakdown. The 4-cycle test is the optimal based on the events' magnitude.*

The source radius is directly proportional to the seismic moment (***Fig. 4.52***). In a semilog plot, both parameters have a weak correlation. The source radius range oscillates from 5 to 15 mm. The events in the 6 cycles test have the smallest in source radius. Note that some of the events for the 6-cycle test show a significantly lower seismic moment which should be further analyzed as they are off trend.

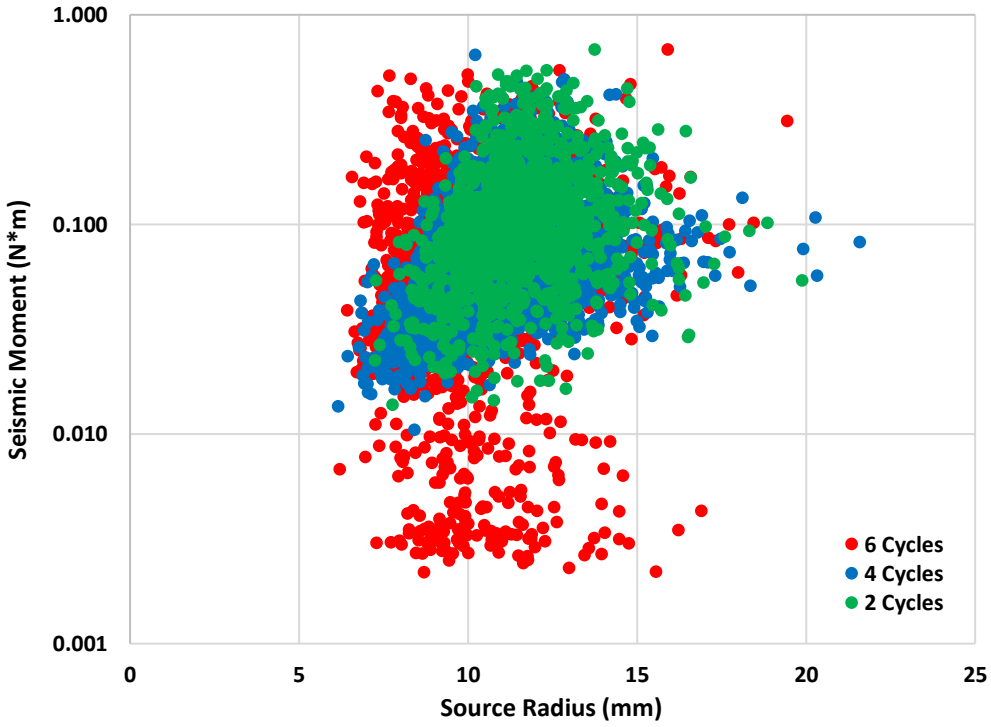


*Figure 4-52. Seismic moment versus source radius. There is a direct correlation, the greater the source radius, the greater the seismic moment. Note the 6-cycle have events in a lower range of moment compared to the other tests.*

### *4.3.3 Discussion*

In this study, pre-cyclic injection was performed on 2.5% KCl saturated Tennessee sandstone of 175 µm grain size, using different number of cycles before breakdown (2, 4, and 6).

- The breakdown pressure decreased as the number of cycles increased, with 10, 15, and 22% difference for the 2-, 4-, and 6-cycle tests with respect to the monotonic test.

- The 4- and 6-cycle tests created a larger SRV than the 2-cycle test. There was a 5.6- and 7.3-fold increase, respectively.
- The average event seismic moments decreased as the number of cycles increased. This is important as larger moments are associated with large earthquakes. With recent developments in geothermal energy, hydraulic fracturing with cyclic injection could reduce the magnitude of associated microseismics, reducing the number of induced earthquakes.
- There is an increase in permeability with increasing number of injection cycles. The 6-cycle test had twice the permeability compared to the 2-cycle test under 5000 psi of confining pressure.
- Shear failure controlled the deformation of the samples. Tensile events increased as more cycles were used.
- **Our experiments suggest that the 4-cycles test is optimal under our testing conditions.**

# 5. APPLICABILITY AND FUTURE WORK

This section is divided in three parts. First, some of the applications of the tests used in this study are described. Second, a hydraulic fracturing test using cyclic injection is designed for field use. Last, recommendations for future studies are noted.

## 5.1. Applications

1. Formations requiring high breakdown pressure require more energy and horsepower. Thus, reducing breakdown pressure through cyclic injection is a potential cost savings for field operations. This will be applicable to deeper formations as well as formations with rocks such as granite/gabbro and other igneous rocks which are encountered in geothermal wells and have higher breakdown pressure.

2. Field experiments have shown that the hydrocarbon recovery increases with the amount of surface area of the fractures created during hydraulic fracturing. Complex fracture networks are needed for larger surface area. Our cyclic injection technique showed greater AE events, and thus more complex fracture network, as compared to monotonic injection. Cyclic injection than will be more appropriate technique for greater hydrocarbon recovery. This technique can also be useful for Enhanced Oil Recovery in shales, which depends on the total surface contacted area.

3. Geothermal operations require fluid injection in the reservoir, which can reactivate fractures by increasing pore pressure. Increased pore pressure can result in inducing seismicity. As such, the use of event's classification between tensile and shear through frequencies could aid to understand the type of events created. If the events are shear, pumping of fluid can be stopped in order to prevent/minimize induced seismicity. Note that cyclic injection while creating complex fracture network was shown to decrease the magnitude in the induced microseismic events.

4. Nanoindentation is a technique used to measure mechanical properties on any unconventional formations with fine grain size. With subsurface carbon sequestration gaining popularity and the advent of hydrogen storage in shales, nanoindentation can be a technique that evaluates the effect of those gases in the elastic and non-elastic mechanical properties.

## 5.2. Hydraulic Fracturing Design

A design was created for operators to apply pre-cyclic injection in the lab. The first step for the user is to input an approximate magnitude of the breakdown pressure for monotonic injection. Then, the starting pressure for the first cycle is calculated using ***Eqn. 5.1***. Here, the total number of cycles and the percentage desired for reduction per cycle are necessary. (i.e., assume that breakdown pressure for monotonic injection is 1000 psi; if aiming for 3 cycles and wanting a reduction of 10% per the desired cycle, the starting pressure for the first cycle will be set to 700 psi, 30% lower than your monotonic breakdown.)

$$P_{Cycle\,1} = P_{b-monotonic} - [\#\ of\ Cycles * (Reduction\ \% * P_{b-monotonic})] \quad (5.1)$$

Once the initial pressure is calculated, the remaining peak cycles are obtained. Eqn. 5.2 is used, where the resulting starting pressure ($P_{cycle1}$), the total number of cycles, and the specified cycle number are inputted.

$$Peak\ Cycle = P_{cycle\,1} + \frac{(Cycle\ N_o - 1) * (P_{b-monotonic} - P_{cycle\,1})}{\#\ of\ Cycles} \quad (5.2)$$

A screenshot of the created spreadsheet is displayed in ***Fig. 5.1***. Note that the yellow cells correspond to the input parameters. The spreadsheet gives the user the design that should be used for any number of cycles selected from 2 to 10. If one specific number of cycles is desired, it is inputted in the pink cell. With this, the user will know how to set up the protocol based on the number of cycles that he wants to use. A baseline of 500 psi is recommended so that operators do

not have to shut the pump completely but instead can have a base pressure as a lower limit to drop.

This design aims to have a method to compare different test efficiently.

| Parameter | Magnitude |
|---|---|
| Monotonic Injection Breakdown | 7000 |
| Percentage reduction | 10% |
| Number of Cycles | 6 |
| Starting pressure | 2800 |

$$P_{Cycle\ 1} = P_{b-monotonic} - [\#\ of\ Cycles * (Reduction\ \% * P_{b-monotonic})]$$

$$Peak\ Cycle = P_{cycle\ 1} + \frac{(Cycle\ N_o - 1) * (P_{b-monotonic} - P_{cycle\ 1})}{\#\ of\ Cycles}$$

| | | Cycle Pressure peak | | | | | | | | | |
|---|---|---|---|---|---|---|---|---|---|---|---|
| **Pb =** 7000 | | 1 | 2 | 3 | 4 | 5 | 6 | 7 | 8 | 9 | 10 |
| Number of Cycles per test | 2 | 5600 | To failure | | | | | | | | |
| | 3 | 4900 | 5600 | To failure | | | | | | | |
| | 4 | 4200 | 4900 | 5600 | To failure | | | | | | |
| | 5 | 3500 | 4200 | 4900 | 5600 | To failure | | | | | |
| | 6 | 2800 | 3500 | 4200 | 4900 | 5600 | To failure | | | | |
| | 7 | 2100 | 2800 | 3500 | 4200 | 4900 | 5600 | To failure | | | |
| | 8 | 1400 | 2100 | 2800 | 3500 | 4200 | 4900 | 5600 | To failure | | |
| | 9 | 700 | 1400 | 2100 | 2800 | 3500 | 4200 | 4900 | 5600 | To failure | |
| | 10 | 0 | 700 | 1400 | 2100 | 2800 | 3500 | 4200 | 4900 | 5600 | To failure |

| | | Cycle Pressure peak | | | | | | | | | |
|---|---|---|---|---|---|---|---|---|---|---|---|
| | | **1** | **2** | **3** | **4** | **5** | **6** | **7** | **8** | **9** | **10** |
| Number of Cycles per test | 6 | 2800 | 3500 | 4200 | 4900 | 5600 | 6300 | | | | |

*Figure. 5-1. Spreadsheet for the developed hydraulic fracturing design. The input parameters correspond to the monotonic injection breakdown pressure and the percentage reduction desired based on the number of cycles. Note that between C10:L17 are the values of the pressures to use as peak based on the number of cycles. The part between rows 19 and 21 just shows a specific column based on the number of cycles inputted. The formulas are also displayed for reference.*

## 5.3. Future Work Recommendations

First, I suggest repeating the cycle test using the design described in section 5.2. That will use similar peak pressures but change the initial starting pressure according to the number of cycles desired. I will recommend starting with a test using the monotonic breakdown pressure, then testing 3, 5, and 7 cycles.

Second, based on the tests performed in the first recommendation, an optimal number of cycles can be obtained. I would use that number of cycles and perform at least 3 cyclic injection tests with changes in differential pressures. If treating different differential pressures, operators would relate it better to stresses in the field. Confining pressure can be increased as it has been set to only 500 psi.

Third, I would suggest using the continuous monitoring system for any test. If this gives us the moment type, it can be compared to the measured frequencies, having a broader understanding of the waveforms recorded at each stage during the fracturing tests.

Forth, I would consider different fracturing fluids. Based on the laboratory experiments performed so far, no test has used fluids at high temperatures, but every fluid has been injected at room temperature. I would compare the signal waveforms obtained to those at standard conditions, as the wavelength, the frequency, and the moment magnitudes generated.

In nanoindentation, I would suggest performing indentation tests on rocks used to store $CO_2$. I would grab rocks with known petrophysics (from different formations) and obtain elastic parameters' change. It would be important to evaluate the elastic change under different times of $CO_2$ storage, as this is a long-time process. Consider also that the nanoindentation can flow gases while testing. This might help in the test design.

# 6. CONCLUSIONS

Each chapter has described its own set of conclusions in the discussion section. Here, a summary of the main findings is presented.

- The number of cycles used in pre-cyclic injection relates to the stimulated reservoir volume, breakdown pressure, and induced seismicity.

  - ❖ Based on the testing conditions, a greater number of cycles reduces the monotonic breakdown pressure. As the number of cycles increased, there was a reduction of 10, 15, and 22% difference for the 2-, 4-, and 6-cycle test, with respect to the monotonic test. Breakdown pressure reduction is significant in fields such as geothermal, where operations occur at deeper conditions which require more work.

  - ❖ A greater number of cycles led to more located acoustic events. This was reflected in a greater estimated SRV. Compared to the 2-cycle test, there was a 5.6- and 7.3-fold increase in the 4-cycle and 6-cycle tests, respectively.

  - ❖ The average event seismic moments decreased as the number of cycles increased. This is important as larger moments are associated with large earthquakes. This can be applied in geothermal operations where fluid is injected in the reservoir, which reactivate fractures by increasing pore pressure, inducing seismicity.

  - ❖ The 4-cycle test was the most efficient test, with the greatest SRV generated based on the work inputted.

- Nanoindentation is shown as a successful technique to understand the mechanical behavior of unconventional reservoirs under different conditions.

  - ❖ Linear gel generates more damage than slickwater to elastic properties. The Young's modulus had a greater reduction in carbonate-rich formations attributed to carbonate dissolution. Most of the elastic reduction occurred within the first 5 hours of saturation, which should be considered in field testing.

  - ❖ Nanoindentation was a successful technique to measure mechanical properties in ash beds, as those were not previously reported. The Young's modulus was significantly lower than the formation matrix, leading to fracture closure. Additionally, it was observed that this layer could creep substantially more, which could cause proppant embedment.

  - ❖ Primary and secondary creep can be modeled through nanoindentation using the holding time. Using the secondary creep function, it was observed that creep mainly depends on clays and TOC. Furthermore, creep deformation increased for saturated samples.

# 7. REFERENCES


1. Adams, J., and Rowe, C. (2013). Differentiating applications of hydraulic fracturing. In *ISRM International Conference for Effective and Sustainable Hydraulic Fracturing*.
2. Albright, James N., and Christopher F. Pearson. "Acoustic Emissions as a Tool for Hydraulic Fracture Location: Experience at the Fenton Hill Hot Dry Rock Site." *SPE J.* 22 (1982): 523–530.
3. Agarwal, K., Mayerhofer, M. J., and Warpinski, N. R. (2012). Impact of geomechanics on microseismicity. In: SPE/EAGE European Unconventional Resources Conference and Exhibition, Vienna, Austria. SPE-152835
4. Aki, K., and Richards, P. G. (1980). Quantitative seismology: Theory and Methods, Vols I and II, W. H. Freeman and Company, New York
5. Akrad, O. M., Miskimins, J. L. and Prasad, M., 2011, The Effects of Fracturing Fluids on Shale Rock Mechanical Properties and Proppant Embedment. *SPE Annual Technical Conference and Exhibition*.
6. Aksu, I., Bazilevskaya, E., and Karpyn, Z., 2015, Swelling of clay minerals in unconsolidated porous media and its impact on permeability. Geo. Res. J, 7, 1-13.
7. Al-Bazali, T. (2013). The impact of water content and ionic diffusion on the uniaxial compressive strength of shale. Egyptian Journal of Petroleum, 22(2), 249-260.
8. Almasoodi, M. M., Abousleiman, Y. N., and Hoang, S. K., 2014, Viscoelastic Creep of Eagle Ford Shale: Investigating Fluid-Shale Interaction. SPE/CSUR Unconventional Resources Conference – Canada.
9. Al-Nakhli, A., BaTaweel, M., Mustafa, A., Tariq, Z., Mahmoud, M., and Abdulrahim, A. (2019). Novel Methodology to Reduce the Strength of High Stress-Tight Gas Reservoirs Using Thermochemical. In *53rd US Rock Mechanics/Geomechanics Symposium*.
10. Al-Mohammed, A.M., Nasr-El-Din, H.A., and Al-Fuwaires, O.A., 2007, Degradation of high pH borate gels. Presented at the International Petroleum Technology Conference, Dubai, United Arab Emirates. IPTC 11585
11. Baig, A. (2014). Hydraulic fracturing-induced seismicity: an overview of recent observations and implications on development. *first break*, *32*(7).

12. Bak, K. M., Kalaichelvan, K., and Arumugam, V. (2014). A novel approach for classification of failure modes in single lap joints using acoustic emission data. Journal of Composite Materials, 48(24), 3003-3017.

13. Bakker, R. R., Fazio, M., Benson, P. M., Hess, K. U., and Dingwell, D. B. (2016). The propagation and seismicity of dyke injection, new experimental evidence. *Geophysical Research Letters*, *43*(5), 1876-1883.

14. Ballard, B. D., 2007, Quantitative Mineralogy of Reservoir Rocks Using Fourier Transform Infrared Spectroscopy, Society of Petroleum Engineers.

15. Brune, J. N. (1970). Tectonic stress and the spectra of seismic shear waves from earthquakes. Journal of geophysical research, 75(26), 4997-5009.

16. Burlini, L., Vinciguerra, S., Di Toro, G., De Natale, G., Meredith, P., and Burg, J. P. (2007). Seismicity preceding volcanic eruptions: New experimental insights. *Geology*, *35*(2), 183-186.

17. Calvin, C., Diaz, H. G., Mosse, L., Miller, C., and Fisher, K. (2015). Evaluating the diagenetic alteration and structural integrity of volcanic ash beds within the Eagle Ford shale. In: *SPE/CSUR Unconventional Resources Conference*. Society of Petroleum Engineers

18. Ciezobka, J., Maity, D., and Salehi, I. (2016). Variable pump rate fracturing leads to improved production in the Marcellus Shale. In: SPE Hydraulic Fracturing Technology Conference, The Woodlands, TX. SPE-179107

19. Chen, X., Eichhubl, P., Olson, J. E., and Dewers, T., 2019, Effect of water on fracture mechanical properties of shales. *Journal of Geophysical Research: Solid Earth*, **124**, 2428– 2444.

20. Chitrala, Y., Moreno, C., Sondergeld, C. H., and Rai, C. S. (2013). An experimental investigation into hydraulic fracture propagation under different applied stresses in tight sands using acoustic emissions. Journal of Petroleum Science and Engineering, 108, 151-161.

21. Clark, J. J. B. (1961). *U.S. Patent No. 2,978,025*. Washington, DC: U.S. Patent and Trademark Office.

22. Colback, P. S. B. and Wiid, B. L., 1965, The influence of moisture content on the compressive strength of rocks, in Proc. 3rd Canadian Symp. on Rock Mechanics, 65-73.

23. Corapcioglu, H., Miskimins, J. and Prasad, M., 2014, Fracturing Fluid Effects on Youngs Modulus and Embedment in the Niobrara Formation. *SPE Annual Technical Conference and Exhibition*.

24. Curtis, M. E., Cardott, B. J., Sondergeld, C. H., and Rai, C. S. (2012a). Development of organic porosity in the Woodford Shale with increasing thermal maturity. In: *International Journal of Coal Geology*, *103*, 26-31

25. Curtis, M. E., Sondergeld, C. H., Ambrose, R. J., and Rai, C. S., (2012b) Microstructural investigation of gas shales in two- and three-dimensions using nanometer-scale resolution imaging, *AAPG Bull*., 96,4,665-677.

26. Damani, A. (2013), *Acoustic Mapping and Fractography of Laboratory Induced Hydraulic Fractures.* M.S. thesis, University of Oklahoma.

27. Damani, A., Sondergeld, C. H., and Rai, C. S. (2018). Experimental investigation of in situ and injection fluid effect on hydraulic fracture mechanism using acoustic emission in Tennessee sandstone. Journal of Petroleum Science and Engineering, 171, 315-324.

28. Dean, J., Bradbury, A., Smith, G.A., and Clyne, T.W., 2013, A procedure for extracting primary and secondary creep parameters from nanoindentation data. Elsevier, Mechanics of Materials 65 (2013) 124-134.

29. Deichmann, N., and Giardini, D. (2009), Earthquake induced by the stimulation of an enhanced geothermal system below Basel (Switzerland). Seism. Res. Lett., 80, 5,

30. Engelder, T. (1999). Transitional–tensile fracture propagation: a status report. Journal of Structural Geology, 21(8-9), 1049-1055.

31. Erarslan, N., and Williams, D. J. (2012). Investigating the effect of cyclic loading on the indirect tensile strength of rocks. *Rock mechanics and rock engineering*, *45*(3), 327-340.

32. Falser, S., Mo, W., Weng, D., Fu, H., Lu, Y., Ding, Y., and Wong, S. W. (2016). Reducing breakdown pressure and fracture tortuosity by in-plane perforations and cyclic pressure ramping. In: The 50th US Rock Mechanics/ Geomechanics Symposium, Houston, June 26-29. ARMA paper 2016-191.

33. Faulkner, D. R., Mitchell, T. M., Jensen, E., and Cembrano, J. (2011). Scaling of fault damage zones with displacement and the implications for fault growth processes, J. Geophys. Res., 116, B05403.

34. Goodfellow, S. D., Nasseri, M. H. B., Maxwell, S. C., and Young, R. P. (2015). Hydraulic fracture energy budget: Insights from the laboratory. *Geophysical Research Letters*, *42*(9), 3179-3187.

35. Goyal, S., Curtis, M. E., Sondergeld, C. H., and Rai, C. S. (2020). A Comparative Study of Monotonic and Cyclic Injection Hydraulic Fracturing in Saturated Tight Rocks Under Triaxial Stress. In *Unconventional Resources Technology Conference, 20–22 July 2020* (pp. 776-792).

36. Gross, S. P., Fineberg, J., Marder, M., McCormick, W. D., and Swinney, H. L. (1993). Acoustic emissions from rapidly moving cracks. Physical Review Letters, 71(19), 3162.

37. Gupta, I., Rai, C., and Sondergeld, C., 2018, Applications of Nanoindentation for Reservoir Characterization in Shales, Paper ARM-2018-271, Proceedings, 52nd U.S. Rock Mechanics/Geomechanics Symposium, Seattle, Washington, USA, 17-20

38. Harrison, A. L., Jew, A. D., Dustin, M. K., Thomas, D. L., Joe-Wong, C. M., Bargar, J. R., and Maher, K. (2017). Element release and reaction-induced porosity alteration during shale-hydraulic fracturing fluid interactions. *Applied Geochemistry*, *82*, 47-62.

39. Hofmann, H., Zimmermann, G., Zang, A., and Min, K. B. (2018). Cyclic soft stimulation (CSS): a new fluid injection protocol and traffic light system to mitigate seismic risks of hydraulic stimulation treatments. *Geothermal Energy*, *6*(1), 1-33.

40. Hol, S., and Zoback M. D., 2013, Creep behavior of coal and shale related to adsorption of reservoir fluids. In: 47th U.S. Rock Mechanics/ Geomechanics Symposium. American Rock Mechanics Association, San Francisco.

41. Hunt, J. M., Wisherd, M. P., and Bonham, L. C. (1950). Infrared Absorption Spectra of Minerals and Other Inorganic Compounds. *Analytical Chemistry*, *22*(12), 1478–1497.

42. Iriarte, J., Merritt, J., and Kreyche, B. (2017). Using water hammer characteristics as a fracture treatment diagnostic. In *SPE Oklahoma City Oil and Gas Symposium*.

43. Jarvie, D. M. 1991. Total Organic Carbon (TOC) Analysis, in Merrill, R. K., ed., Treatise of Petroleum Geology: Handbook of Petroleum Geology, Source and Migration Processes and Evaluation Techniques. American Association of Petroleum Geologists, P. 113-118.

44. Jones, S.C. 1971. A rapid accurate unsteady-state Klinkenberg permeameter, SPE 3535, first presented at the SPE 46th Annual Fall Meeting, New Orleans.

45. Kim, J. W., Bhowmick, S., Hermann, I., and Lawn, B. R. (2006). Transverse fracture of brittle bilayers: Relevance to failure of all-ceramic dental crowns. *Journal of Biomedical Materials Research Part B: Applied Biomaterials*, *79*(1), 58-65.

46. Kumar, D. (2013). Applying Backus averaging for deriving seismic anisotropy of a long-wavelength equivalent medium from well-log data. *Journal of Geophysics and Engineering*, *10*(5), 055001.

47. Kumar, A., Kumar, A., Mittal, H., Kumar, A., and Bhardwaj, R. (2012). Software to estimate earthquake spectral and source parameters. International Journal of Geosciences 3 (5), 1142-1149.

48. Hulse, D.S., 1959. Fracturing Process with Superimposed Cyclic Pressure. U.S. Patent US2915122.

49. Li, Y. and Ghassemi, A., 2012. Creep Behavior of Barnett, Haynesville, and Marcellus Shale. Proc., In the 46th US Rock Mechanics / Geomechanics Symposium held in Chicago, IL, USA, 24-27 June 2012.

50. Liu, M., Lu, C., Tieu, K. A., Peng, C. T., and Kong, C. (2015). A combined experimental-numerical approach for determining mechanical properties of aluminum subjects to nanoindentation. *Scientific reports*, *5*(1), 1-16.

51. Loucks, R. G., Reed, R. M., Ruppel, S. C., and Jarvie, D. M (2009) Morphology, genesis, and distribution of nanometer-scale pores in siliceous mudstones of the Mississippian Barnet shale, *J. Sed. Res.* 79, 848-861.

52. Lu, Y., Li, Y., Wu, Y., Luo, S., Jin, Y., and Zhang, G. (2019). Characterization of shale softening by large volume-based nanoindentation. In: *Rock Mechanics and Rock Engineering*, 1-17.

53. Luo, Y., Xie, H. P., Ren, L., Zhang, R., Li, C. B., and Gao, C. (2018). Linear elastic fracture mechanics characterization of an anisotropic shale. *Scientific reports*, *8*(1), 1-12.

54. Luo, S., Wu, Y., Li, Y., Wang, D., Kim, D., Song, J., and Zhang, G. (2021). Nanoindentation-enhanced screening of hydraulic fracturing fluid additives. *International Journal of Coal Geology*, *240*, 103744.

55. Lyu, Q., Ranjith, P., Long, X., Kang, Y. and Huang, M, 2015, A review of shale swelling by water adsorption. J. Nat. Gas Sci. Eng. 2015, 27, 1421–1431

56. Lyu, Q., Long, X., Ranjith, P., Tan, J., and Kang, Y., 2018, Experimental investigation on the mechanical behaviors of a low-clay shale under water-based fluids. *Engineering Geology*, *233*, 124-138.

57. Madariaga, R., 2007, Seismic source theory: Treatise on Geophysics, 4, 59–82

58. Maity, D., and Ciezobka, J. (2019). Using microseismic frequency-magnitude distributions from hydraulic fracturing as an incremental tool for fracture completion diagnostics. Journal of Petroleum Science and Engineering, 176, 1135-1151.

59. Mayerhofer, M. J., Stegent, N. A., Barth, J. O., and Ryan, K. M. (2011). Integrating fracture diagnostics and engineering data in the marcellus shale. In *SPE annual technical conference and exhibition*.

60. Mighani, S. (2014) *Microseismic Rock Tensile Failure Related To Improving Hydraulic Fracturing*, M.S. thesis, University of Oklahoma.

61. Mighani, S., Taneja, S., Sondergeld, C. H. and Rai, C. S., 2015, November. Nanoindentation creep measurements on shale. In 49th US Rock Mechanics/Geomechanics Symposium. American Rock Mechanics Association.

62. Mitchell, T. M. and Faulkner, D. R. (2009). The nature and origin of off-fault damage surrounding strike-slip fault zones with a wide range of displacements: A field study from the Atacama fault system, northern Chile, J. Structural Geol. 31, 802-816.

63. Mittal, A., Rai, C. S., and Sondergeld, C. H., 2018, Proppant-Conductivity Testing Under Simulated Reservoir Conditions: Impact of Crushing, Embedment, and Diagenesis on Long- (04), 1304–1315. SPE-191124-PA.

64. Mizuno, T., Le Calvez, J., and Rutledge, J. (2019). Variation of seismic scalar moment–corner frequency relationship during development of a hydraulic fracture system. *The Leading Edge*, *38*(2), 123-129.

65. Molenda, M., Stöckhert, F., Brenne, S., and Alber, M. (2015). Acoustic emission monitoring of laboratory scale hydraulic fracturing experiments. In: 49th US Rock Mechanics/Geomechanics Symposium, San Francisco, CA. ARMA-2015-069.

66. Montgomery, C., 2013, Fracturing Fluids. *Effective and Sustainable Hydraulic Fracturing*.

67. Moradian, Z., Li, Q. B., Morgan, S., da Silva, G., Germaine, J. T., and Einstein, H. H. (2015). Acoustic emission characteristics of shale. In: 13th ISRM International Congress of Rock Mechanics, Montreal, Canada.

68. Moreno, C. (2011) *Microseismic Mapping of Fluid Induced Hydraulic Fractures and Analysis of Location Uncertainties*, M.S. thesis, University of Oklahoma.

69. Oliver, W. C., and Pharr, G. M. (1992). An improved technique for determining hardness and elastic modulus using load and displacement sensing indentation experiments. *Journal of materials research*, *7*(6), 1564-1583.

70. Oliver, W. C., and Pharr, G. M. (2004). Measurement of hardness and elastic modulus by instrumented indentation: Advances in understanding and refinements in technology. *J. Mater. Res*. 19(1): 3-20

71. Ortiz, A. (2010) *Automatic Picking And Classification Of Acoustic Emission Event Arrivals*, M.S. thesis, University of Oklahoma.

72. Papageorgiou, A. S. (1988). On two characteristic frequencies of acceleration spectra: Patch corner frequency and f max. *Bulletin of the Seismological Society of America*, *78*(2), 509-529.

73. Patel, H., Cadwallader, S., and Wampler, J. (2016). Zipper fracturing: Taking theory to reality in the Eagle Ford Shale. In *Unconventional Resources Technology Conference, San Antonio, Texas, 1-3 August 2016* (pp. 1000-1008).

74. Patel, S., Sondergeld, C., and Rai, C. (2017). Laboratory studies of hydraulic fracturing by cyclic injection. In: International Journal of Rock Mechanics and Mining Sciences, 95, 8-15.

75. Philipp, S. L., Afşar, F., and Gudmundsson, A. (2013). Effects of mechanical layering on hydrofracture emplacement and fluid transport in reservoirs. *Frontiers in Earth Science*, *1*, 4.

76. Rassouli, F. S., and Zoback, M. D. (2018). Comparison of short-term and long-term creep experiments in shales and carbonates from unconventional gas reservoirs. *Rock Mechanics and Rock Engineering*, *51*(7), 1995-2014.

77. Ratzlaff. (2019) *SEM Investigation of the Fracture Network (SRV) Induced by Hydraulic Fracturing*, M.S. thesis, University of Oklahoma.

78. Ratzlaff, C. W., Sondergeld, C. H., Rai, C. S., Curtis, M. E., and Jernigen, J. D. (2019). SEM investigation of the fracture network (Stimulated Reservoir Volume) induced by hydraulic fracturing in Tennessee sandstone, ARMA 19-490.

79. Rosenfeld, L. G., Ritter, J. E., Lardner, T. J., and Lin, M. R. (1990). Use of the microindentation technique for determining interfacial fracture energy. *Journal of Applied Physics*, *67*(7), 3291-3296.

80. Rutqvist, J., Rinaldi, A. P., Vilarrasa, V., and Cappa, F. (2019). Numerical geomechanics studies of geological carbon storage (GCS). In *Science of carbon storage in deep saline formations* (pp. 237-252).

81. Rybacki, E., Herrmann, J., Wirth, R., and Dresen, G. (2017). Creep of Posidonia shale at elevated pressure and temperature. *Rock Mechanics and Rock Engineering*, *50*(12), 3121-3140.

82. Schiffmann, K. I., 2011, Determination of fracture toughness of bulk materials and thin films by nanoindentation: comparison of different models, Phil. Mag. 91,7-9, 1163-1178.

83. Shatilo, A. P., Sondergeld, C. H., and Rai, C.S. (1995) "Attenuation measurement on rocks from the Glenn Pool Reservoir, OK." *SEG Technical Program Expanded Abstracts 1995*. Society of Exploration Geophysicists. 882-885.

84. Shukla, P., Kumar, V., Curtis, M., Sondergeld, C. H., and Rai, C. S. (2013). Nanoindentation studies on shales. In: *47th us rock mechanics/geomechanics symposium*. American Rock Mechanics Association.

85. Singh, V.K., Wolfe, C., and Jiao, D., 2019, Fracturing fluids impact on unconventional shale rock mechanical properties and proppant embedment. Presented at the American Rock Mechanics Association, New York City, New York. ARMA 19-1831

86. Sondergeld, C. H. and C. S. Rai, 1993, A new exploration tool: Quantitative core characterization, PAGEOPH 141, 2/3/4, 249-268.

87. Sondergeld, C. H., Ambrose, R. J., Rai, C. S., Moncrieff, J. (2010) Micro-structural studies of gas shales, SPE 131771.

88. Sone, H., and Zoback, M. D. (2013). Mechanical properties of shale-gas reservoir rocks—Part 2: Ductile creep, brittle strength, and their relation to the elastic modulus. *Geophysics*, *78*(5), D393-D402.

89. Sone, H., and Zoback, M. D., 2014, Time-dependent deformation of shale gas reservoir rocks and its long-term effect on the in-situ state of stress. *International Journal of Rock Mechanics and Mining Sciences*, *69*, 120–132.

90. Stein, S., and Wysession, M. (2003). An introduction to seismology. *Earthquakes, and Earth*, *7*(9), 10.

91. Stoeckhert, F., Molenda, M., Brenne, S., and Alber, M. (2015). Fracture propagation in sandstone and slate–Laboratory experiments, acoustic emissions and fracture mechanics. Journal of Rock Mechanics and Geotechnical Engineering, 7(3), 237-249.

92. Suarez-Rivera*, R., Degenhardt, J., Gonten, W. V., Graham, J., Ali, S., and Jegadeesan, A. (2016). Optimizing lateral landing depth for improved well production. In: *Unconventional Resources Technology Conference, San Antonio, Texas, 1-3 August 2016* (pp. 2267-2279).

93. Sukumar, S., Weijermars, R., Alves, I., and Noynaert, S. (2019). Analysis of pressure communication between the Austin Chalk and Eagle Ford reservoirs during a zipper fracturing operation. *Energies*, *12*(8), 1469.

94. Suresh, S., Nieh, T.-G. and Choi, B. W. Nanoindentation of copper thin films on silicon substrates. Scripta Mater. 41, 951–957 (1999).

95. Surguchev, L. M., Giske, N. H., Kollbotn, L., and Shchipanov, A. (2008). Cyclic water injection improves oil production in carbonate reservoir. *In Abu Dhabi International Petroleum Exhibition and Conference. Society of Petroleum Engineers.*

96. Thomsen, L. (1986). Weak elastic anisotropy. *Geophysics*, *51*(10), 1954-1966.

97. Toms, J., Müller, T. M., Ciz, R., and Gurevich, B. (2006). Comparative review of theoretical models for elastic wave attenuation and dispersion in partially saturated rocks. Soil Dynamics and Earthquake Engineering, 26(6-7), 548-565.

98. Walter, W. R., and Brune, J. N. (1993). Spectra of seismic radiation from a tensile crack. Journal of Geophysical Research: Solid Earth, 98(B3), 4449-4459.

99. Walsh, J. B. (1981). Effect of pore pressure and confining pressure on fracture permeability. In *International Journal of Rock Mechanics and Mining Sciences & Geomechanics Abstracts* (Vol. 18, No. 5, pp. 429-435). Pergamon.

100. Warpinski, N. R., Branagan, P. T., Peterson, R. E., Wolhart, S. L., and Uhl, J. E. (1998). Mapping hydraulic fracture growth and geometry using microseismic events detected by a wireline retrievable accelerometer array. In *SPE Gas Technology Symposium*.

101. Warpinski, N.R. (2009). Integrating Microseismic Monitoring with Well Completions, Reservoir Behavior, and Rock Mechanics. In: SPE Tight Gas Completions Conference, San Antonio, TX. SPE-125239

102. Warpinski, N. R. (2013). Understanding hydraulic fracture growth, effectiveness, and safety through microseismic monitoring. In *ISRM International Conference for Effective and Sustainable Hydraulic Fracturing*.

103. Waters, G. A., Lewis, R. E., and Bentley, D. (2011). The effect of mechanical properties anisotropy in the generation of hydraulic fractures in organic shales. In: SPE Annual Technical Conference and Exhibition, Denver, CO. SPE-146776

104. Wick, W. (2015) Application of Nanoindentation for Creep Properties and Saturation Effects, M.S. thesis, University of Oklahoma.

105. Wick, W., Taneja, S., Gupta, I., Sondergeld, C. H., and Rai, C. S. (2020). Chemically Induced Formation Damage in Shale. *Petrophysics*, *61*(02), 239-249.

106. Whitfield, K. C., Bourassa, M. W., Adamolekun, B., Bergeron, G., Bettendorff, L., Brown, K. H., and Combs Jr, G. F. (2018). Thiamine deficiency disorders: diagnosis, prevalence, and a roadmap for global control programs. *Annals of the New York Academy of Sciences*, *1430*(1), 3.

107. Xu, J., Fisher, K., Qiu, F., Malpani, R., Ejofodomi, E., and Viswanathan, A. (2016). Impact of Ash Beds on Production in Eagle Ford Shale. In: *SPE Hydraulic Fracturing Technology Conference*

108. Zang, A. and O. Stephansson, 2010, Stress Field of the Earth's Crust, Springer.

109. Zecevic, M., and Eaton, D. W. (2017). Differentiating Between Shear and Tensile Events Using Spectral Parameters. Geoconvention, Calgary, Canada.

110. Zhuang, L., Kim, K. Y., Jung, S. G., Diaz, M. B., Min, K. B., Park, S., and Yoon, J. S. (2016). Laboratory study on cyclic hydraulic fracturing of Pocheon granite in Korea. In *50th US rock mechanics/geomechanics symposium*.

111. Zhuang, L., Kim, K. Y., Jung, S. G., Nam, Y. J., Min, K. B., Park, S., and Yoon, J. S. (2017). Laboratory evaluation of induced seismicity reduction and permeability enhancement effects of cyclic hydraulic fracturing. In: 51st US Rock Mechanics/Geomechanics Symposium. ARMA-2017-0757.